

Dissertation ETH No. 24474

Synthesis and Application of Bis(acyl)phosphane Oxide Photoinitiators

A Dissertation Submitted to

ETH Zürich

for the degree of

Doctor of Sciences

Presented by

Jieping Wang

Master of Science, Nanjing University of Science and Technology

born 25th of June 1987

Citizen of China

Accepted on the Recommendation of

Prof. Dr. Hansjörg Grützmacher, examiner
Prof. Dr. Christophe Copéret, co-examiner

Zürich 2017

“道可道，非常道。名可名，非常名。”

老子

Acknowledgements

I would like to express my deep gratitude to all the people, without the support and kind help of whom the present work would not have been possible. I would like to express my special thanks to my supervisor Prof. Dr. Hansjörg Grützmacher for the great opportunity he gave me to carry out my PhD in his group. Thanks for his vision, trust, support, and patience during my PhD studies. Furthermore, I am thankful to my co-examiner Prof. Dr. Christophe Copéret for reading and evaluating my thesis.

My special thanks go to Dr. Georgina Müller for her guidance and patience which helped me a lot to get a good start with my PhD studies. I would like to express my sincere gratitude to Dr. Kurt Dietliker for his invaluable suggestions and discussions. Many thanks go to Dr. Daniel Rentsch for solid state NMR measurements and careful corrections of my papers. I would like to thank Christine Rüegg for her help with administrative issues and moral and emotional support. I am also grateful to Dr. Hartmut Schönberg for his help with technical issues.

Big thanks go to Jia En and Christine for proof-reading my thesis and the superb moments spent together.

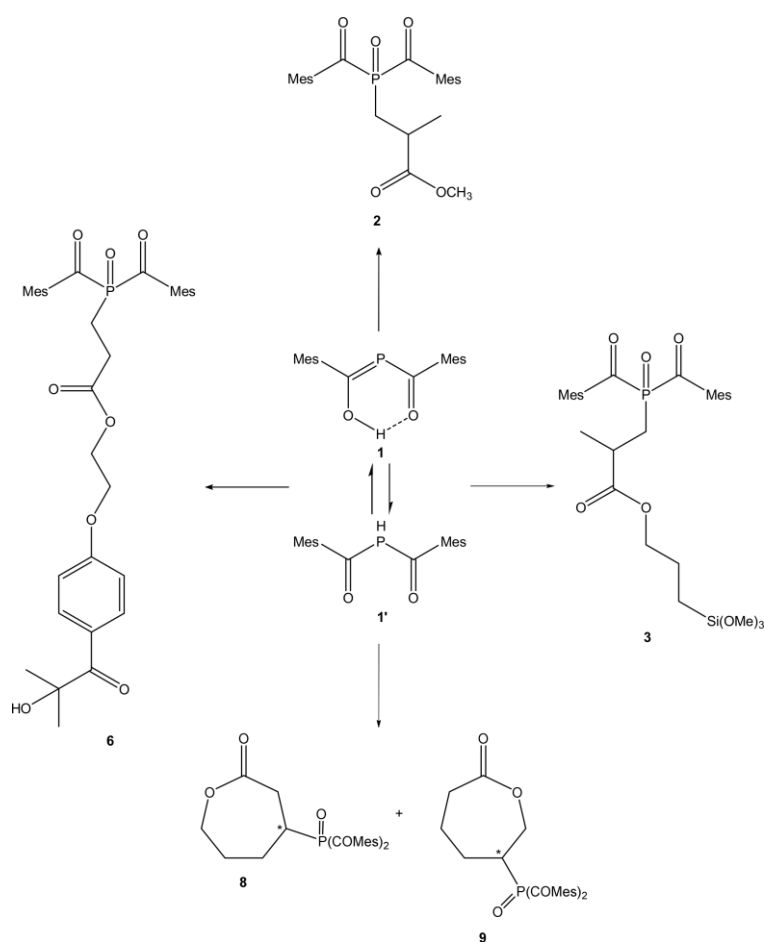
I would like to thank Dr. Tanja Zimmermann, Dr. Philippe Tingaut, Dr. Gilberto Siqueira who involved in the NRP 66 project, Dr. Annalisa Chiappone, Dr. Ignazio Roppolo and Dr. Erika Fantino for the help in 3D printing of nanocomposite hydrogels, Dr. Stefan Baudis and Prof. Dr. Robert Liska for testing the water soluble PEG-BAPO.

I would also like to thank all the former and current group members of the Grützmacher group for discussions and the nice time we had together: Crispin, Jan, Thomas, Pascal, Dominikus, Xiaodan, Vitto, Zoltan, Samuel, Rafael, Robert, Riccardo, Erik, Mark, Matt, Andreas, Monica, Bruno, Fabian, Fernando, Yanbo, Johanna, Esther and Yaqi.

Finally, I would like to thank Xiuxiu and my family and friends for their trust and kind support.

Abstract

Acylphosphane oxide photoinitiators play an important role in radiation curing owing to their excellent efficiency and activity. In the present work the phospho-Michael addition of **1** to olefinic acceptors allowing the facile synthesis of functionalized bis(acyl)phosphane oxide derivatives (BAPOs) is presented. Various applications of the obtained BAPOs were investigated in detail.

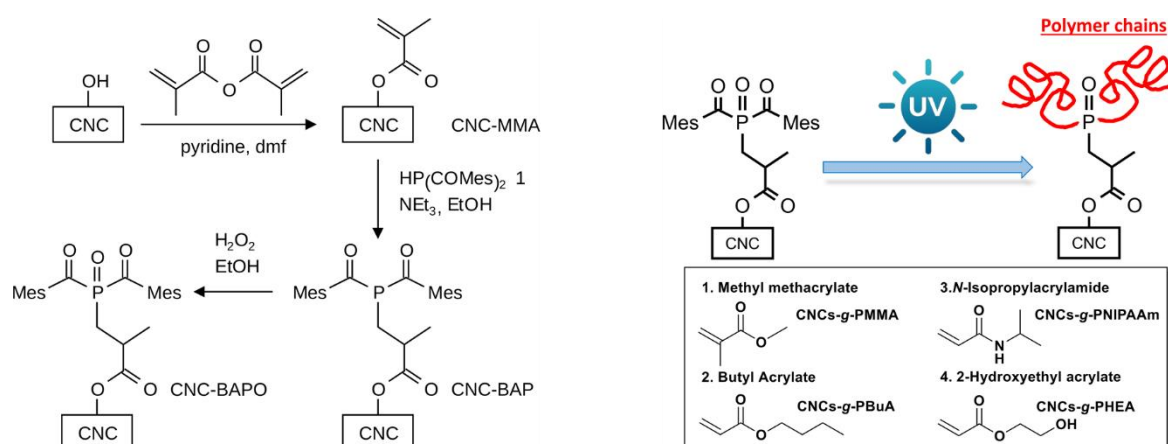


Scheme 1. Synthesis of BAPO derivatives via phospho-Michael addition.

An improved synthetic process of the starting material **1** was developed on a kilogram scale. **2** was prepared by the phospho-Michael addition of methyl methacrylate with **1**. Based on this model reaction, **3** was achieved. It was fixed to glass surfaces for polymer grafting or covalently attached onto porous silica particles to obtain photoactive inorganic fillers. **6** was obtained as a

multifunctional photoinitiator which can be selectively excited at different irradiation wavelengths for the synthesis of star polymers. **8** and **9** were synthesized by phospho-Michael addition of **1** onto cyclohex-2-en-1-one and a subsequent Baeyer–Villiger oxidation. 4-BAPO-substituted lactone (**8**) and 6-BAPO-substituted lactone (**9**) were obtained with a ratio of 1 : 0.28 (Scheme 1).

Cellulose nanocrystals (CNCs) were functionalized with methacryloyl groups to which **1** was attached by a phospho-Michael addition. Subsequent oxidation with H₂O₂ generated photoactive groups, which serve as initiators for free radical polymerization of acrylic monomers. Hybrid materials with excellent graft yields were obtained rapidly under mild and acid-free conditions (Scheme 2).



Scheme 2. (left): Functionalization of CNCs with a BAPO photoinitiator. (right): Graft polymerization of CNC-BAPO.

Multifunctional cellulose nanocrystals were achieved by facile surface immobilization of photoactive groups. They serve as highly efficient visible light photoinitiators, cross-linkers and covalently embedded nanofillers for 3D printing of nanocomposite hydrogels. Aqueous formulations containing the modified nanocrystals and a mono-functional methacrylate as the only monomer, result in shape-persistent and free-standing 3D structured objects, which can absorb water more than ten times their own weight (Figure 1).

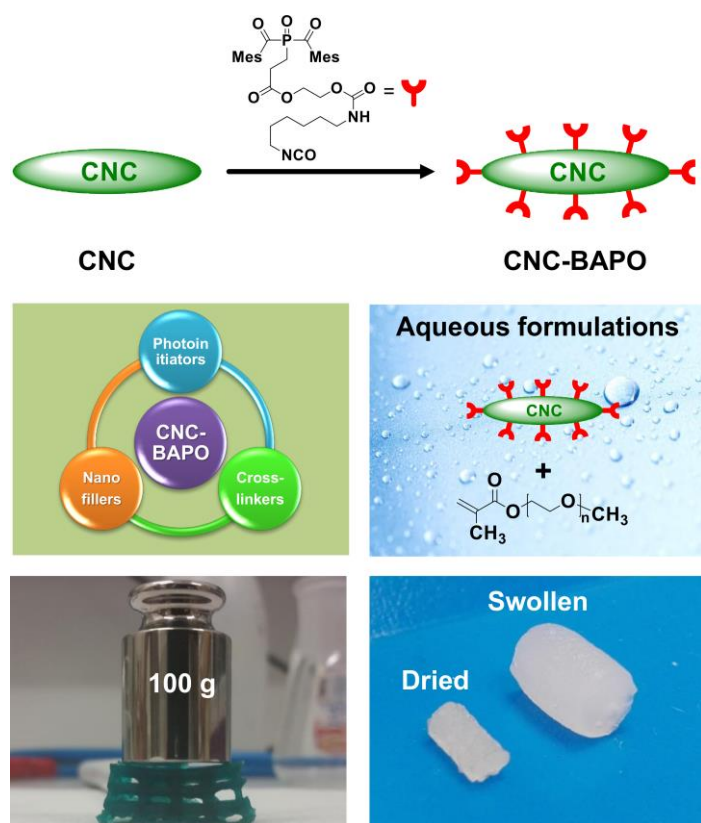


Figure 1. All-in-One Cellulose Nanocrystals for 3D Printing of Nanocomposite Hydrogels.

A highly efficient water-soluble photoinitiator was prepared in a facile one-pot synthesis. It shows excellent water-solubility, good storage stability and higher reactivity under visible light irradiation. A well-defined gyroid structure was successfully printed by a digital light processing (DLP) 3D printer equipped with visible LEDs (Figure 2).

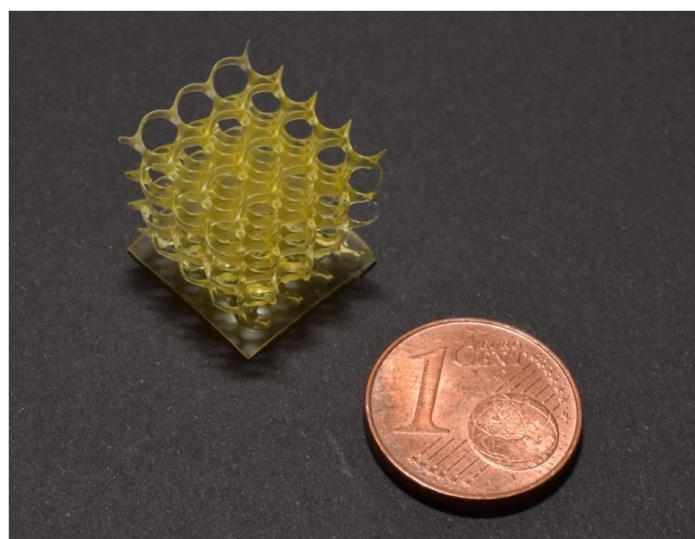
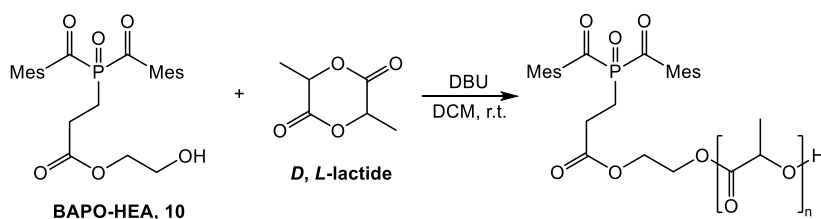


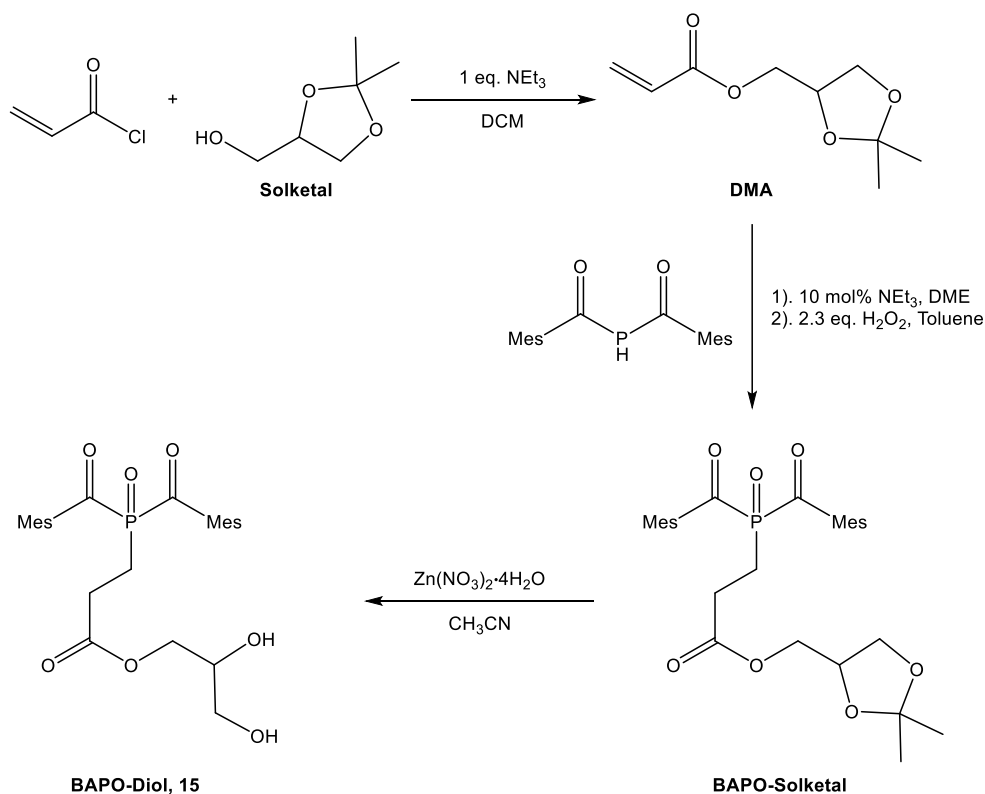
Figure 2. Photograph of a 3D printed hydrogel with gyroid structure.

10 was prepared and applied as an initiator for the ring-opening polymerization of *D, L*-lactide, generating a photoactive polylactic acid with a terminal BAPO group (Scheme 3).



Scheme 3. Synthesis of PLA-BAPO with a terminal BAPO group.

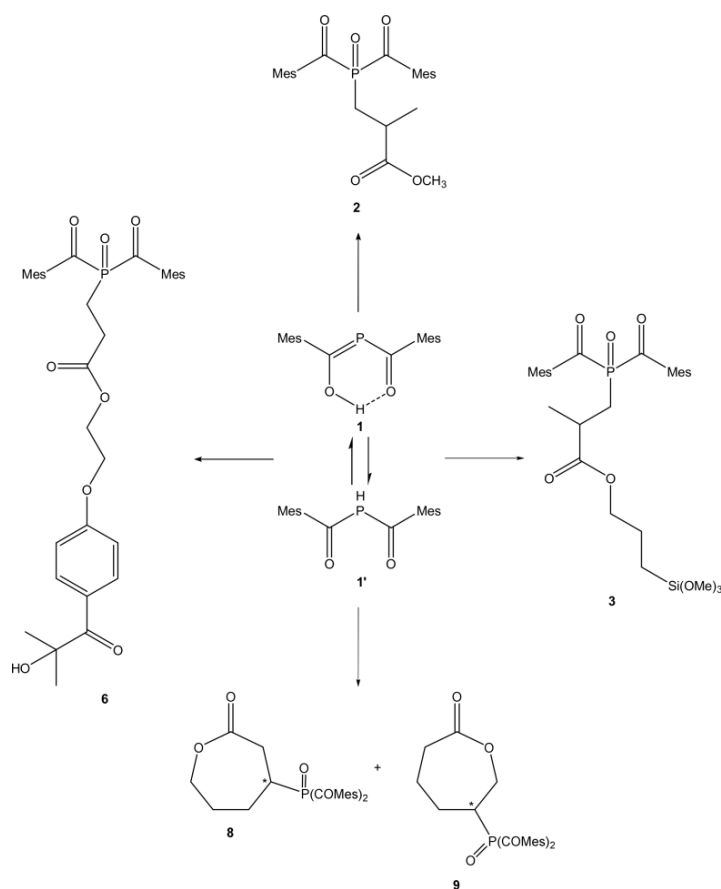
15 was prepared for the synthesis of photoactive polyurethanes (PUs) (Scheme 4). The polycondensation of **15** with other diols and diisocyanates results in PUs with side-chain BAPOs. Preliminary tests indicate that these photoactive polymers can be used as polymeric photoinitiators for free-radical polymerization of unsaturated monomers.



Scheme 4. Synthesis of BAPO-Diol (**15**).

Zusammenfassung

Acylphosphanoxid-Photoinitiatoren spielen aufgrund ihrer hervorragenden Effizienz und Aktivität eine wichtige Rolle bei der photoinduzierten Polymerisation. In dieser Arbeit wird die Phospha-Michael Addition von **1** mit olefinischen Akzeptoren, die eine einfache Synthese von funktionalisierten Bis(acyl)-phosphanoxid – Derivaten (BAPOs) erlaubt, gezeigt. Verschiedene Anwendungen der erhaltenen BAPOs wurden ausführlich untersucht.

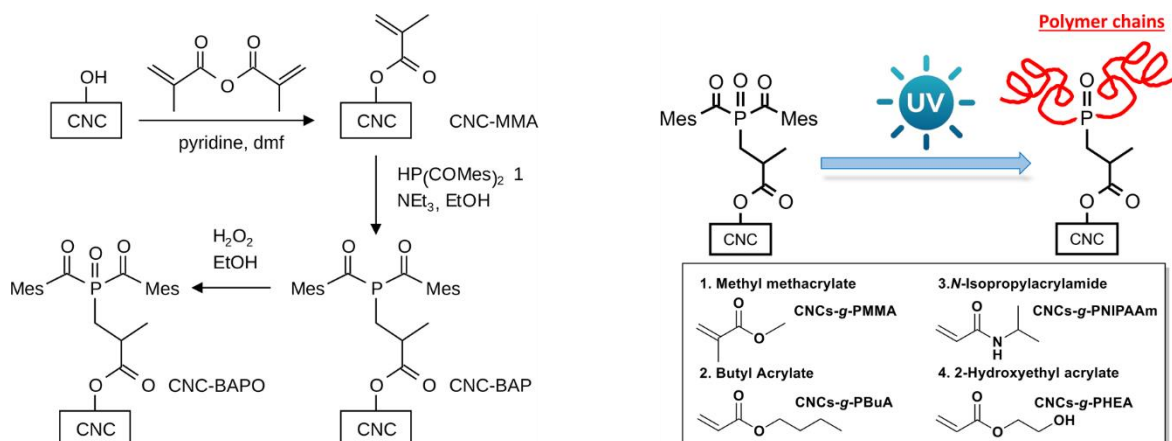


Scheme 5. Synthese von BAPO – Derivaten via phospho-Michael Addition.

Es wurde eine verbesserte Synthese des Eduktes **1** im Kilogramm Maßstab entwickelt. **2** wurde durch eine Phospha-Michael Addition von Methyl-Methacrylat mit **1** dargestellt. Basierend auf dieser Modell-Reaktion konnte **3** erhalten werden, welches auf Glas-Oberflächen fixiert wurde, die dann photochemisch mit Polymeren beschichtet werden können. **3** wurde auch kovalent an poröse Silika-Partikel gebunden und es wurden photoaktive anorganische

Füllstoffe erhalten. Die Verbindung **6** ist ein multifunktionaler Photoinitiator, der selektiv bei verschiedenen Wellenlängen angeregt werden kann und so die Synthese von sternartigen Polymeren ermöglicht. **8** und **9** wurden durch phospho-Michael Addition von **1** mit Cyclohex-2-en-1-on und nachfolgender Baeyer-Villiger Oxidation synthetisiert. Das 4-BAPO substituierte Lacton (**8**) und das 6-BAPO substituierte Lacton (**9**) wurden im Verhältnis 1:0.28 erhalten (Scheme 5).

Zellulose Nanokristalle (CNCs) wurden mit Methacryloyl-Gruppen funktionalisiert und dann mit **1** in einer phospho-Michael Addition umgesetzt. Durch eine anschließende Oxidation mit H₂O₂ wurden photoaktive Gruppen gebildet, die als Initiatoren für die photochemische Polymerisation von Acryl-Monomeren dienen. Hybridmaterialien können mit exzellenten Ausbeuten unter milden, säurefreien Bedingungen erhalten werden (Scheme 6).



Scheme 6. Funktionalisierung von CNC mit einem BAPO Photoinitiator (rechts). Polymerisation auf einem CNC-BAPO.

Multifunktionelle Zellulose-Nanokristalle wurden durch einfache Immobilisierung von photoaktiven Gruppen an Oberflächen erhalten. Sie können als hoch effiziente Photoinitiatoren in sichtbaren Bereichen des Lichtes, als Cross-Linker und als kovalent eingebettete Nanofüller für das 3D Drucken von nanokompositen Hydrogelen dienen. Wässrige Formulierungen mit den modifizierten Nanokristallen und monofunktionalen Methacrylat, als einziges Monomer,

führen zu Form-persistenten und frei stehenden 3D strukturierten Objekten, die mehr als das Zehnfache ihres eigenen Gewichtes an Wasser absorbieren können (Figure 3).

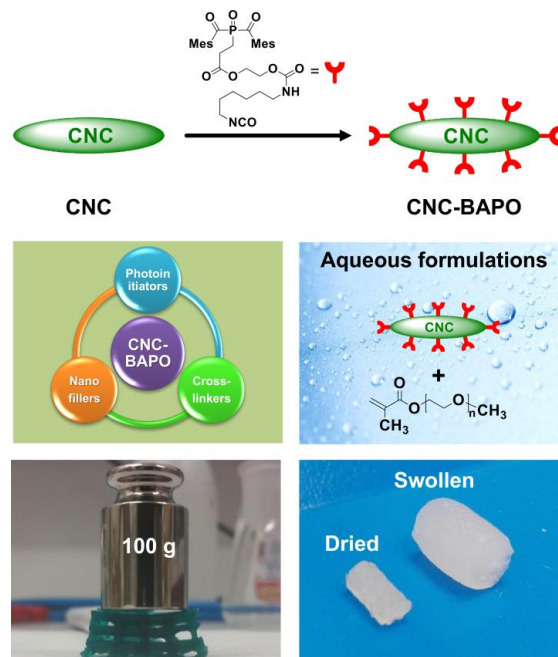


Figure 3. All-in-One Zellulose Nanokristalle für das 3D Drucken von Nanokomposithydrogelen.

Ein hoch effizienter wasserlöslicher Photoinitiator wurde in einer Eintopf-Synthese dargestellt. Er ist ausgezeichnet wasserlöslich, hat eine gute Lagerungs-Stabilität und zeigt eine höhere Reaktivität unter Bestrahlung mit sichtbarem Licht. Eine gut definierte Gyroid - Struktur wurde erfolgreich mit einem Digital Light Processing (DLP) 3D Drucker, der mit LEDs die im sichtbaren Bereich des Lichtes strahlen ausgerüstet war, gedruckt (Figure 4).

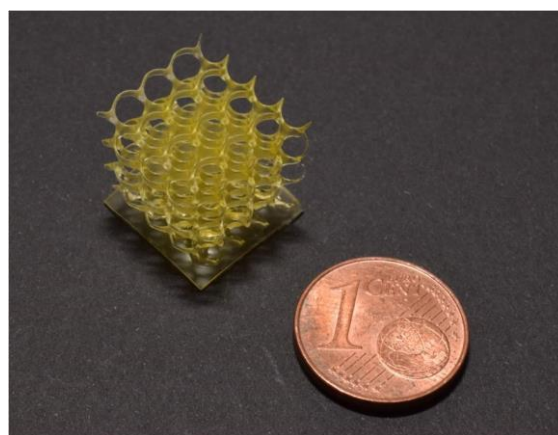
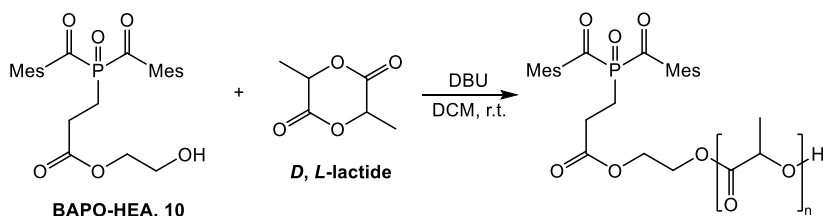


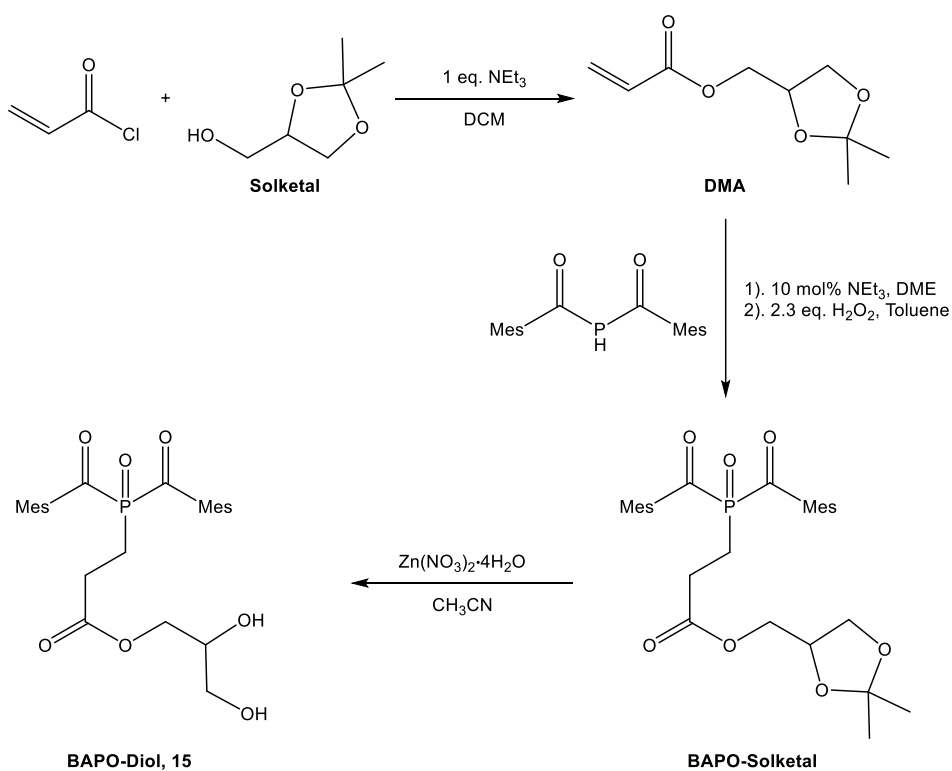
Figure 4. Foto eines 3D gedruckten Hydrogel mit Gyroid-Struktur.

Die Verbindung **10** wurde als Initiator für die Ringöffnungspolymerisation von *D, L*-Lactid unter Bildung einer photoaktiven Polymilchsäure-Säure mit einer terminalen BAPO-Gruppe eingesetzt (Scheme 7).



Scheme 7. Synthese von PLA-BAPO mit einer terminalen BAPO – Gruppe.

15 wurde dargestellt zur Synthese von photoaktiven Polyurethanen (PUs) (Scheme 8). Die Polykondensation von **15** mit anderen Diolen und Diisocyanaten führt zu PUs mit Seitenketten – BAPOs. Vorläufige Tests deuten darauf hin, dass diese photoaktiven Polymere als Photoinitiatoren für die radikalische Polymerisation von ungesättigten Monomeren verwendet werden könnten.



Scheme 8. Synthese von BAPO-Diol (15).

Publications

1. **J. Wang**, A. Chiappone, I. Roppolo, F. Shao, E. Fantino, M. Lorusso, D. Rentsch, K. Dietliker, C. F. Pirri, H. Grützmacher. *Angew. Chem. Int. Ed.* **2018**, *57*, 2353-2356.
2. **J. Wang**, S. Stanic, A. A. Altun, M. Schwentenwein, K. Dietliker, L. Jin, J. Stampfl, S. Baudis, R. Liska, H. Grützmacher. *Chem. Commun.* **2018**, *54*, 920-923.
3. **J. Wang**, G. Siqueira, G. Müller, D. Rentsch, A. Huch, P. Tingaut, J. L. Grützmacher, H. Grützmacher. *Chem. Commun.* **2016**, *52*, 2823-2826.
4. M. Sahin, K. K. Krawczyk, P. Roszkowski, **J. Wang**, B. Kaynak, W. Kern, S. Schlögl, H. Grützmacher. *Eur. Polym. J.* **2018**, *98*, 430-438.
5. A. Eibel, D. E. Fast, J. Sattelkow, M. Zalibera, **J. Wang**, A. Huber, G. Müller, D. Neshchadin, K. Dietliker, H. Plank, H. Grützmacher, G. Gescheidt. *Angew. Chem. Int. Ed.* **2017**, *56*, 14306-14309.
6. M. Sahin, S. Schlögl, S. Kaiser, W. Kern, **J. Wang**, H. Grützmacher. *J. Polym. Sci. A Polym. Chem.* **2017**, *55*, 894-902.
7. S. Benedikt, **J. Wang**, M. Markovic, N. Moszner, K. Dietliker, A. Ovsianikov, H. Grützmacher, R. Liska. *J. Polym. Sci. A Polym. Chem.* **2016**, *54*, 473-479.
8. M. Sangermano, M. Periolatto, M. Castellino, **J. Wang**, K. Dietliker, J. L. Grützmacher, H. Grützmacher. *ACS Appl. Mater. Interfaces* **2016**, *8*, 19764-19771.

1	Introduction	1
1.1	Photopolymerization.....	1
1.2	Acylphosphane oxide photoinitiators	2
1.3	Cellulose nanocrystals	4
1.4	Objective and Outline	6
1.5	References	7
2	Synthesis of bis(acyl)phosphane oxide photoinitiators via phospho- Michael addition	11
2.1	Introduction	11
2.2	Synthesis of phosphane starting material: bis(2,4,6-trimethylbenzoyl) hydrogenphosphane (BAP-H, 1)	12
2.3	Synthesis of methyl 3-(bis(2,4,6-trimethylbenzoyl)phosphoryl)-2-methyl-propanoate (BAPO-MMA, 2)	14
2.4	Synthesis and application of 4-(trimethoxysilyl)butyl-3-[bis(2,4,6-trimethylbenzoyl)- phosphinoyl]-2-methyl-propionate (TMESi ² -BAPO, 3).....	14
2.5	Synthesis of multi-wave photoinitiators for producing star polymers via free radical polymerization.....	18
2.6	Synthesis of BAPO functionalized ϵ -caprolactones	22
2.7	Conclusion	23
2.8	References	24
3	Surface functionalization of cellulose nanocrystals for polymer grafting	27
3.1	Introduction	27
3.2	Synthesis and Characterization.....	28
3.3	Polymer Grafting	32
3.4	Properties of grafted hybrid materials.	36
3.5	Conclusion	39
3.6	Methods	39

3.7	References	44
4	All-in-One cellulose nanocrystals for 3D printing of nanocomposite hydrogels	47
4.1	Introduction	47
4.2	Synthesis of BAPO derivatives and functionalization of cellulose nanocrystals	48
4.3	Photopolymerization studies of different aqueous formulations	56
4.4	3D printing of nanocomposite hydrogels	64
4.5	Conclusion	68
4.6	Methods	69
4.7	References	76
5	A highly efficient waterborne photoinitiator for visible-light-induced 3D printing of hydrogels	79
5.1	Introduction	79
5.2	Synthesis and characterization of PEG-BAPO	80
5.3	Photoreactivity of PEG-BAPO	86
5.4	3D printing of hydrogel model using PEG-BAPO	89
5.5	Conclusion	91
5.6	Methods	92
5.7	References	96
6	Bis(acyl)phosphane oxide-based polymeric photoinitiators	99
6.1	Introduction	99
6.2	Poly(lactic acid) with terminal BAPO group	99
6.3	Polyurethane with side-chain BAPO (PU-BAPO)	101
6.4	Conclusion	105
6.5	References	105
7	Summary and Outlook	109

8	Experimental procedures	113
8.1	General techniques and chemicals.....	113
8.2	Analytic methods.....	113
8.3	Synthetic protocols	116

1 Introduction

1.1 Photopolymerization

The Sun provides the ultimate source of light which can be readily harvested for chemical transformations to make life possible on Earth.¹ After absorbing light, molecules are promoted to an electronically excited state that can significantly change their chemical properties and reactivities.² This allows access to compounds otherwise difficult to obtain with ground-state reactions.³⁻⁵

The use of light to control the formation, structure, and biochemomechanical properties of polymeric materials is one of the most powerful paradigms in polymer science.⁶ Absorption of a mole of photons at 365 nm provides energy 130 times higher than the thermal energy available to activate a reaction at 25 °C. This massive amount of energy input provided by light would overcome energy barriers for many chemical reactions occurring rapidly at room temperature.⁷ Because of this, photoinitiated polymerization has striking advantages over thermal and redox polymerizations, and has found widespread applications in industry, such as coatings, inks, adhesives, optoelectronics, laser imaging, stereolithography and biomedical applications.⁸

Photoinitiators play a key role in photopolymerization. A photoinitiator or photoinitiator system can be defined as a molecule or combinations of molecules that, upon absorption of light, initiate polymerization by the generated reactive species.⁹ In the case of free radical polymerization, photoinitiators are classified as cleavage (Norrish type I) and H-abstraction type (Norrish type II) initiators. The main type I photoinitiators are aromatic carbonyl compounds which undergo “ α -cleavage”, generating free radicals upon absorption of light (Figure 1.1a). A bimolecular reaction with a co-initiator (e.g., alcohols, tertiary amines, or thiols)

is necessary for type II photoinitiators (Figure 1.1b), resulting in slower curing rate and easier to be quenched by monomers with low triplet energy or by oxygen.⁸

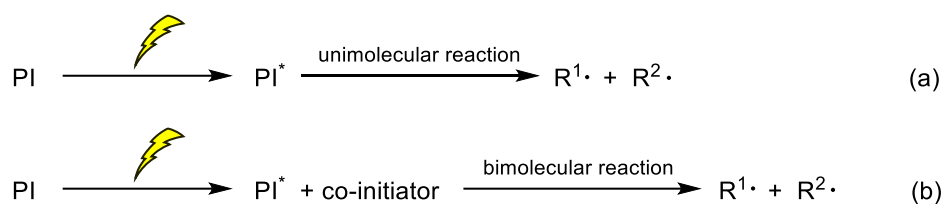


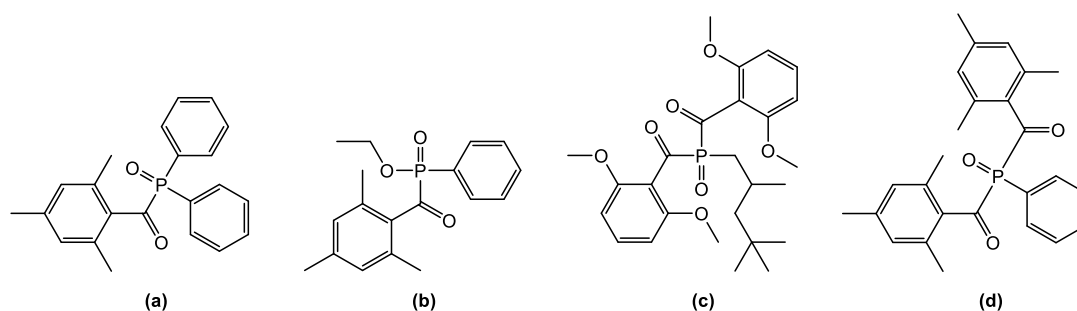
Figure 1.1 Reaction schemes for the free radical photoinitiators of type I (a) and type II (b) upon light irradiation.

1.2 Acylphosphane oxide photoinitiators

Due to the long wavelength absorption characteristics, thermal stability and high reactivity, both mono(acyl)phosphane oxides (MAPOs) and bis(acyl)phosphane oxides (BAPOs) are used as photoinitiators since 1980s.¹⁰ Their photobleaching properties have made them prime photoinitiators for clear coatings and inks.¹¹ Short-lived (< 1 ns) excited triplet state enables these photoinitiators to be less affected by triplet quenchers including styrene. Even a weak visible-light irradiation can lead to the formation of a phosphinoyl and an acyl radical through an efficient type I cleavage. The phosphinoyl radical is about 1000 times more reactive than the acyl radicals.¹² BAPOs show superior efficiencies, as their molar extinction coefficients at 400 nm are usually higher than those of the corresponding MAPOs.¹³

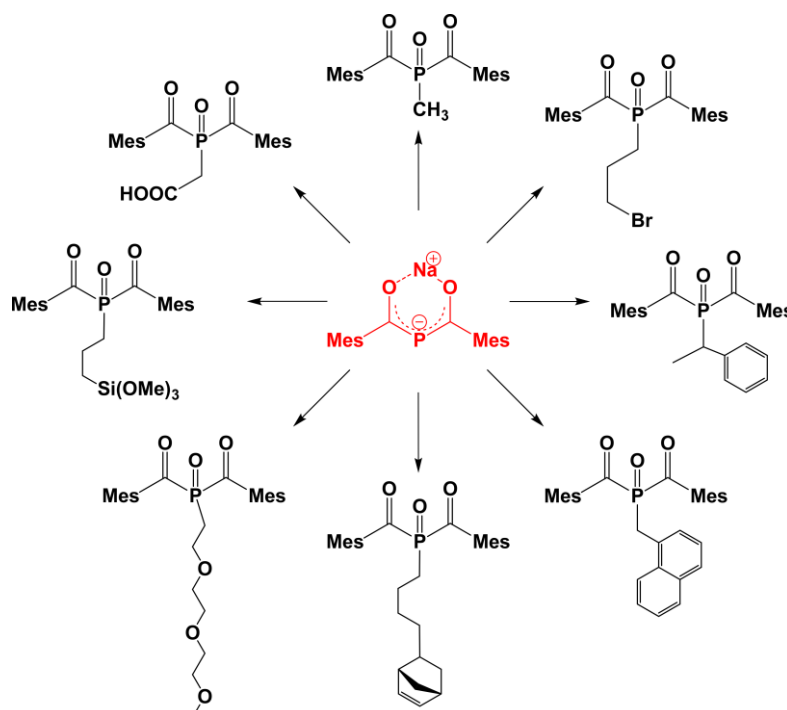
Some commercially available MAPOs and BAPOs are shown in Scheme 1.1. While MAPOs are easily available through an Arbuzov reaction of alkoxyphosphanes with acyl chloride, the synthesis of BAPOs are more complicated than that of MAPOs. Conventional synthetic routes involve a primary phosphane (RPH₂) or a metallated derivative (RPH_{2-x}M_x) with an acyl

chloride. These have inherent safety problems and a low functional-group compatibility, only aryl or alkyl substituents are bound to the phosphorus.¹³



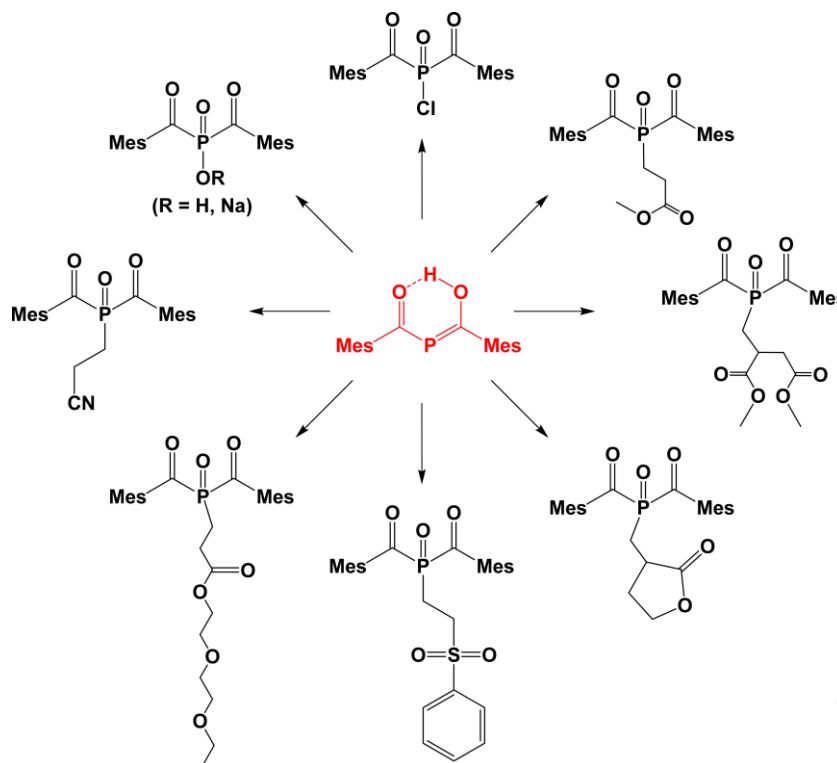
Scheme 1.1 Structures of commercially available MAPOs (a) (Lucirin® TPO), (b) (Lucirin® TPO-L) and BAPOs (c) (BAPO part in Irgacure® 1700), (d) (Irgacure® 819).

Recently, a simple one-pot procedure for the conversion of white or red phosphorus to sodium bis(mesityl)phosphide $\text{NaP}(\text{COMes})_2$ was developed in the group of Prof. Grützmacher.^{12, 14-15} The nucleophilic substitution of $\text{NaP}(\text{COMes})_2$ with alkyl halides (R-X) provides a straightforward method to obtain P-functionalized BAPO derivatives (Scheme 1.2).



Scheme 1.2 Synthesis of P-functionalized bis(acyl)phosphane oxides from $\text{NaP}(\text{COMes})_2$.

The protonation of $\text{NaP}(\text{COMes})_2$ with acetic acid results in $\text{HP}(\text{COMes})_2$ which can be used as another building block for the synthesis of functionalized BAPO photoinitiators (Scheme 1.3).¹⁶⁻¹⁷



Scheme 1.3 Synthesis of P-functionalized bis(acyl)phosphane oxides from $\text{HP}(\text{COMes})_2$.

1.3 Cellulose nanocrystals

Cellulose constitutes the most abundant renewable polymer resource produced in the biosphere on Earth. Cellulose-based materials (wood, hemp, cotton, linen, etc.) have been used by human beings for thousands of years and their use continues today as verified by the magnitude of the world wide industries in forest products, paper, textiles, etc.¹⁸ Controlled acid hydrolysis of cellulose fibers results in defect-free rod-like cellulose nanocrystals (CNCs), which have attracted tremendous attention in the past few years. These stiff rod-like

nanoparticles have a typical width of 2 - 50 nm and length of 100 - 2000 nm. They can be used as reinforcing fillers, security papers, emulsifying agents and medical implants, owing to their low cost, availability, renewability, light weight, nanoscale dimension, and unique morphology.¹⁹ However, due to the inherent hydrophilicity, their utilization is restricted to applications involving hydrophilic or polar media. Various surface chemical modification strategies, including oxidation, esterification, amidation, carbamation, etherification, click chemistry and polymer grafting, have been developed to extend their use to highly sophisticated applications.²⁰⁻²¹

Compared to modifications by covalently attaching small molecules, polymer grafting could lead to extraordinary properties. The grafted polymer chains can act as binding sites for drug delivery and toxin removal. The covalent bonding between the reinforcement and the matrix may result in near-perfect stress transfer at the interface with superior mechanical properties of the composite as a result.²² The two most common approaches are “grafting onto” and “grafting from”. In the former approach, the pre-synthesized polymer chains are attached to hydroxyl groups on the surfaces via reactive end groups. The properties of the obtained materials are well controlled because the attached polymer can be fully characterized before grafting, but high grafting densities are difficult to achieve due to steric hindrance and high viscosity of the reaction medium. The latter method consists of mixing the cellulose with monomers and initiators to induce polymerization from the surfaces, which gives high grafting densities due to less steric hindrance and lower viscosity of the medium. However, it is not easy to control and properly determine the molecular weight of the grafted polymers.

Native CNCs have an axial elastic modulus ranging from 110 to 220 GPa, while the tensile strength is in the range of 7.5–7.7 GPa. These make CNCs ideal candidates as a reinforcement

material comparable to other nanofillers, such as clay nanoplatelets or carbon nanotubes.²³ Moreover, CNCs possess excellent biodegradability and low ecotoxicological risk. The incorporation of CNCs either as nanofillers or multifunctional cross-linkers into several polymeric hydrogel matrices have been reported,²⁴⁻³¹ showing the great potential of their applications as higher performance materials.

1.4 Objective and Outline

In this work, a series of phosphorous-functionalized BAPO photoinitiators with specific properties are prepared by the efficient phospho-Michael addition of HP(COMes)₂ to a variety of olefinic acceptors. Various applications of the obtained BAPOs are investigated in detail.

The phospho-Michael addition of HP(COMes)₂ to olefinic acceptors is further studied in chapter 2. Based on this convenient strategy, a tri(methoxy)silyl-substituted BAPO derivative is obtained and has been fixed to the surfaces of non-porous glass or porous silica particles for further applications. A multifunctional BAPO photoinitiator comprising three photoactive groups, which can be selectively excited at different irradiation wavelengths, is obtained for the synthesis of star polymers. BAPO functionalized ϵ -caprolactones are synthesized by phospho-Michael addition and a subsequent Baeyer–Villiger oxidation.

Chapter 3 and 4 describe the surface functionalization of cellulose nanocrystals (CNCs) with immobilized BAPO photoinitiators. The first approach (Chapter 3) consists of modifying the surfaces of CNCs with methacrylate functions in a first step, to which bis(acyl)phosphane oxide functions were added in a second step. Acrylic monomers have been grafted from the photoactive surfaces with excellent graft yields. The second strategy involves a new BAPO with an isocyanate end group directly binding covalently to CNCs without any further

modification of their surfaces. The obtained versatile cellulose nanocrystals are applied as visible light photoinitiators, cross-linkers, as well as covalently embedded nanofillers for 3D printing of nanocomposite hydrogels. Shape-persistent and free-standing 3D structured objects have been rapidly printed, showing a superior swelling capacity and improved mechanical properties.

Chapter 5 presents a polyethylene glycol functionalized BAPO photoinitiator, which has higher solubility and reactivity than state of the art water-soluble PIs. Under visible light irradiation (460 nm), a hydrogel with well-defined structure was successfully printed by a digital light processing (DLP) 3D printer.

Two strategies to prepare polymeric BAPO photoinitiators are demonstrated in Chapter 6. One includes introducing a BAPO group in the terminal position of a polylactic acid chain, the other involves preparing polyurethanes with side-chain BAPOs by polycondensation. Preliminary results show the possibility of using these polymers for free-radical polymerization.

1.5 References

1. Beeler, A. B., Introduction: Photochemistry in Organic Synthesis. *Chemical Reviews* **2016**, *116* (17), 9629-9630.
2. Hoffmann, N., Photochemical Reactions as Key Steps in Organic Synthesis. *Chemical Reviews* **2008**, *108* (3), 1052-1103.
3. Prier, C. K.; Rankic, D. A.; MacMillan, D. W. C., Visible Light Photoredox Catalysis with Transition Metal Complexes: Applications in Organic Synthesis. *Chemical Reviews* **2013**, *113* (7), 5322-5363.
4. Romero, N. A.; Nicewicz, D. A., Organic Photoredox Catalysis. *Chemical Reviews* **2016**, *116* (17), 10075-10166.
5. Ghogare, A. A.; Greer, A., Using Singlet Oxygen to Synthesize Natural Products and Drugs. *Chemical Reviews* **2016**, *116* (17), 9994-10034.

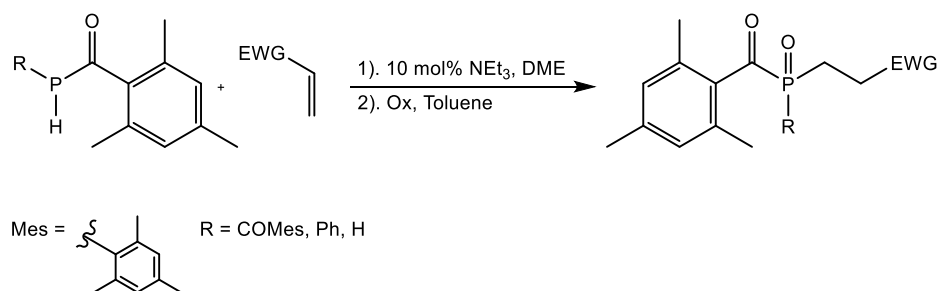
6. Chatani, S.; Kloxin, C. J.; Bowman, C. N., The power of light in polymer science: photochemical processes to manipulate polymer formation, structure, and properties. *Polymer Chemistry* **2014**, *5* (7), 2187-2201.
7. Dadashi-Silab, S.; Doran, S.; Yagci, Y., Photoinduced Electron Transfer Reactions for Macromolecular Syntheses. *Chemical Reviews* **2016**, *116* (17), 10212-10275.
8. Yagci, Y.; Jockusch, S.; Turro, N. J., Photoinitiated Polymerization: Advances, Challenges, and Opportunities. *Macromolecules* **2010**, *43* (15), 6245-6260.
9. Monroe, B. M.; Weed, G. C., Photoinitiators for free-radical-initiated photoimaging systems. *Chemical Reviews* **1993**, *93* (1), 435-448.
10. Fouassier, J., Lalevée, J., *Photoinitiators for Polymer Synthesis: Scope, Reactivity, and Efficiency*. Wiley-VCH Verlag GmbH & Co. KGaA, Weinheim, 2012.
11. Green, W., A., *Industrial Photoinitiators: A Technical Guide*. CRC Press, Boca Raton, 2010.
12. Huber, A.; Kuschel, A.; Ott, T.; Santiso-Quinones, G.; Stein, D.; Bräuer, J.; Kissner, R.; Krumeich, F.; Schönberg, H.; Levalois-Grützmaker, J.; Grützmaker, H., Phosphorous-Functionalized Bis(acyl)phosphane Oxides for Surface Modification. *Angewandte Chemie International Edition* **2012**, *51* (19), 4648-4652.
13. Gonsalvi, L.; Peruzzini, M., Novel Synthetic Pathways for Bis(acyl)phosphine Oxide Photoinitiators. *Angewandte Chemie International Edition* **2012**, *51* (32), 7895-7897.
14. Huber, A. *Diss. ETH Nr.* 20480, 2012.
15. Eibel, A.; Schmallegger, M.; Zalibera, M.; Huber, A.; Bürkl, Y.; Grützmaker, H.; Gescheidt, G., Extending the Scope of Bis(acyl)phosphane Oxides: New Derivatives. *European Journal of Inorganic Chemistry* **2017**, n/a-n/a.
16. Müller, G.; Zalibera, M.; Gescheidt, G.; Rosenthal, A.; Santiso-Quinones, G.; Dietliker, K.; Grützmaker, H., Simple One-Pot Syntheses of Water-Soluble Bis(acyl)phosphane Oxide Photoinitiators and Their Application in Surfactant-Free Emulsion Polymerization. *Macromolecular Rapid Communications* **2015**, *36* (6), 553-557.
17. Müller, G., *Diss. ETH Nr.* 21309, 2013.
18. Moon, R. J.; Martini, A.; Nairn, J.; Simonsen, J.; Youngblood, J., Cellulose nanomaterials review: structure, properties and nanocomposites. *Chemical Society Reviews* **2011**, *40* (7), 3941-3994.
19. Habibi, Y.; Lucia, L. A.; Rojas, O. J., Cellulose Nanocrystals: Chemistry, Self-Assembly, and Applications. *Chemical Reviews* **2010**, *110* (6), 3479-3500.
20. Eyley, S.; Thielemans, W., Surface modification of cellulose nanocrystals. *Nanoscale* **2014**, *6* (14), 7764-7779.
21. Habibi, Y., Key advances in the chemical modification of nanocelluloses. *Chemical Society Reviews* **2014**, *43* (5), 1519-1542.

22. Dufresne, A., *Nanocellulose : from nature to high performance tailored materials*. Walter De Gruyter, Berlin, 2012.
23. Domingues, R. M. A.; Gomes, M. E.; Reis, R. L., The Potential of Cellulose Nanocrystals in Tissue Engineering Strategies. *Biomacromolecules* **2014**, *15* (7), 2327-2346.
24. Das, D.; Kar, T.; Das, P. K., Gel-nanocomposites: materials with promising applications. *Soft Matter* **2012**, *8* (8), 2348-2365.
25. Yang, J.; Zhao, J.-J.; Xu, F.; Sun, R.-C., Revealing Strong Nanocomposite Hydrogels Reinforced by Cellulose Nanocrystals: Insight into Morphologies and Interactions. *ACS Applied Materials & Interfaces* **2013**, *5* (24), 12960-12967.
26. Yang, X.; Bakaic, E.; Hoare, T.; Cranston, E. D., Injectable Polysaccharide Hydrogels Reinforced with Cellulose Nanocrystals: Morphology, Rheology, Degradation, and Cytotoxicity. *Biomacromolecules* **2013**, *14* (12), 4447-4455.
27. Schmocker, A.; Khoushabi, A.; Frauchiger, D. A.; Gantenbein, B.; Schizas, C.; Moser, C.; Bourban, P.-E.; Pioletti, D. P., A photopolymerized composite hydrogel and surgical implanting tool for a nucleus pulposus replacement. *Biomaterials* **2016**, *88*, 110-119.
28. Yang, J.; Han, C.-R.; Zhang, X.-M.; Xu, F.; Sun, R.-C., Cellulose Nanocrystals Mechanical Reinforcement in Composite Hydrogels with Multiple Cross-Links: Correlations between Dissipation Properties and Deformation Mechanisms. *Macromolecules* **2014**, *47* (12), 4077-4086.
29. Yang, J.; Han, C.-r.; Xu, F.; Sun, R.-c., Simple approach to reinforce hydrogels with cellulose nanocrystals. *Nanoscale* **2014**, *6* (11), 5934-5943.
30. Liu, L.; Li, L.; Qing, Y.; Yan, N.; Wu, Y.; Li, X.; Tian, C., Mechanically strong and thermosensitive hydrogels reinforced with cellulose nanofibrils. *Polymer Chemistry* **2016**, *7* (46), 7142-7151.
31. Siqueira, G.; Kokkinis, D.; Libanori, R.; Hausmann, M. K.; Gladman, A. S.; Neels, A.; Tingaut, P.; Zimmermann, T.; Lewis, J. A.; Studart, A. R., Cellulose Nanocrystal Inks for 3D Printing of Textured Cellular Architectures. *Advanced Functional Materials* **2017**, *27* (12), 1604619-n/a.

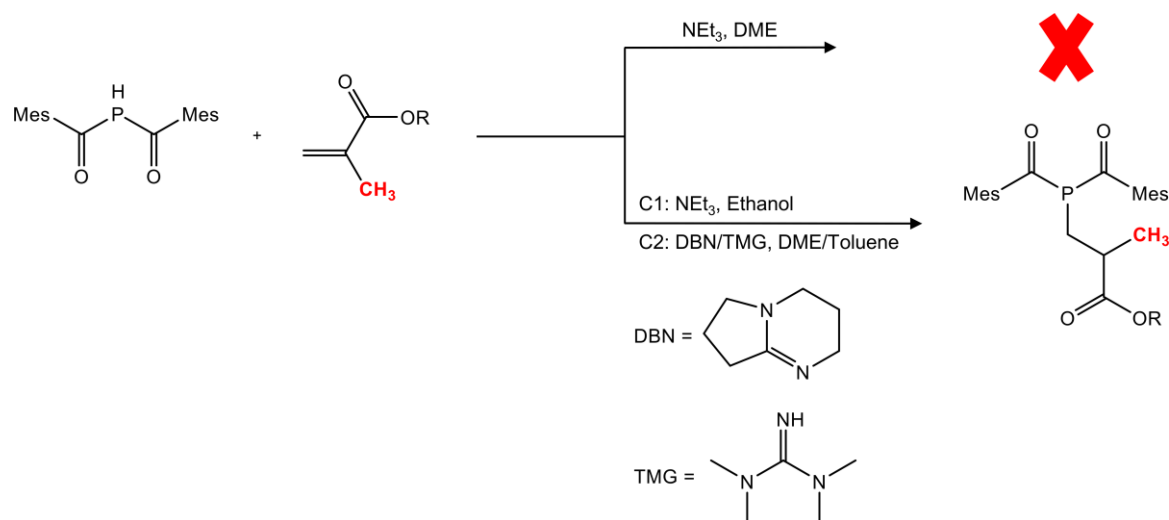
2 Synthesis of bis(acyl)phosphane oxide photoinitiators via phospha-Michael addition

2.1 Introduction

Phosphorus is one of the six biogenic elements in living systems.¹ Many natural products containing P-C bonds show important biological activities.² Similar to the well-established Michaelis-Arbuzov and Michaelis-Becker reactions, the phospha-Michael addition could become a versatile method to form P-C bonds.³ A library of P-functionalized BAPO derivatives were prepared through this synthetic strategy in the group of Prof. Grützmacher.^{4,5} In this process, acylphosphanes reacted readily with activated olefins in the presence of catalytic amounts of triethylamine (10 mol%) via a phospha-Michael addition (Scheme 2.1). Subsequently, the corresponding acylphosphane oxide photoinitiators were obtained in high yields after oxidation.



Scheme 2.1 General reaction scheme for phospha-Michael addition to obtain acylphosphane oxides. EWG = electron withdrawing group.



Scheme 2.2 General reaction scheme of phospho-Michael addition between bis(acyl)phosphane and methacrylates.

In this chapter, the method was further developed, resulting in a series of new bis(acyl)phosphane oxide derivatives for various applications. Particularly, the phospho-Michael addition between bis(acyl)phosphane and methacrylates (derivatives of methacrylic acid), which was inaccessible before, is also described (Scheme 2.2).

2.2 Synthesis of phosphane starting material: bis(2,4,6-trimethylbenzoyl)hydrogenphosphane (BAP-H, 1)

It was found that bis(2,4,6-trimethylbenzoyl)hydrogenphosphane (BAP-H) is a versatile starting material to prepare BAPO photoinitiators.⁵ Herein, an improved synthetic route to BAP-H (**1**) has been developed on a kilogram scale (Figure 2.1). The reaction of red phosphorus with three equivalents of sodium metal in the presence of 10 mol% naphthalene as promoter in dimethoxyethane (DME) results in Na_3P as a black suspension. Subsequent addition of an equimolar amount of *tert*-butanol and two equivalents of 2,4,6-trimethylbenzoyl chloride (MesCOCl) yielded sodium bis(mesityl)phosphide (BAP-Na) as a yellow solution. The desired product BAP-H (**1**) was obtained after the protonation of BAP-Na with acetic acid. The

salts generated during the synthesis were removed by washing with deionized water instead of filtration over Celite®. After recrystallization from toluene, BAP-H was obtained in excellent yield (90%), which is higher than the previous protocol (81 %).⁵ The air-stable crystalline yellow substance exists in an equilibrium between tautomers 1 and 1' in solution (Scheme 2.3).

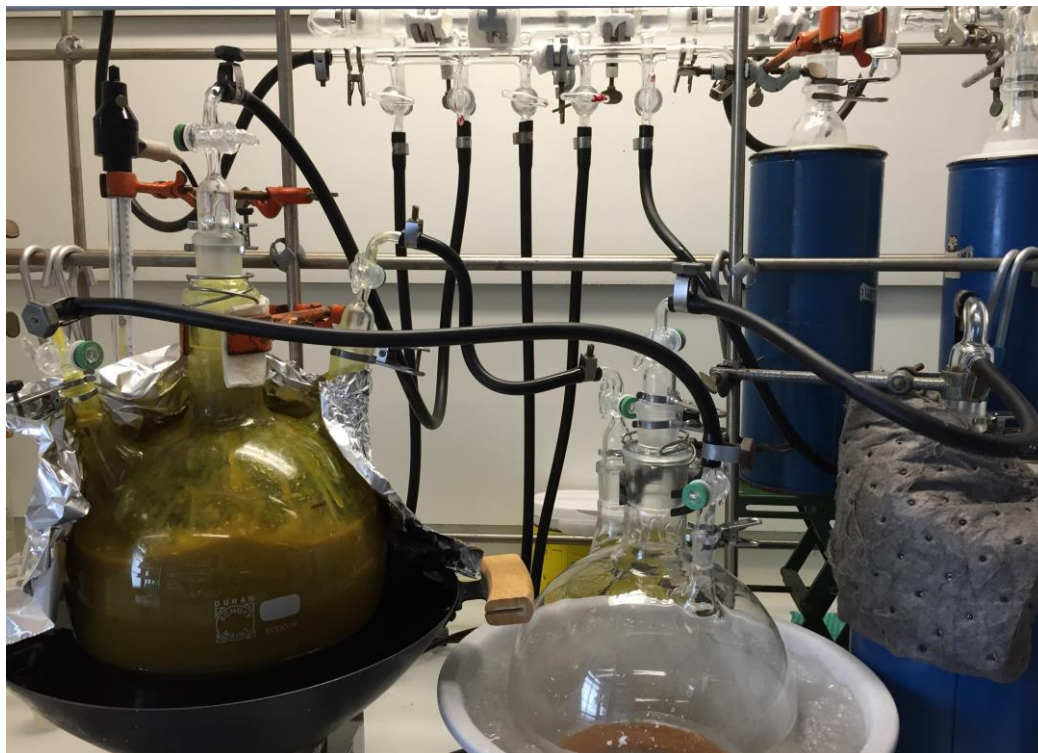
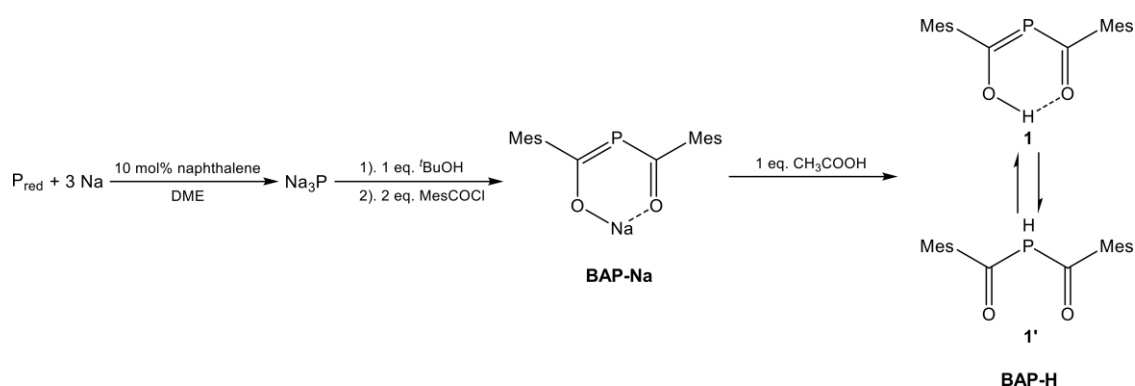


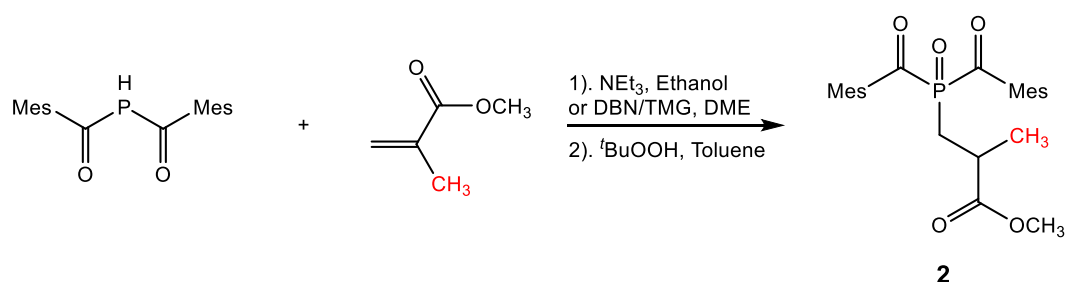
Figure 2.1 Synthesis of BAP-H on a kilogram scale.



Scheme 2.3 One-pot synthesis of BAP-H (1) from red phosphorus and sodium.

2.3 Synthesis of methyl 3-(bis(2,4,6-trimethylbenzoyl)phosphoryl)-2-methyl-propanoate (BAPO-MMA, 2)

Due to the electron-donating property of the α -methyl group, the addition of methyl methacrylate (MMA) with **1** is not available in DME as a solvent in the presence of trimethylamine (NEt_3 , $\text{pK}_a = 10.75^6$) as a catalyst. It was found that the P-C bond could be formed when a protic solvent, ethanol, was used instead of DME. Alternatively, 1,5-diazabicyclo(4.3.0)non-5-ene (DBN, $\text{pK}_a = 23.4^7$) or 1,1,3,3-tetramethylguanidine (TMG, $\text{pK}_a = 23.3^7$) in DME can be applied to the same purpose. Subsequently, the corresponding bis(acyl)phosphane oxide (**2**) was obtained in high yield after oxidation with *tert*-butyl hydroperoxide ($t\text{BuOOH}$). Based on this, surface functionalization of cellulose nanocrystals with an immobilized BAPO was achieved, see chapter 3.

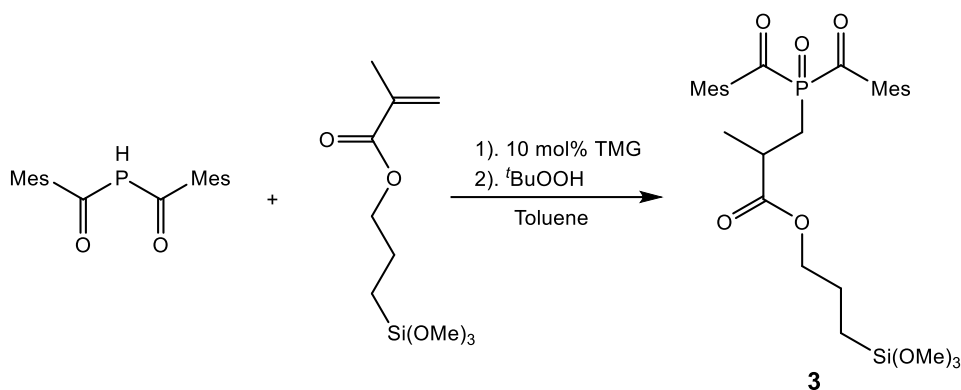


Scheme 2.4 Synthesis of BAPO-MMA (**2**).

2.4 Synthesis and application of 4-(trimethoxysilyl)butyl-3-[bis(2,4,6-trimethylbenzoyl)-phosphinoyl]-2-methyl-propionate (TMESI²-BAPO, 3)

A tri(methoxy)silyl-substituted BAPO derivative has been developed for grafting of fluorinated acrylates onto cotton fabrics in earlier work.⁸ However, the tedious synthetic process is the main limitation of this compound for broad use. To overcome this, we developed a simple

and efficient one-pot synthesis of a new tri(methoxy)silyl-substituted BAPO derivative in toluene. The Michael addition reaction of **1** onto 3-(trimethoxysilyl)propyl methacrylate, followed by the oxidation of the phosphane, provides TMESI²-BAPO (**3**) as a yellow oil in high yield (Scheme 2.5).



Scheme 2.5 Synthesis of TMESI²-BAPO (**3**).

TMESI²-BAPO (**3**) was successfully fixed to glass surfaces allowing coating via the “grafting-from” method (Figure 2.2). This was achieved by immersing the glass slide in an ethanol-water solution of **3** at 80 °C for four hours. **3** was thus grafted onto the glass surface via hydrolysis and condensation reactions taking place between the silanol groups present on the glass surface and the alkoxy silane groups in **3**. Subsequent irradiation with UV light in the presence of either a partially fluorinated acrylate (1H,1H,2H,2H-perfluorooctyl acrylate) or a specifically synthesized polysiloxane containing polymerizable acrylate functions (**4**, Scheme 2.6) allowed to generate polymer chains which grew from the surface in an efficient radical polymerization process (“grafting-from” procedure). Durable hydrophobic surfaces were prepared which give contact angles between 93° and 95°. The silanization process with the photoinitiator and the grafting process were followed and analyzed with various techniques including high-resolution X-ray photoelectron spectroscopy (XPS).⁹

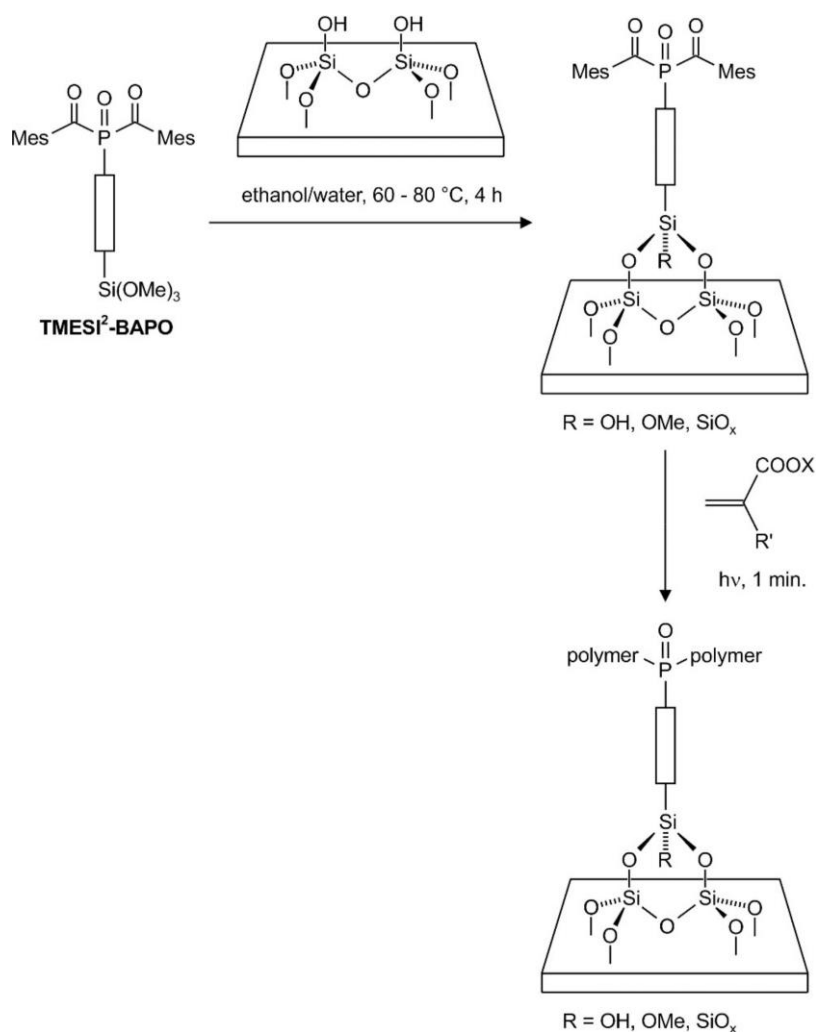
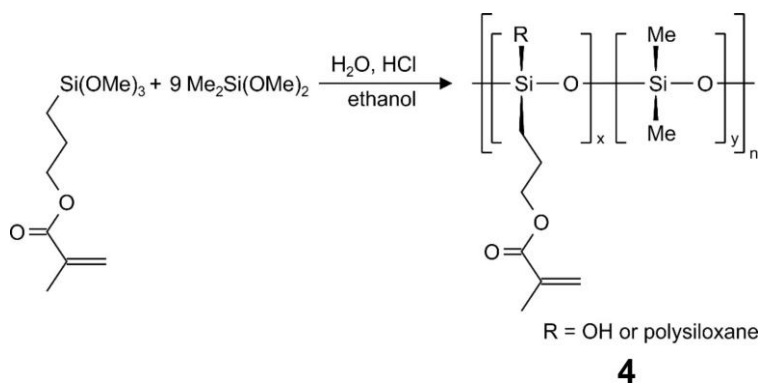


Figure 2.2 Schematic representation of the “grafting-from” process.



Scheme 2.6 Synthesis of acrylated polydimethylsiloxane (4)

TMESI²-BAPO (3) was also covalently attached onto silica particles to obtain photoactive inorganic fillers. The immobilization of the photoactive groups is evidenced by spectroscopic

measurements and thermal gravimetric analysis. The modified particles are then incorporated into thiol-ene resins to study the efficiency of the Norrish type I photofragmentation reaction of the covalently bound **3**. The photopolymerization kinetics of the thiol-ene system is monitored by FT-IR spectroscopy and photo-DSC upon prolonged exposure with UV-light and compared to the results achieved with Irgacure[®] 819. Rapid curing and high conversion yields were obtained evidencing the high efficiency of the photoactive particles. In addition, negative-toned patterns are inscribed in thin thiol-ene films by photolithographic processes and characterized by microscopic techniques demonstrating the versatile applicability of the photoactive particles. This offers a new approach for the efficient initiation of radical-mediated thiol-ene chemistry, whilst simultaneously reducing the amount of extractable and volatile residues in thiol-ene compounds. (Figure 2.3).¹⁰

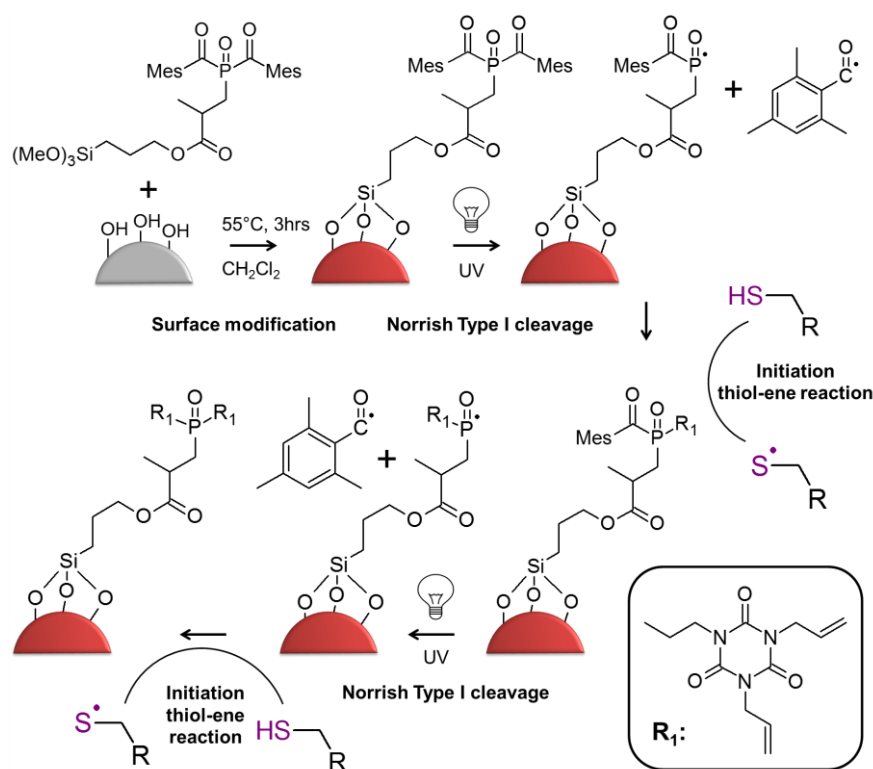


Figure 2.3 Schematic representation of the immobilization of TMESI²-BAPO on silica surfaces and subsequent photoinitiation of radical-mediated thiol-ene reactions.

2.5 Synthesis of multi-wave photoinitiators for producing star polymers via free radical polymerization

Star polymers consist of several linear polymer chains connected to a central point.¹¹ Unique shape and associated properties make them promising materials for a variety of applications, such as drug and gene delivery and imaging, thermoplastics and nanoelectronics.¹²⁻¹⁴ A broad range of star polymers have been realized through controlled polymerizations. However, few was achieved by free radical polymerization,¹⁵ which is more reasonable for industrial-scale synthesis. Two multifunctional PIs comprising three photoactive groups, which can be selectively excited at different irradiation wavelengths, are presented for the synthesis of compositional miktoarm star polymers via free radical photopolymerization (Figure 2.4).

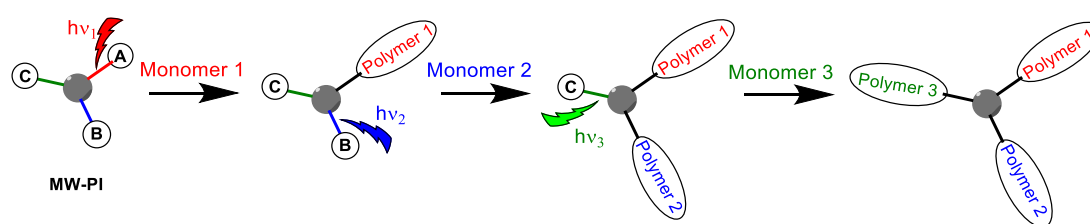
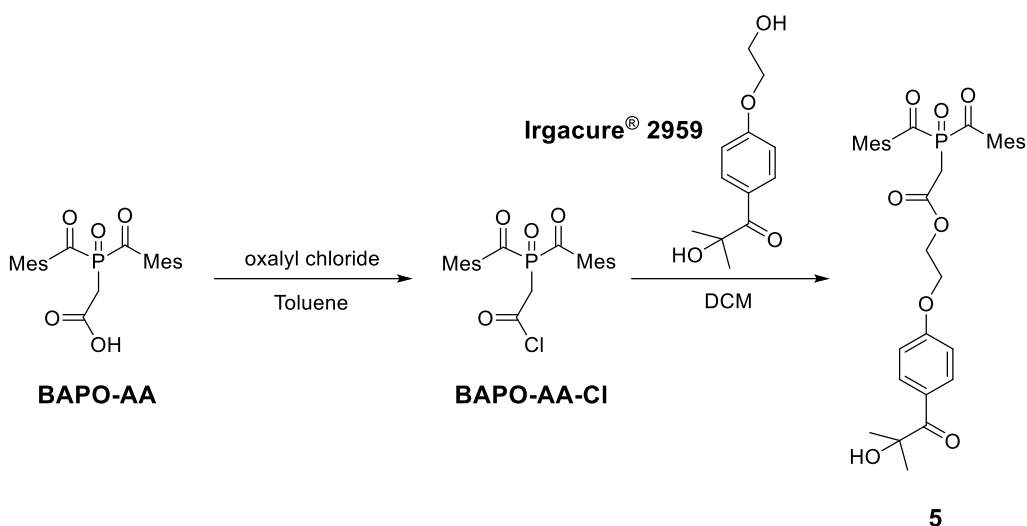


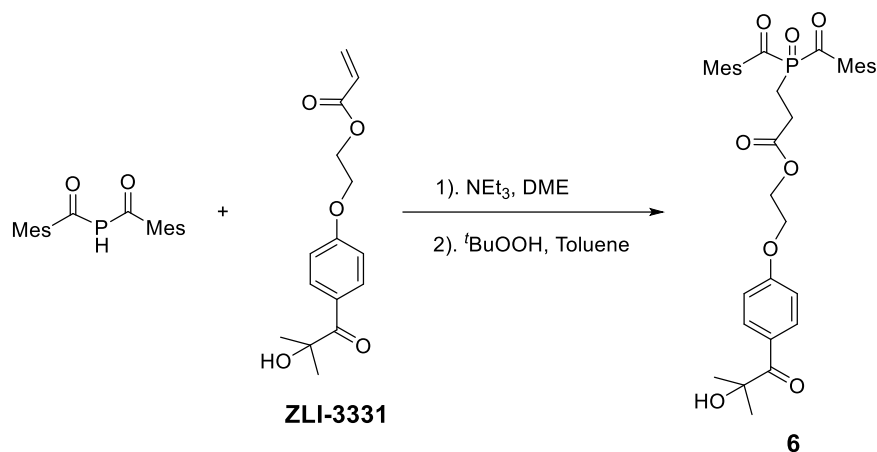
Figure 2.4 Schematic representation of multi-wave photoinitiators for producing star polymers.

A previous study revealed that block copolymers can be obtained by the BAPO Irgacure[®] 819, acting as two-step photoinitiator. Styrene was polymerized first by irradiation at 420 nm, followed by a second irradiation at 380 nm for the polymerization of methyl methacrylate.¹⁶ By attaching an α -hydroxy ketone (Irgacure[®] 2959), which absorbs at shorter wavelengths than the BAPO, the tri-functional PIs were obtained to prepare star polymers (compound **5** and **6**).



Scheme 2.7 Synthesis of 2-(4-(2-hydroxy-2-methylpropanoyl)phenoxy)ethyl 2-(bis(2,4,6-trimethylbenzoyl)phosphoryl)acetate (**5**).

First, **BAPO-AA** was converted to the corresponding acid chloride (**BAPO-AA-Cl**) in the presence of excess amount of oxalyl chloride. Subsequent reaction with Irgacure[®] 2959 generates the desired product **5** as a yellow solid (prepared by Dr. Alex Huber, Scheme 2.7).



Scheme 2.8 Synthesis of 2-(4-(2-hydroxy-2-methylpropanoyl)phenoxy)ethyl 3-(bis(2,4,6-trimethylbenzoyl)phosphoryl)propanoate (**6**).

6 was prepared in a more convenient way. The Michael addition of **1** onto 4-(2-acryloyloxyethoxy)phenyl-2-hydroxy-2-propyl ketone (**ZLI-3331**), followed by the oxidation

with t BuOOH, provides 2-(4-(2-hydroxy-2-methylpropanoyl)phenoxy)ethyl 3-(bis(2,4,6-trimethylbenzoyl)phosphoryl)propanoate (**6**) as a yellow solid in good yield (Scheme 2.8).

5 and **6** were both tested for synthesizing star polymers (Figure 2.5): The first benzoyl moiety of the BAPO is addressed by LED at 420 nm, followed by the MAPO-type benzoyl moiety of the macroinitiator **I2** (LED at 400 nm or 385 nm). Finally, the α -hydroxy ketone of **I3** reacts by irradiation with a Hg-Xe UV lamp ($\lambda_{\text{max}} = 365$ nm).

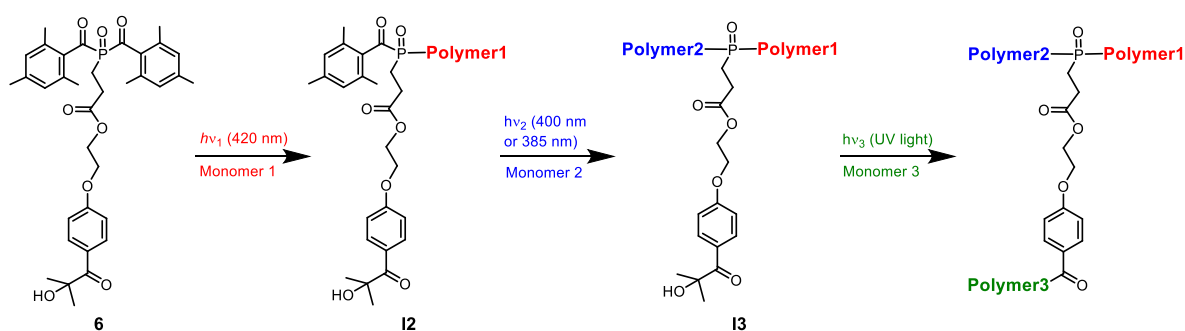


Figure 2.5 Strategy for star polymer synthesis based on absorption properties. Compound **6** was chosen for demonstration.

As a proof of concept, a polymer containing three poly(methyl methacrylate) (pMMA) blocks was prepared using **5** as the photoinitiator. Diblock and star polymer formation is evident from size-exclusion chromatography (SEC) analysis (Table 2.1), showing an increase in M_n as well as M_w after each polymerization step.

The successful synthesis of multi-wave PIs **5** and **6** enabled the preparation of strictly defined star polymers by performing successive radical polymerizations. This provides access to materials with tailor-made properties under robust and environmentally favorable conditions.

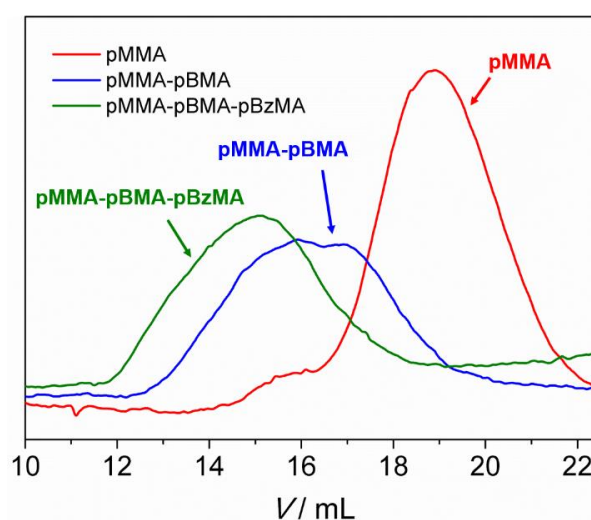
Table 2.1 SEC analysis of pMMA, pMMA-pMMA and pMMA-pMMA-pMMA synthesized with **5**.

Sample	$M_n / 10^3$ [g/mol]	$M_w / 10^3$ [g/mol]	M_w/M_n
pMMA	5.1	15.4	3.04
pMMA-pMMA	9.0	51.0	5.69
pMMA-pMMA-pMMA	13.1	56.9	4.33

A star polymer consisting of three different polymer blocks was synthesized with **6**, utilizing the monomers MMA, butyl methacrylate (BMA) and benzyl methacrylate (BzMA). SEC data presented in Table 2.2 and Figure 2.6 confirms the success of diblock and star polymer synthesis.

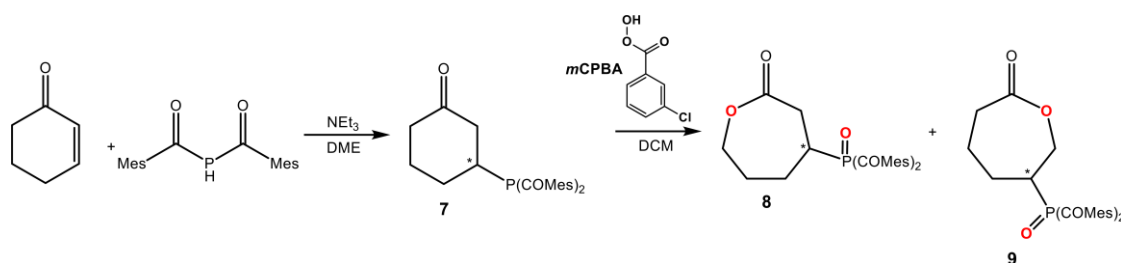
Table 2.2 SEC analysis of pMMA, pMMA-pBMA and pMMA-pBMA-pBzMA synthesized with **6**.

Sample	$M_n / 10^3$ [g/mol]	$M_w / 10^3$ [g/mol]	M_w/M_n
pMMA	4.6	14.5	3.13
pMMA-pBMA	35.2	125.7	3.57
pMMA-pBMA-pBzMA	110.2	309.5	2.81

**Figure 2.6** SEC curves of pMMA, the diblock copolymer pMMA-pBMA and the star polymer pMMA-pBMA-pBzMA.

2.6 Synthesis of BAPO functionalized ϵ -caprolactones

Aliphatic polyesters are being used in various fields, ranging from agricultural implements to biomedical applications.¹⁷ Lactones and lactides are key monomers used to prepare versatile aliphatic polyesters.¹⁸ Polycaprolactones (PCLs) are of great interest for tissue engineering and drug delivery, due to their biodegradability and biocompatibility.¹⁹ Herein, BAPO functionalized ϵ -caprolactones (BAPO-CLs) were synthesized by the efficient phospho-Michael addition of **1** onto cyclohex-2-en-1-one and subsequent Baeyer–Villiger oxidation of the cyclohexanone derivative (Scheme 2.9).



Scheme 2.9 Synthesis of BAPO functionalized ϵ -caprolactones.

3-BAP-substituted cyclohexanone (**7**) was prepared by using the commercially available cyclohex-2-en-1-one as the starting material and triethylamine as the catalyst. Subsequent Baeyer-Villiger oxidation was performed under conventional reaction conditions, using *meta*-chloroperoxybenzoic acid (*m*CPBA) as oxidant and dichloromethane as solvent.

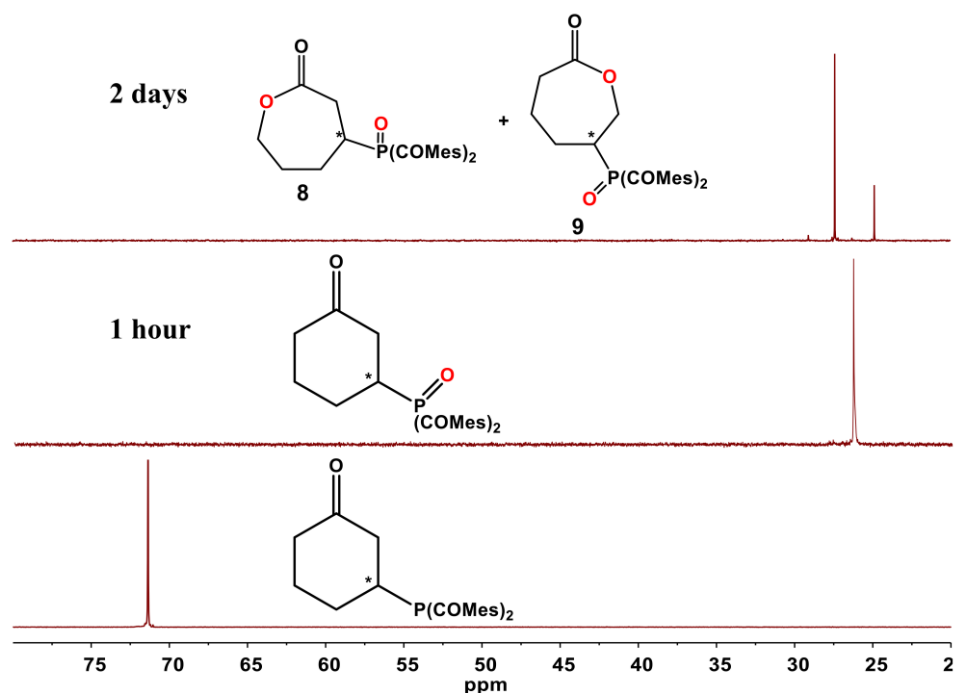


Figure 2.7 ^{31}P NMR studies during the Baeyer–Villiger oxidation.

^{31}P NMR studies during oxidation revealed that the phosphane was oxidized first, full conversion to phosphane oxide was observed in one hour. The subsequent oxidation of the ketone to the ester took 2 days after stirring the reaction mixture at room temperature in the presence of an excess of *m*CPBA (Figure 2.7). 4-BAPO-substituted lactone (**8**) and 6-BAPO-substituted lactone (**9**) were obtained with a ratio of 1 : 0.28. These two compounds could be used as monomers to obtain photoactive poly(ϵ -caprolactones) by a controlled ring-opening polymerization.

2.7 Conclusion

The phospho-Michael addition of BAP-H (**1**) to a broad range of activated olefins offers an atom economic and convenient process to prepare substituted bis(mesityl)phanes (BAPs), which can be easily oxidized to afford the corresponding BAPOs. With these functionalized

PIs, interesting applications such as surface modifications, photoactive and star polymer synthesis, can be achieved.

2.8 References

1. C. C. Cummins. *Dædalus*, 2014, **143**, 9-20.
2. H. Seto, T. Kuzuyama. *Nat. Prod. Rep.*, 1999, **16**, 589-596.
3. D. Enders, A. Saint-Dizier, M. I. Lannou and A. Lenzen. *Eur. J. Org. Chem.*, 2006, **1**, 29-49.
4. H. Grützmacher and G. Müller. A Process for The Preparation of Acylphosphanes. EP 2903995A1, WO2014053455A1.
5. G. Müller. Phosphorus based photoinitiators: Synthesis and application. Dissertation No. 21309, ETH Zürich, Zürich, 2013.
6. See Evans' a pKa table, http://evans.rc.fas.harvard.edu/pdf/evans_pKa_table.pdf
7. W. Galezowski, A. Jarczewski, M. Stanczyk, B. Brzezinsky, F. Bartl and G. Zundel. *J. Chem. Soc., Faraday Trans.*, 1997, **93**, 2515-2518.
8. Huber, A.; Kuschel, A.; Ott, T.; Santiso-Quinones, G.; Stein, D.; Bräuer, J.; Kissner, R.; Krumeich, F.; Schönberg, H.; Levalois- Grützmacher, J.; Grützmacher, H. *Angew. Chem. Int. Ed.*, 2012, **51**, 4648-4652.
9. Sangermano, M.; Periolatto, M.; Castellino, M.; Wang, J.; Dietliker, K.; Grützmacher, J. L.; Grützmacher, H., A Simple Preparation of Photoactive Glass Surfaces Allowing Coatings via the "Grafting-from" Method. *ACS Applied Materials & Interfaces* 2016, **8**, 19764-19771.
10. Sahin, M.; Schlögl, S.; Kaiser, S.; Kern, W.; Wang, J.; Grützmacher, H., Efficient initiation of radical-mediated thiol-ene chemistry with photoactive silica particles. *Journal of Polymer Science Part A: Polymer Chemistry* 2017, **55**, 894-902.
11. Ren, J. M.; McKenzie, T. G.; Fu, Q.; Wong, E. H. H.; Xu, J.; An, Z.; Shanmugam, S.; Davis, T. P.; Boyer, C.; Qiao, G. G. *Chem. Rev.*, 2016, **116**, 6743-6836.
12. Hildebrandt, K.; Kaupp, M.; Molle, E.; Menzel, J. P.; Blinco, J. P.; Barner-Kowollik, C. *Chem. Commun.*, 2016, **52**, 9426-9429.
13. Ding, H.; Park, S.; Zhong, M.; Pan, X.; Pietrasik, J.; Bettinger, C. J.; Matyjaszewski, K. *Macromolecules*, 2016, **49**, 6752-6760.
14. Lapienis, G. *Prog. Polym. Sci.*, 2009, **34**, 852-892.
15. Gao, H.; Matyjaszewski, K. *Chem. Eur. J.*, 2009, **15**, 6107-6111.
16. Gunersel, E. D.; Hepuzer, Y.; Yagci, Y. *Angew. Makromol. Chemie*, 1999, **264**, 88-91.

17. Hillmyer, M. A.; Tolman, W. B., Aliphatic Polyester Block Polymers: Renewable, Degradable, and Sustainable. *Accounts of Chemical Research*, 2014, **47**, 2390-2396.
18. Winkler, M.; Raupp, Y. S.; Köhl, L. A. M.; Wagner, H. E.; Meier, M. A. R., Modified Poly(ϵ -caprolactone)s: An Efficient and Renewable Access via Thia-Michael Addition and Baeyer–Villiger Oxidation. *Macromolecules*, 2014, **47**, 2842-2846.
19. Labet, M.; Thielemans, W., Synthesis of polycaprolactone: a review. *Chemical Society Reviews*, 2009, **38**, 3484-3504.

3 Surface functionalization of cellulose nanocrystals for polymer grafting

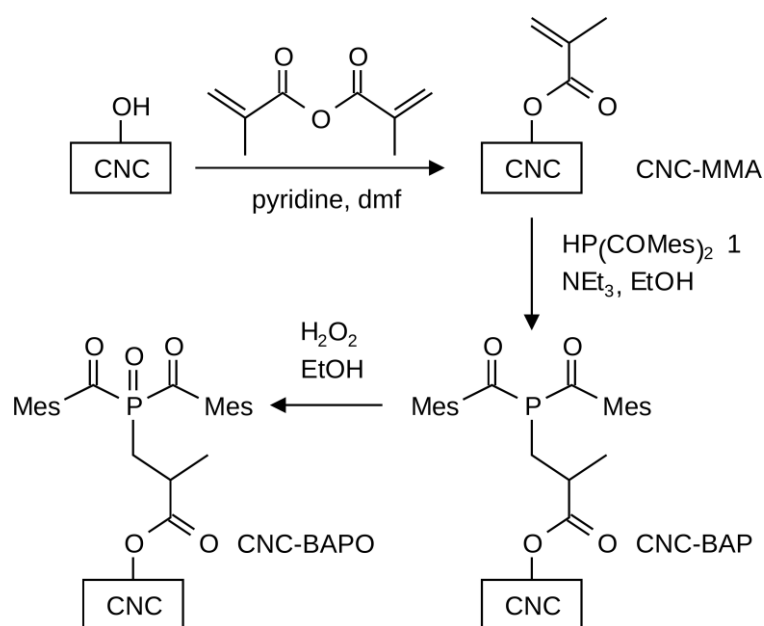
3.1 Introduction

Cellulose nanocrystals (CNCs), which are generated by hydrolysis of cellulose fibers, have attracted tremendous attention in the past few years.¹⁻⁵ This material can be used as reinforcing fillers, security papers, emulsifying agents and medical implants, owing to its excellent mechanical properties, optical transparency, biodegradability, and renewability.⁶⁻¹¹ However, the inherent hydrophilicity and self-aggregation upon drying often limit its applications. Polymer grafting offers a way to overcome these obstacles. The two most commonly used approaches are “grafting onto” and “grafting from”.^{12,13} In the former approach, the pre-synthesized polymer chains are attached to hydroxyl groups on the surfaces via reactive end groups. The latter method consists of mixing the cellulose with monomers and initiators to induce polymerization from the surfaces, which gives high grafting densities due to less steric hindrance.¹⁴ Free radical polymerization (radicals are generated by various methods from an initiator in the presence of cellulose and monomer),¹⁵⁻¹⁷ controlled radical polymerization [atom transfer radical polymerization (ATRP)¹⁸ or reversible addition–fragmentation chain transfer polymerization (RAFT)¹⁹], and ring opening polymerization²⁰ (cellulose surface hydroxyl groups act as initiating sites) were used as the “grafting from” strategy. Free radical polymerization is able to polymerize a wide range of monomers in a short time and is tolerant to water or other impurities, but rather harsh conditions are required to generate radicals in most cases.

In this chapter, a new “grafting from” approach to functionalize CNC surfaces via free radical polymerization of acrylic monomers initiated by an immobilized photoinitiator bis(acyl)phosphane oxide (BAPO) is discussed.

3.2 Synthesis and Characterization

In order to functionalize CNCs (derived from wood pulp by sulfuric acid treatment, provided by the University of Maine), methacryloyl groups were attached to their surfaces as shown in Scheme 3.1. To these, BAP-H (**1**) was added to give CNC-BAP and subsequent oxidation with aqueous H₂O₂ generated quantitatively CNC-BAPO. Elemental analysis of the final yellow powder indicates a phosphorus content of 1.0% which corresponds to 0.33 mmol bis(acyl)phosphane oxide (BAPO) per gram of CNC.



Scheme 3.1 Functionalization of cellulose nanocrystals with a BAPO photoinitiator. Mes = mesityl.

The successful immobilization was confirmed by Fourier transform infrared spectroscopy (FT-IR), see Figure 3.1. The peaks at 1716 cm⁻¹ and 1635 cm⁻¹ in the CNC-

MMA sample are attributed to the stretching vibration of the carbonyl ($\nu_{C=O}$) and alkene groups ($\nu_{C=C}$), respectively. After the addition of BAPO, a new absorption at 1608 cm^{-1} is observed which is assigned to the stretching vibration of the C=C bonds in the mesityl (Mes) ring while $\nu_{C=O}$ is shifted to a higher wavenumber at 1732 cm^{-1} .

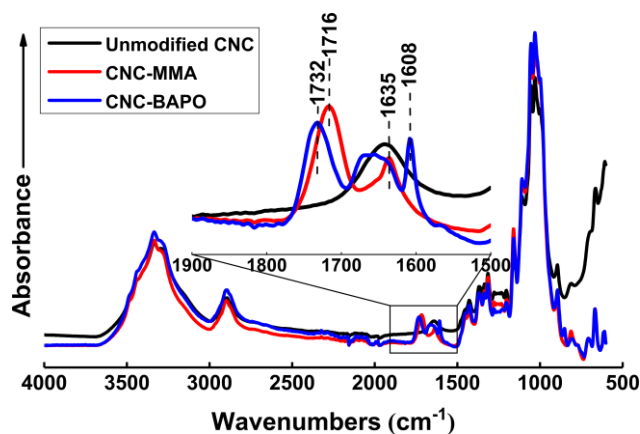


Figure 3.1 FT-IR spectra of unmodified CNC, CNC-MMA and CNC-BAPO.

The presence of BAPO was further proved by ^{13}C and ^{31}P CP-MAS NMR spectroscopy (Figure 3.2). A single signal at 23.7 ppm in ^{31}P CP-MAS NMR spectrum of CNC-BAPO is characteristic for an alkyl bound BAPO group. Typical ^{13}C signals of cellulose nanocrystals at $\delta = 105.0$ (C_1), 88.6 (C_4 crystalline), 83.8 (C_4 amorphous), 74.7/72.4 ($\text{C}_{2,3,5}$), 65.0 (C_6 crystalline), and 62.9 ppm (C_6 amorphous) are observed in all spectra.²¹ In the CNC-BAPO sample, the characteristic signals of the BAPO unit at $\delta = 216.4$ (COMes), 141.4 (C^4 Mes), 136.1 ($\text{C}^{2,6}$ Mes), 129.4 ($\text{C}^{3,5}$ Mes), and 20.0 (*o,p*-CH₃ Mes) are clearly observed, which are absent in the spectrum of CNC-MMA. The ^{13}C signal of the C=O group from methacrylate unit is shifted from 168.1 to 174.7 ppm, due to the addition of the BAPO group.

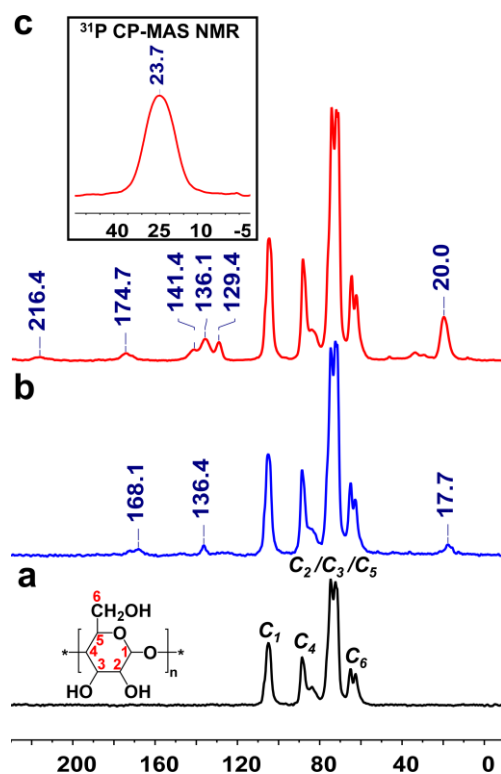


Figure 3.2 ^{13}C CP-MAS NMR spectra of: (a) unmodified CNC, (b) CNC-MMA, (c) ^{13}C and ^{31}P CP-MAS NMR spectra of CNC-BAPO.

Table 3.1 Gravimetrically determined graft yield (G), graft efficiency (G_E), molecular weight and polydispersity (PDI) of the cleaved polymers after grafting to CNC, and results from elemental analyses.

Sample	G (%)	G_E (%)	M_n (kg/mol)	M_w (kg/mol)	PDI	C (%)	H (%)	P (%)	S (%)
Unmodified CNC						41.88	6.40		1.00
CNC-MMA						43.43	6.27		0.95
CNC-BAPO						46.10	6.32	1.02	0.60
CNC-g-PMMA	477.2	79.7	76.7	250.6	3.27	57.07	7.99	0.16	0.11
CNC-g-PBuA	311.2	75.4	9.5	17.4	1.82	61.02	9.06	0.21	0.13
CNC-g-PNIPAAm	292.4	73.5	25.2	69.5	2.76	58.41	9.37	0.21	0.12
CNC-g-PHEA	197.8	66.3				48.85	6.96	0.30	0.16

The sulfur content decreased after adding BAPO, which is likely caused by nucleophilic displacement of the sulfate group, which acts as leaving group.

The TEM images in Figure 3.3 show that the morphology of the CNC was maintained during the modification procedure with BAPO units. The unmodified nanocrystals exhibit an average diameter of 5-10 nm and lengths of 100-150 nm. The BAPO functionalized nanocrystals are

less individualized. This aggregation may be due to a decrease of sulfate groups or activation of the surface BAPO groups under the conditions of the TEM experiment (Table 3.1).

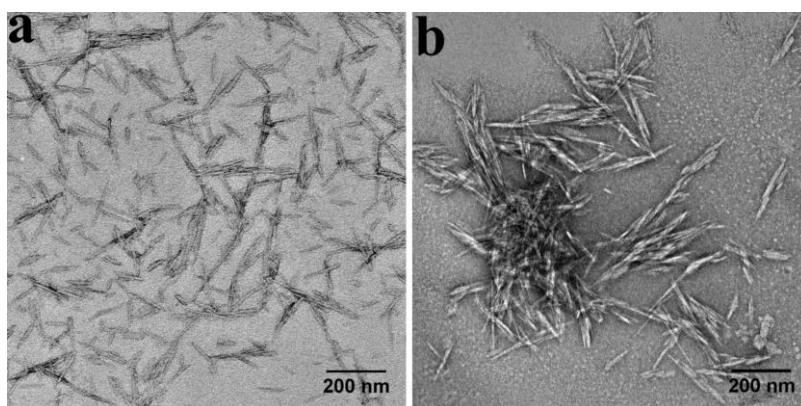


Figure 3.3 Transmission electron micrographs of unmodified CNC (a), and CNC-BAPO (b).

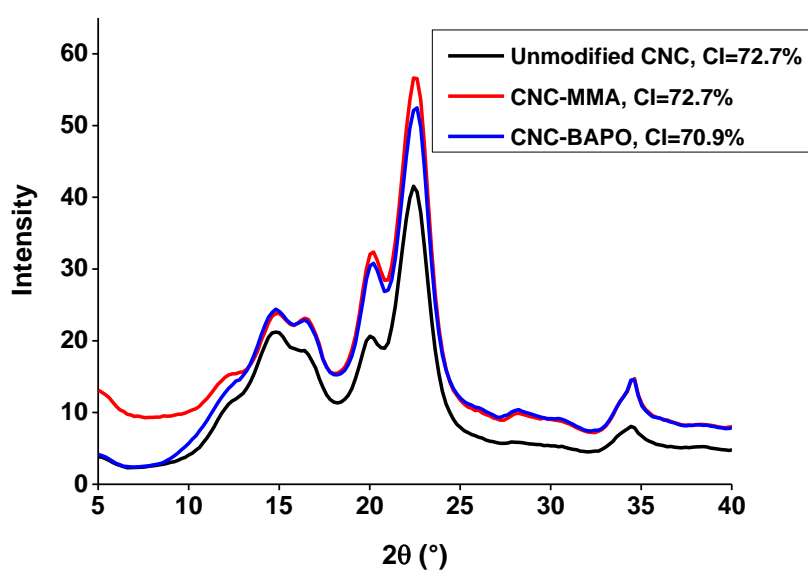
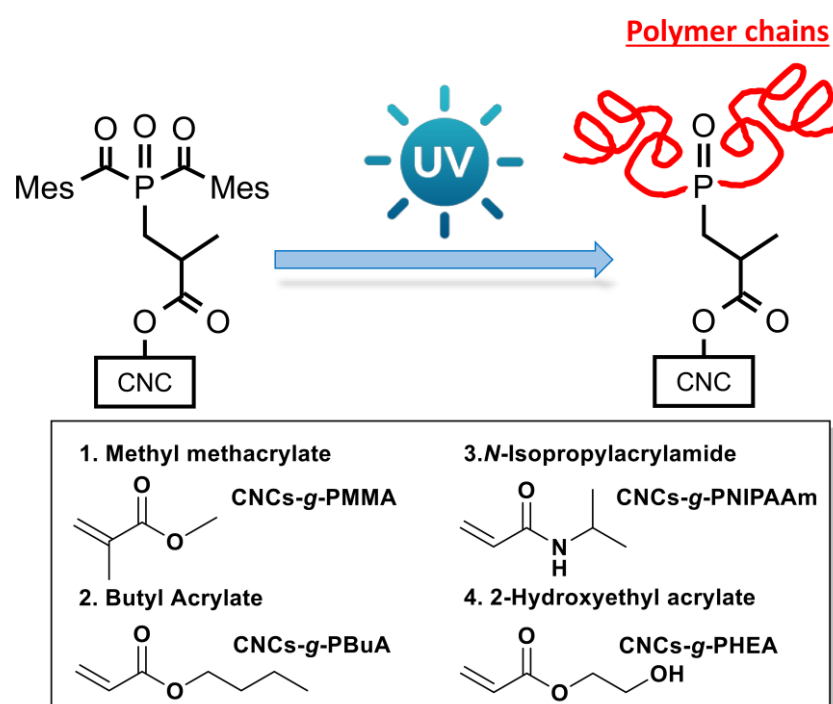


Figure 3.4 X-ray diffraction patterns of the unmodified, methacrylate and BAPO functionalized nanocrystals with crystallinity indices.

The X-ray diffraction patterns of unmodified CNC, methacrylate, and BAPO modified CNC show that all three samples have similar crystallinity and exhibit patterns

typical of the native crystalline form of cellulose I β (Figure 3.4). Similar crystallinity indices (CI) around 72% were determined for unmodified CNC, CNC-MMA and CNC-BAPO, respectively. This suggests that the modification is limited to the surfaces of CNCs.

3.3 Polymer Grafting



Scheme 3.2 Graft polymerization of CNC-BAPO.

CNC-BAPO was used to polymerize acrylic monomers under UV light irradiation at room temperature for 1 hour. The dimension of CNC was preserved after UV irradiation (Figure 3.5). The monomers used include methyl methacrylate (MMA), butyl acrylate (BuA), N-isopropylacrylamide (NIPAAm) and 2-hydroxyethyl acrylate (HEA). Graft yield (G), graft efficiency (G_E) and elemental analysis of the polymer graft CNC are recorded in Table 3.1.

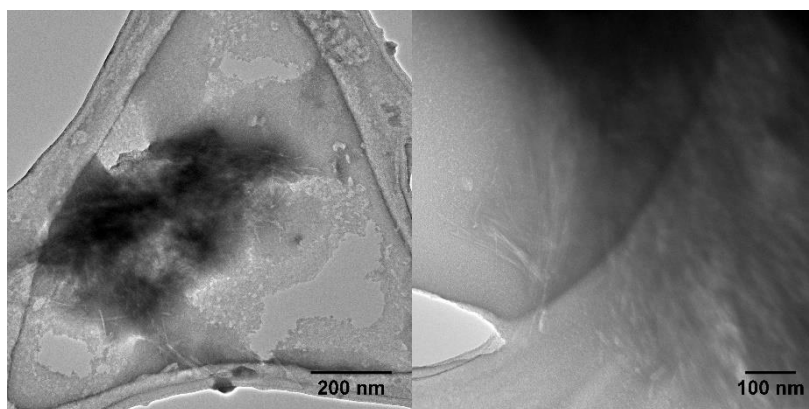


Figure 3.5 Transmission electron micrographs of CNC-BAPO after UV irradiation in the absence of monomer. Cellulose nanocrystals were crosslinked, but the dimension was preserved.

High graft yields (after removing the homopolymers by Soxhlet extraction) were obtained for all tested monomers. The highest mass gain of up to 477% was achieved with MMA. BuA and NIPAAm both formed grafted polymers with masses three times greater than that of the starting CNC. HEA was less prone to graft, but the mass still increased by 200%. Elemental analysis was performed to quantify the composition of the grafted materials. The mass gain calculated according to phosphorus content correlates well with the gravimetric value. Homopolymers, generated by cleaved acyl radicals, were formed in smaller amounts which confirms that phosphinoyl radicals are more reactive than acyl radicals.²²

The obtained samples were characterized by FT-IR (Figure 3.6). Intense absorption bands attributed to the $\nu_{C=O}$ of the carboxyl groups of the grafted polymers were observed in all spectra. The bending vibration of the N-H bond was detected at 1531 cm^{-1} in the CNC-*g*-PNIPAAm sample. Moreover, the intensities of the O-H stretching bands of cellulose backbones at 3300 cm^{-1} decreased significantly in PMMA and PBuA grafted samples. This is likely caused by the grafting of the polymers from the CNC surfaces.²⁰ In contrast, the intensities increased in the PNIPAAm and PHEA grafted samples, due to the overlapping of N-H and O-H groups present in the grafted polymer chains.

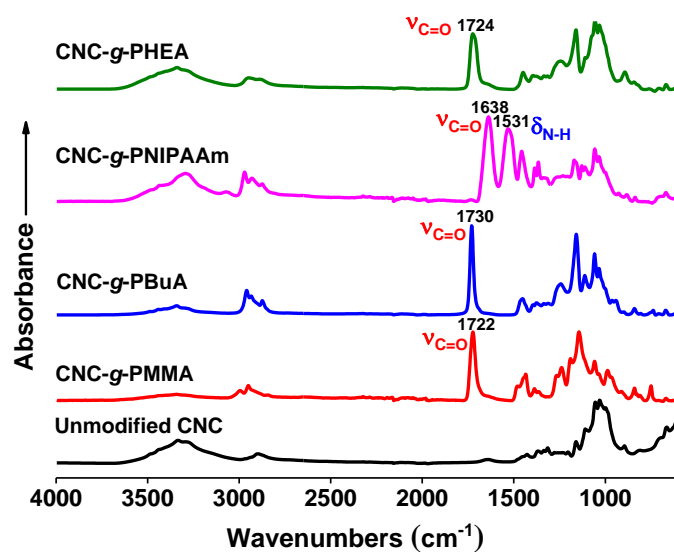


Figure 3.6 FT-IR spectra of the polymer grafted samples.

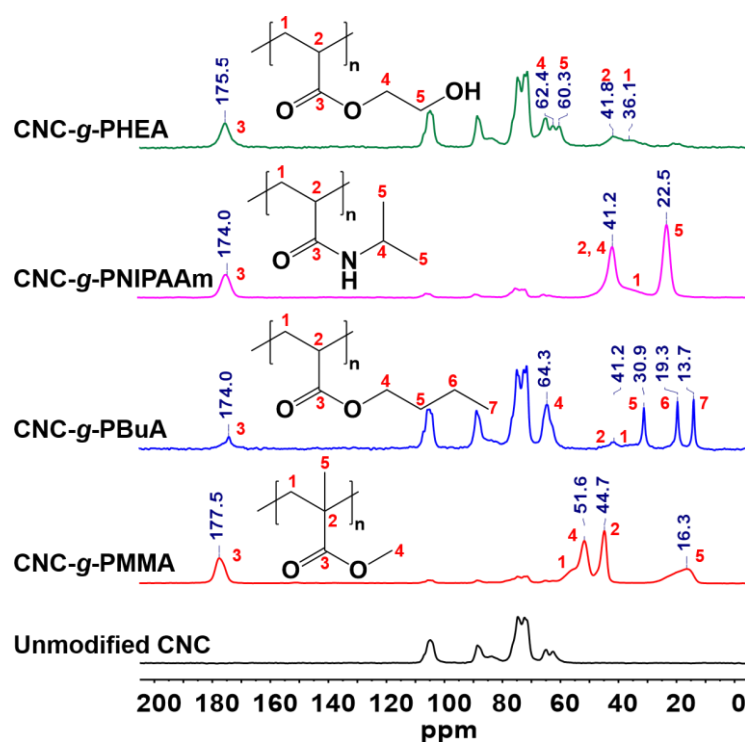


Figure 3.7 ^{13}C CP-MAS NMR spectra of the polymer grafted samples with assignments of resonances.

^{13}C CP-MAS NMR spectroscopy was used to characterize the polymer grafted CNC. In addition to the signals of cellulose, the resonances of the ^{13}C nuclei in the polymers were clearly observed, confirming the success of grafting (Figure 3.7).

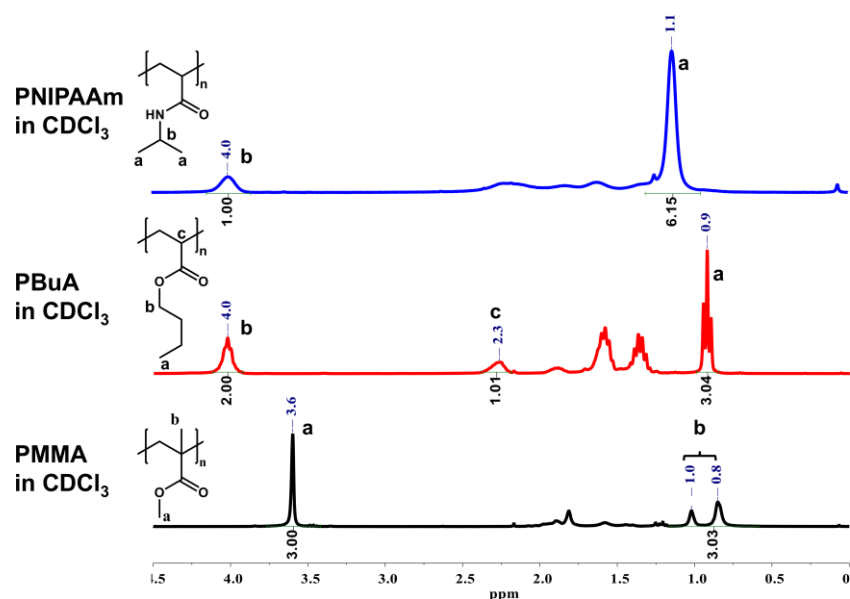


Figure 3.8 ^1H NMR spectra of the cleaved polymers with assignments of resonances.

The grafted polymer chains were cleaved from the CNC and independently investigated. ^1H NMR indicated that the structures were maintained except for PHEA (Figure 3.8). The molecular weight of the polymers varies with the monomer (see Table 3.1). MMA generated the longest chains, and the weight average molecular weight (M_w) is 250 kg/mol. BuA and NIPAAm gave shorter chains with M_w of about 17 kg/mol and 70 kg/mol, respectively.

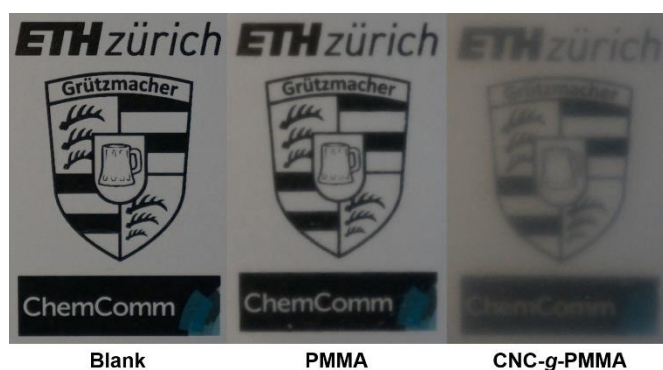


Figure 3.9 Pictures of solvent casting films. Blank: background picture without film (left), with PMMA film (middle), and with CNC-g-PMMA film (right). Films of about 0.1 mm thickness were placed about 2 cm above the background and photographed.

Polymeric films of CNC-*g*-PMMA can be obtained by solvent casting, because of sufficiently long polymer chains. A film of about 0.1 mm thickness is shown to the right of Figure 3.9 and is less transparent than a neat PMMA film (Figure 3.9 middle).

3.4 Properties of grafted hybrid materials.

In order to confirm the efficiency of the surface modification, the behavior of dispersions of unmodified and polymer grafted CNC were examined in THF. As shown in Figure 3.10, the unmodified CNC suspension sedimented quickly, the polymer grafted samples remained dispersed for more than four hours and still exhibited noticeable turbidity after 24 hours.

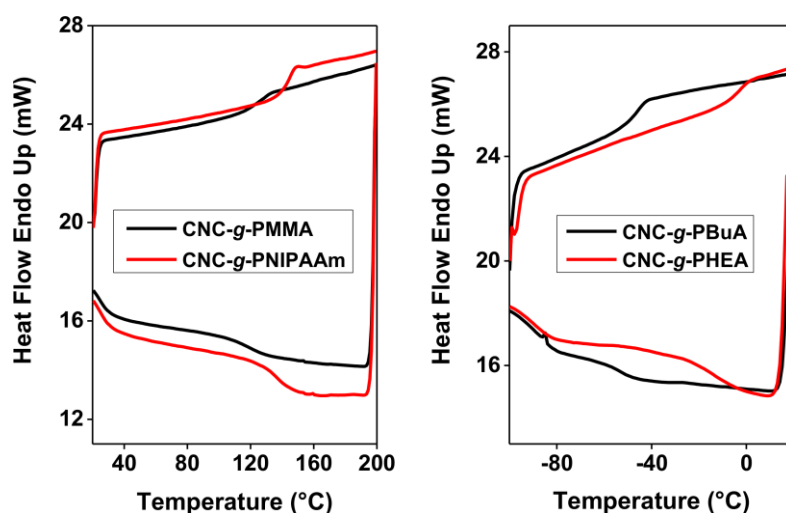


Figure 3.10 Dispersion test of unmodified and polymer grafted cellulose nanocrystals (0.5 wt%) in THF. The CNC-*g*-PHEA sample was not tested, since the homopolymer is insoluble in THF. Pictures recorded: immediately after stirring stopped (top), and four hours later (bottom).

Table 3.2 TGA and DSC data of samples

Sample	TGA			DSC		T_g [°C]
	$T_{5\%}^{[a]}$ [°C]	$T_m^{[b]}$ [°C]	$Y_c^{[c]}$ [%]	$T_H^{[d]}$ [°C]	$T_C^{[e]}$ [°C]	
Unmodified CNC	251	306	0.8			
CNC-BAPO	247	294	18.3			
CNC-g-PMMA	241	397	1.3	123	114	105 ^[f]
CNC-g-PBuA	275	420	5.6	-46	-51	-54 ^[f]
CNC-g-PNIPAAm	273	417	3.7	143	136	130 ^[f]
CNC-g-PHEA	277	447	1.3	-4	-13	-15 ^[g]

[a] Temperature at which 5 % weight loss occurred. [b] Temperature at which the maximum rate of degradation is observed. [c] Char yield at 800°C. [d] Glass transition temperature during heating. [e] Glass transition temperature during cooling. [f] Reference values of homopolymers from Polymer handbook (4th ed.), John Wiley & Sons, 1999, pp. 199-204. [g] Reference value from CRC Handbook of Enthalpy Data of Polymer-Solvent Systems, CRC Press, 2006, page 423.

**Figure 3.11** DSC thermograms of grafted samples, the data of cooling and reheating were recorded.

DSC and TGA thermograms were recorded (Figure 3.11 and 3.12, respectively, and Table 3.2). Glass transition temperatures (T_g) of the grafted products are slightly higher than the reported values of the homopolymers. The increase can be explained by the restriction of the mobility of grafted polymer chains to the CNC surfaces.²³ In TGA thermograms, a significant increase of the onset temperature was observed for CNC grafted with PBuA, PNIPAAm and PHEA. The char yield of CNC-BAPO sample at 800 °C (18.3%) is much higher than the others

because on cellulose substrates, organo phosphorus compounds favor char formation and suppress the concentration of combustible volatile species during thermal decomposition.²⁴

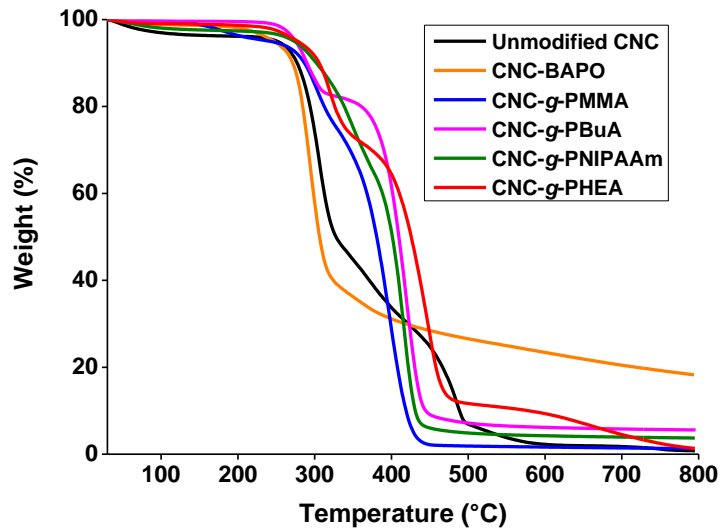


Figure 3.12 TGA thermograms of samples.

The reinforcing properties of CNC-g-PMMA in a PMMA matrix were evaluated by tensile tests. The elastic modulus (E), tensile strength (σ), and elongation at break of the specimens are given in Figure 3.13. The incorporation of unmodified CNC (20 wt%) in a PMMA matrix decreases both the elastic modulus and the tensile strength by 25% and 56%, respectively. This finding can be explained by the poor compatibility between the hydrophilic CNC and the hydrophobic PMMA. The addition of CNC-g-PMMA (20 wt%) into PMMA proved to enhance the elastic modulus by 8% without loss of the tensile strength. Elongation at break decreases significantly but the values still remain better than the composites filled with unmodified CNC.

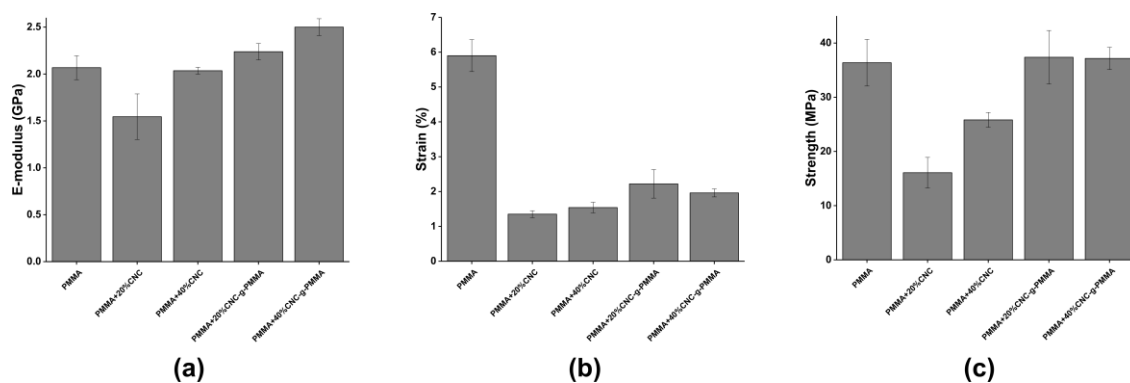


Figure 3.13 Tensile tests of PMMA composites. (a) Elastic modulus, (b) Tensile strength, (c) Elongation at break.

3.5 Conclusion

A new approach to modify CNCs with an immobilized bis(acyl)phosphane oxide was developed. The functionalized CNCs were used for polymer grafting. Under mild and acid-free conditions, excellent graft yields were achieved. The obtained hybrid materials have been characterized and show long-term dispersion stability in THF. The PMMA grafted CNCs show an improved mechanical performance when dispersed in a PMMA matrix.

3.6 Methods

3.6.1 Materials

Cellulose nanocrystals were purchased from the University of Maine, with a sulfur content of 0.99%, and were purified by Soxhlet extraction with ethanol for 24 h before further modification.²⁵ Acrylates were passed through basic alumina columns to remove inhibitors immediately before the polymerization experiment, except *N*-isopropylacrylamide, which was recrystallized from hexane three times. Poly(methyl methacrylate) was obtained from Alfa Aesar with $M_w = 550$ kDa.

3.6.2 Synthesis of CNC-MMA

CNC-MMA was prepared according to a modified literature procedure.²⁶ In a 500 mL Schlenk flask, 5.06 g dry CNCs (about 94 mmol total hydroxyl groups) were dispersed in 200 mL DMF using an ultrasonication treatment at 0 °C for 0.5 h. Then, 15.1 mL dry pyridine and 29.7 mL degassed methacrylic anhydride (6 eq. to CNCs) were added. The suspension was heated to 60 °C and stirred for further 18 h under argon. After the reaction has completed, the suspension was centrifuged and the modified CNCs were subsequently washed three times with a toluene/ethanol/acetone mixture (4/1/1 by vol.). Further purification was achieved with a Soxhlet extraction with acetone for 24 h.

3.6.3 Synthesis of CNC-BAPO

The remaining acetone in the purified **CNC-MMA** was exchanged for ethanol by three centrifugations and redispersion operations. After the last centrifugation step, the **CNC-MMA** suspension in ethanol was introduced in a 500 mL Schlenk flask and 250 mL of ethanol was added. The suspension was degassed with argon for 30 min, then 10.2 g HP(COMes)₂ (1 eq. to the glucose chain units of CNC) and 0.43 mL triethylamine (0.1 eq) were added. The mixture was allowed to stir for 2 days at 60 °C under argon. The flask was covered with aluminum foil in order to prevent decomposition of the product. Subsequently, 4.7 mL of aqueous H₂O₂ (1.5 eq., 35%) was added dropwise to the suspension at 0 °C. The mixture was allowed to slowly warm to r.t. and stirred vigorously for 12 h. Then, the suspension was centrifuged and the modified nanocrystals were purified by Soxhlet extraction for 1 day. After drying in a vacuum oven at 45°C for 2 days, a yellow powder was obtained and stored in a desiccator over P₂O₅.

3.6.4 Polymerization of acrylic monomers

Typically, 0.25 g **CNC-BAPO** were introduced into a quartz tube with a stirring bar and the reaction vessel degassed. In a separate flask, a solution of 25 mmol acrylate monomer in 10 mL DMF was prepared and degassed by three freeze-pump-thaw cycles. This solution was injected into the quartz tube. A yellow suspension was obtained after stirring for 30 min at 0 °C. Subsequently, the sample was irradiated with UV light for 1 hour under vigorous stirring at room temperature.

The yellow suspension turned white after the irradiation and was precipitated into 100 mL cold ethanol. The solid substance was collected by filtration and washed with cold ethanol to remove residual monomer. For 2-hydroxyethyl acrylate and *N*-Isopropylacrylamide, diethyl ether was used instead of ethanol. This precipitate was then purified by Soxhlet extraction with acetone for 1 day to separate the homopolymer from the grafted copolymer, except for **CNC-g-PHEA**, which was treated with methanol instead. The homopolymer was obtained by removing the solvent and dried together with the grafted CNC in a vacuum oven at 65 °C until constant masses were obtained.

3.6.5 Gravimetric calculations

The weights of grafted CNC and retrieved homopolymers were used to calculate graft yield(G), and graft efficiency(G_E) in each product with the following formulae (1)-(2):

$$\text{Graft yield} = G = \frac{m_G}{m_{Cell}} \times 100\% \quad (1)$$

$$\text{Graft efficiency} = G_E = \frac{m_G}{m_G + m_P} \times 100\% \quad (2)$$

where m_G is the mass of the grafted polymer; m_P is the mass of the homopolymer; m_{Cell} is the mass of the cellulose nanocrystals.

3.6.6 Isolation of grafted polymer

Cellulose backbone was hydrolyzed by methods adapted from the literature.^{23,27}

For **CNC-g-PMMA** and **CNC-g-PBuA**, 200 mg of grafted CNC were mixed in a flask with 10 mL of acetone and 15 mL of THF. After addition of 1 mL of concentrated sulfuric acid (98%), the mixture was refluxed for 12 hours. The resulting brown slurry was poured into cold ethanol and the precipitated polymer was washed with ethanol, dissolved in acetone, filtered, and precipitated again in cold ethanol.

For **CNC-g-PNIPAAm**, 200 mg were placed in 30 mL of 2% NaOH solution for 48 h under stirring. Following the saponification, the dispersion was brought to neutral pH with 6 N HCl and then centrifuged (12'000 rpm at 10 °C for 20 min) to separate the CNC from the cleaved polymer in the supernatant. The supernatant was then dialyzed against DI water until a minimum in conductivity was reached.

Cleaved and purified polymers were dried for further analysis.

3.6.7 Preparation of PMMA composites

Cellulose nanocrystals were first dispersed in toluene by stirring at room temperature for 14 h. The desired amount of PMMA (4% in toluene) was added and the resulting suspension was homogenized by using a Ultra-Turrax at 15'000 rpm for 3 min. Solid films were obtained by casting the suspension on Teflon plates and evaporation of toluene at room temperature. To remove any traces of solvent, the films were heated at 50 °C for 24 h and subsequently stored in a desiccator that contained silica gel until they were analyzed. The thickness of composite films was around 0.1 mm.

3.6.8 TEM Characterization

TEM samples were measured by using a JEOL 2200FS instrument (JEOL, USA) at an accelerating voltage of 200 kV. 5 μ L of untreated nanocrystal suspension in water (0.01 wt%) or of the BAPOs modified nanocrystal in ethanol, were deposited on holey carbon-coated copper grid (200 mesh), negatively stained with uranyl acetate and allowed to dry before measurement.

3.6.9 X-ray Diffraction Analysis

X-ray diffraction (XRD) measurements of all samples were performed using a Bruker D8 Advanced diffractometer (Cu K α radiation: $\lambda = 1.54184$ Å; tube parameters: V = 40 kV, I = 40 mA) with a parallel incident beam prepared by a Göbel Xray mirror. The patterns were recorded with a 1D position sensitive detector (VÅNTEC). The powder samples were measured using a flat sample holder in reflection mode. The scans were recorded in the 2θ range 5-40°.

3.6.10 Crystallinity Index (CI)

The crystallinity index (CI) was evaluated using the Buschle-Diller and Zeronian equation:²⁸

$$CI = 1 - \frac{I_{am}}{I_{200}}$$

where I_{200} is the intensity of the 200 lattice plane at $2\theta = 22.4^\circ$ and I_{am} represents the peak intensity at 18° , which corresponds to the amorphous material in cellulose.

3.6.11 Thermogravimetric Analysis (TGA)

TGA analyses were conducted by using a TGA7 apparatus (PerkinElmer, USA). The dried samples (~5 mg) were heated from 30 to 800 °C at a constant rate of 20 °C/min under a He atmosphere.

3.6.12 Differential Scanning Calorimetry (DSC)

DSC analyses were conducted by using a DSC7 apparatus (PerkinElmer, USA). The dried samples (~5 mg) were measured by a heat-cool-reheated method at a constant rate of 20 °C/min under a He atmosphere.

3.6.13 Tensile tests

PMMA composite films were cut into dog-bone-shaped specimens with a length of 50 mm, a width of 8.5 mm at the clamping zone, and a width of 4 mm at the stretching zone. The modulus of elasticity (E), nominal tensile strength (σ), and elongation at break of the composites were analyzed by using a Universal Testing System Z010 (Zwick, Germany) with a loading cell of 200 N and a deformation rate of 2 mm/min. Measurements were performed in a conditioned room (50% RH and 23°C), and the results were the average of five measurements.

3.7 References

1. Habibi, Y.; Lucia, L. A.; Rojas, O. J. *Chem. Rev.*, 2010, **110**, 3479-3500.
2. Klemm, D.; Kramer, F.; Moritz, S.; Lindström, T.; Ankerfors, M.; Gray, D.; Dorris, A. *Angew. Chem. Int. Ed.*, 2011, **50**, 5438-5466.
3. Eichhorn, S. J. *Soft Matter*, 2011, **7**, 303-315.
4. Dufresne, A. *Materialstoday*, 2013, **16**, 220-227.
5. Moon, R. J.; Martini, A.; Nairn, J.; Simonsen, J.; Youngblood, J. *Chem. Soc. Rev.*, 2011, **40**, 3941-3994.
6. Tingaut, P.; Zimmermann, T.; Sèbe, G. *J. Mater. Chem.*, 2012, **22**, 20105-20111.
7. Giese, M.; Blusch, L. K.; Khan, M. K.; MacLachlan, M. J. *Angew. Chem. Int. Ed.*, 2015, **54**, 2888-2910.
8. Domingues, R. M. A.; Gomes, M. E.; Reis, R. L. *Biomacromolecules*, 2014, **15**, 2327-2346.
9. Lagerwall, J. P F; Schütz, C.; Salajkova, M.; Noh, J. H.; Park, J. H.; Scalia, G.; Bergström, L. *NPG Asia Mater.*, 2014, **6**, e80.
10. Kaushik, M.; Basu, K.; Benoit, C.; Cirtiu, C. M.; Vali, H.; Moores, A. *J. Am. Chem. Soc.*, 2015, **137**, 6124-6127.

11. Yang, X.; Cranston, E. D. *Chem. Mater.*, 2014, **26**, 6016-6025.
12. Eyleya, S.; Thielemans, W. *Nanoscale*, 2014, **6**, 7764-7779.
13. Habibi, Y. *Chem. Soc. Rev.*, 2014, **43**, 1519-1542.
14. Roy, D.; Semsarilar, M.; Guthrie, J. T.; Perrier, S. *Chem. Soc. Rev.*, 2009, **38**, 2046-2064.
15. (a) L. H. C. Mattoso, E. S. Medeiros, D. A. Baker, J. Avloni, D. F. Wood and W. J. Orts, *J. Nanosci. Nanotechnol.*, 2009, **9**, 2917; (b) C. Zhou, Q. Wu, Y. Yue
16. and Q. Zhang, *J. Colloid Interface Sci.*, 2011, **353**, 116; (c) J. Tang, M. F. X. Lee, W. Zhang, B. Zhao, R. M. Berry and K. C. Tam, *Biomacromolecules*, 2014, **15**, 3052.
17. (a) K. Littunen, U. Hippi, L.-S. Johansson, M. Österberg, T. Tammelin, J. Laine and J. Seppälä, *Carbohydr. Polym.*, 2011, **84**, 1039; (b) P. Stenstad, M. Andresen, B. R. Tanem and P. Stenius, *Cellulose*, 2008, **15**, 35.
18. (a) S. Margutti, S. Vicini, N. Proietti, D. Capitani, G. Conio, E. Pedemonte and A. L. Segre, *Polymer*, 2002, **43**, 6183; (b) L. C. V. Wielen and A. J. Ragauskas, *Eur. Polym. J.*, 2004, **40**, 477; (c) V. Kumar, Y. K. Bhardwaj, S. N. Jamdar, N. K. Goel and S. Sabharwal, *J. Appl. Polym. Sci.*, 2006, **102**, 5512.
19. (a) A. Carlmark and E. Malmström, *J. Am. Chem. Soc.*, 2002, **124**, 900; (b) D. Nyström, J. Lindqvist, E. Östmark, A. Hult and E. Malmström, *Chem. Commun.*, 2006, **34**, 3594; (c) Q. Xu, J. Yi, X. Zhang and H. Zhang, *Eur. Polym. J.*, 2008, **44**, 2830.
20. (a) S. Perrier, P. Takolpuckdee, J. Westwood and D. M. Lewis, *Macromolecules*, 2004, **37**, 2709; (b) D. Roy, J. T. Guthrie and S. Perrier, *Macromolecules*, 2005, **38**, 10363; (c) A. Hufendiek, V. Trouillet, M. Meier and C. Barner-Kowollik, *Biomacromolecules*, 2014, **15**, 2563.
21. (a) Y. Habibi, A.-L. Goffin, N. Schiltz, E. Duquesne, P. Dubois and A. Dufresne, *J. Mater. Chem.*, 2008, **18**, 5002; (b) G. Chen, A. Dufresne, J. Huang and P. R. Chang, *Macromol. Mater. Eng.*, 2009, **294**, 59; (c) N. Lin, G. Chen, J. Huang, A. Dufresne and P. R. Chang, *J. Appl. Polym. Sci.*, 2009, **113**, 3417; (d) M. Labet and W. Thielemans, *Polym. Chem.*, 2012, **3**, 679.
22. Z. Zhang, P. Tingaut, D. Rentsch, T. Zimmermann and G. Sèbe, *ChemSusChem*, 2015, **8**, 2681.
23. (a) M. Griesser, D. Neshchadin, K. Dietliker, N. Moszner, R. Liska and G. Gescheidt, *Angew. Chem. Int. Ed.*, 2009, **48**, 9359; (b) U. Kolczak, G. Rist, K. Dietliker and J. Wirz, *J. Am. Chem. Soc.*, 1996, **118**, 6477; (c) S. Jockusch and N. J. Turro, *J. Am. Chem. Soc.*, 1998, **120**, 11773.
24. J. O. Zoppe, Y. Habibi, O. J. Rojas, R. A. Venditti, L.-S. Johansson, K. Efimenko, M. Osterberg and J. Laine, *Biomacromolecules*, 2010, **11**, 2683.
25. J. Alongi, R. A. Carletto, F. Bosco, F. Carosio, A. Di Blasio, F. Cuttica, V. Antonucci, M. Giordano and G. Malucelli, *Polym. Degrad. Stab.*, 2014, **99**, 111.
26. M. Labet and W. Thielemans, *Cellulose*, 2011, **18**, 607.

27. P. Tingaut, T. Zimmermann and F. L. Suevos, *Biomacromolecules*, 2010, **11**, 454.
28. K. Littunen, U. Hippi, L.-S. Johansson, M. Österberg, T. Tammelin, J. Laine and J. Seppälä, *Carbohydr. Polym.*, 2011, **84**, 1039.
29. G. Buschle-Diller and S. H. Zeronian, *J. Appl. Polym. Sci.*, 1992, **45**, 967.

4 All-in-One cellulose nanocrystals for 3D printing of nanocomposite hydrogels

4.1 Introduction

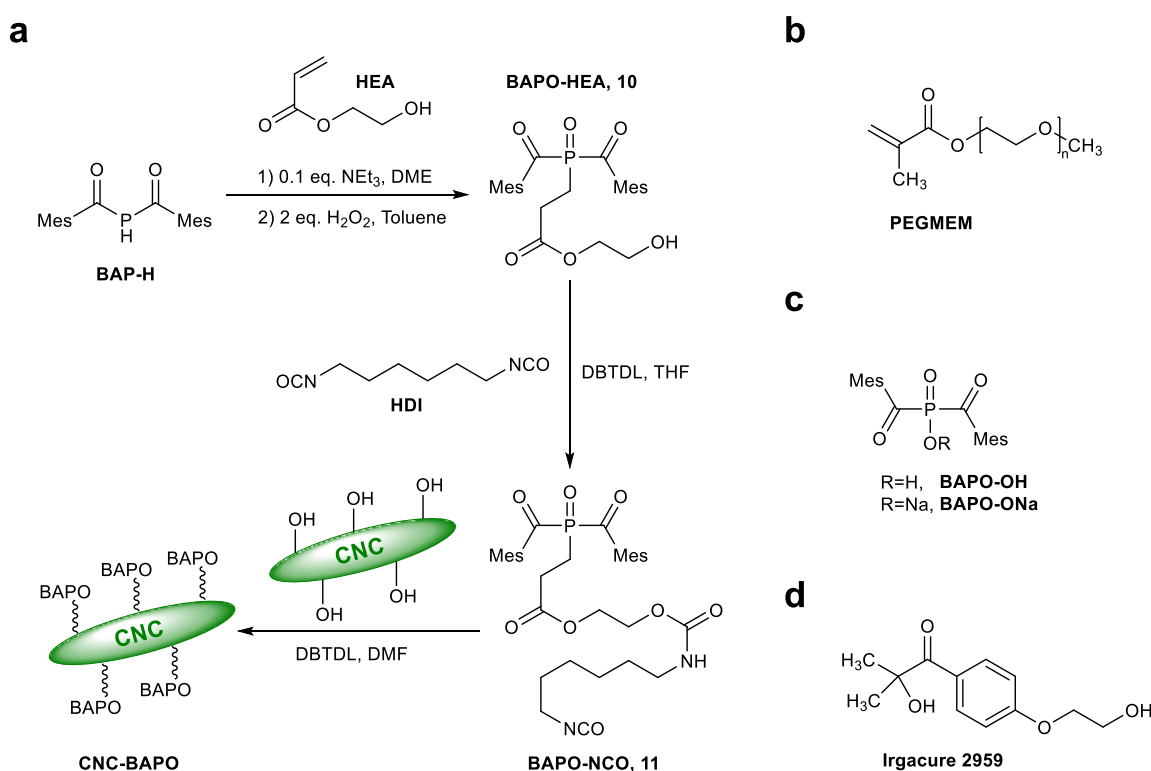
Cellulose nanocrystals (CNCs)¹ possess remarkable physicochemical properties and are promising reinforcing components² for nanocomposite hydrogels.³ Nanocellulose-based nanocomposite hydrogels can be fabricated using 3D printing.⁴ However, conventional cross-linkers are often added which result in mechanically weak and brittle hydrogels.⁵

Photoinitiators (PIs) play a critical role in determining the polymerization rate and the properties of the printed objects.⁶ The mostly used commercially available PI (Irgacure 2959, Scheme 4.1d) is poorly water-soluble and little efficient in the ultraviolet-visible range.⁷

In chapter 3, we succeeded to attach BAPO functions onto CNCs for polymer grafting. This approach consisted in modifying the surfaces of CNCs with methacrylate functions in a first step to which bis(acyl)phosphane oxide functions could be added in a second step. This procedure proves to be rather tedious on larger scale also because a special synthetic protocol needs to be worked out for every cellulosic or related support material. In this chapter, we introduce a new strategy where we use a suitably functionalized BAPO derivative that can be directly used to bind covalently to CNCs without any further modification of their surfaces. That is the surface bound hydroxyl groups are directly addressed. Subsequently, a mono-functional monomer was successfully grafted from the obtained photoactive nanomaterial without introducing any additional crosslinking between individual polymer chains, resulting in a stable network structure which is otherwise impossible to achieve with conventional photoinitiators. Using this water dispersible nanomaterial, 3D structured objects were

fabricated under mild conditions with a digital light processing (DLP) 3D printer, which is equipped with energy-efficient UV-LEDs (405 nm). The obtained nanocomposite hydrogels show enhanced mechanical properties, outstanding swellability and good shape stability.

4.2 Synthesis of BAPO derivatives and functionalization of cellulose nanocrystals



Scheme 4.1 The photoinitiators and the mono-functional monomer. (a) Synthesis of BAPO derivatives and functionalization of cellulose nanocrystals. (b) Chemical structure of the mono-functional methacrylate PEGMEM, $M_n = 950$ g/mol. (c) Chemical structure of BAPO-OH and BAPO-ONa. (d) Chemical structure of Irgacure 2959.

2-Hydroxyethyl 3-(bis(2,4,6-trimethylbenzoyl)phosphoryl)propanoate (**10**, BAPO-HEA) was first synthesized via phospho-Michael addition of BAP-H (**1**) onto 2-hydroxyethyl acrylate (HEA), followed by oxidation with aqueous H_2O_2 . Adding a THF solution of BAPO-HEA dropwise to an excess of the commercially available hexamethylene diisocyanate (HDI, 3 eq.)

in the presence of 1.3 mol% dibutyltin dilaurate (DBTDL) as promotor results in 2-([6-isocyanatohexyl]carbamoylethyl 3-(bis(2,4,6-trimethylbenzoyl) phosphoryl)propanoate (**11**, BAPO-NCO) as a yellow solid in 93% yield (Scheme 4.1a). Under these conditions, the double addition of BAPO-HEA to both of the isocyanate groups is suppressed.

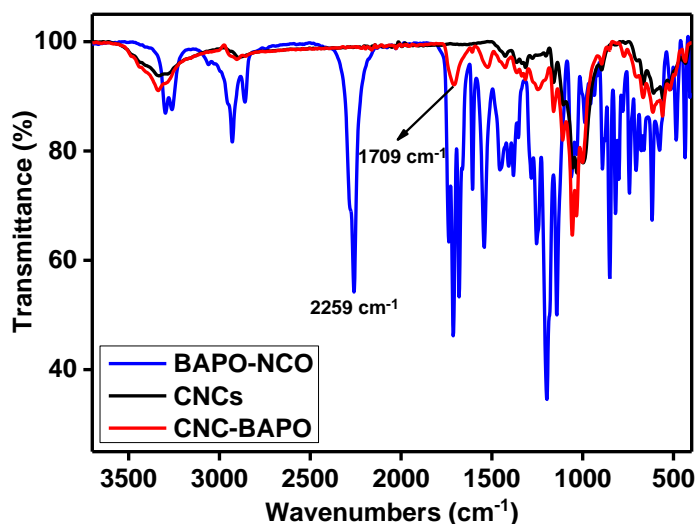


Figure 4.1 FTIR-ATR spectra of BAPO-NCO, neat CNCs and CNC-BAPO.

In the FTIR-ATR spectrum of BAPO-NCO, the strong absorbance of the isocyanate group at 2259 cm^{-1} is clearly observed (Figure 4.1). The two BAPO derivatives, BAPO-HEA and BAPO-NCO, show similar UV-Vis absorption spectra with a maximum absorbance at 290 nm assigned to the $\pi \rightarrow \pi^*_{\text{CO}}$ band of the BAPO chromophore. As is commonly observed for BAPO derivatives, the $n \rightarrow \pi^*_{\text{CO}}$ excitation is observed as weaker band in the range between 360 to 440 nm (Figure 4.2).

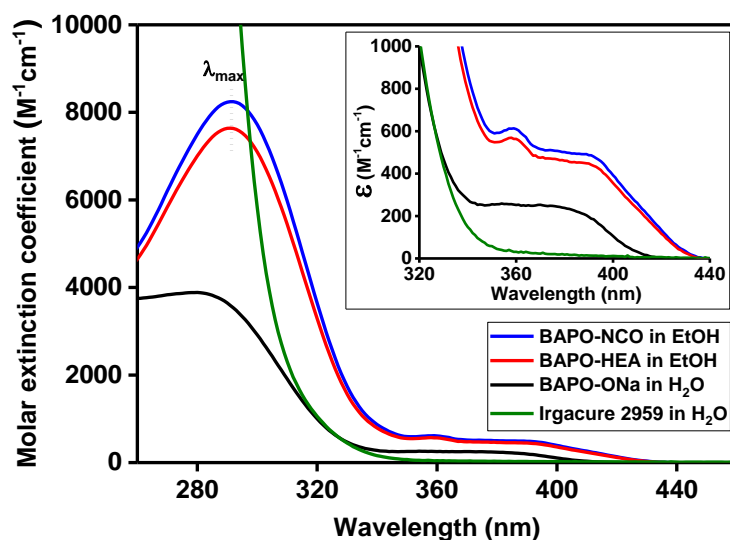


Figure 4.2 UV-Vis absorption spectra of BAPO-HEA, BAPO-NCO, BAPO-ONa and Irgacure 2959 in different solvents recorded at the same concentrations (0.1 mM).

CNC-BAPO was prepared by reacting the surface hydroxyl groups of cellulose nanocrystals with BAPO-NCO in DMF again using 4 mol% DBTDL as promotor. Unreacted BAPO-NCO was removed with acetone as solvent in a Soxhlet extractor. The obtained nanomaterial was dispersed in water and kept in the dark for later use. Elemental analysis of dry CNC-BAPO indicates a phosphorus content of 0.94%. This suggests that about 2'100 BAPO units are bound to one single cellulose nanocrystal. The corresponding surface density of BAPO units can be estimated to be $7.0 \times 10^{-8} \text{ g/cm}^2$ (see subsection 4.6.3 for details).

The successful immobilization was confirmed by various spectroscopic techniques. In the UV-Vis spectrum (Figure 4.3), the wavelength of maximum absorbance (λ_{max} , $\pi \rightarrow \pi^*_{\text{CO}}$) is blue shifted compared to a physical blend of BAPO-NCO and neat CNCs ($\lambda_{\text{max}} = 290 \text{ nm}$) by 21 nm to 269 nm. The excitation wavelength of $n \rightarrow \pi^*_{\text{CO}}$ transition shows no observable change (Figure 4.4). We assume that the blue shift may be caused by hydrogen bonds between the BAPO units and the polar cellulose nanocrystals surfaces. This is supported by an experiment

in which BAPO-OH (chemical structure see Scheme 4.1c) was mixed with NH_4Cl which also leads to a blue shift of the $\pi \rightarrow \pi^*_{\text{CO}}$ transition while the $n \rightarrow \pi^*_{\text{CO}}$ band remains unaffected (Figure 4.5). A suspension of neat CNCs shows negligible absorptions in the relevant range from 220 nm to 460 nm.

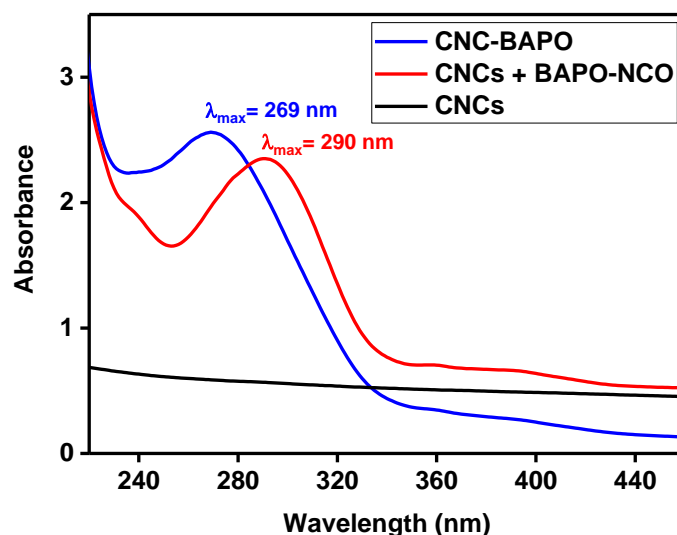


Figure 4.3 UV-Vis absorption spectra of neat CNCs (288 $\mu\text{g}/\text{mL}$), a blend of BAPO-NCO and CNCs (containing 72 μg of BAPO-NCO and 288 μg of neat CNCs per mL), and CNC-BAPO (360 $\mu\text{g}/\text{mL}$) in ethanol. The amounts of CNCs and BAPO-NCO were calculated based on the phosphorus content determined by elemental analysis of the CNC-BAPO sample.

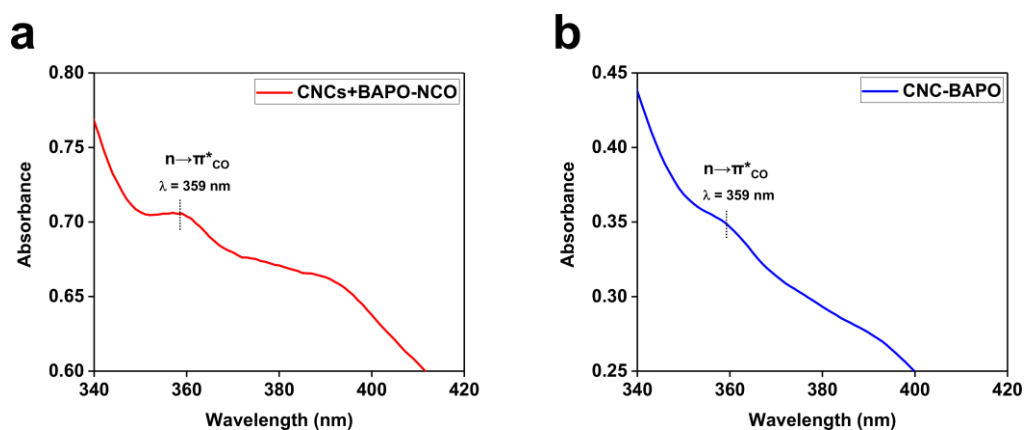


Figure 4.4 UV-Vis absorption spectra in the selected range from 340 nm to 420 nm. For an extended view of the UV-Vis spectra see figure 2b in the main text. (a) The physical blend of BAPO-NCO and CNCs. (b) CNC-BAPO.

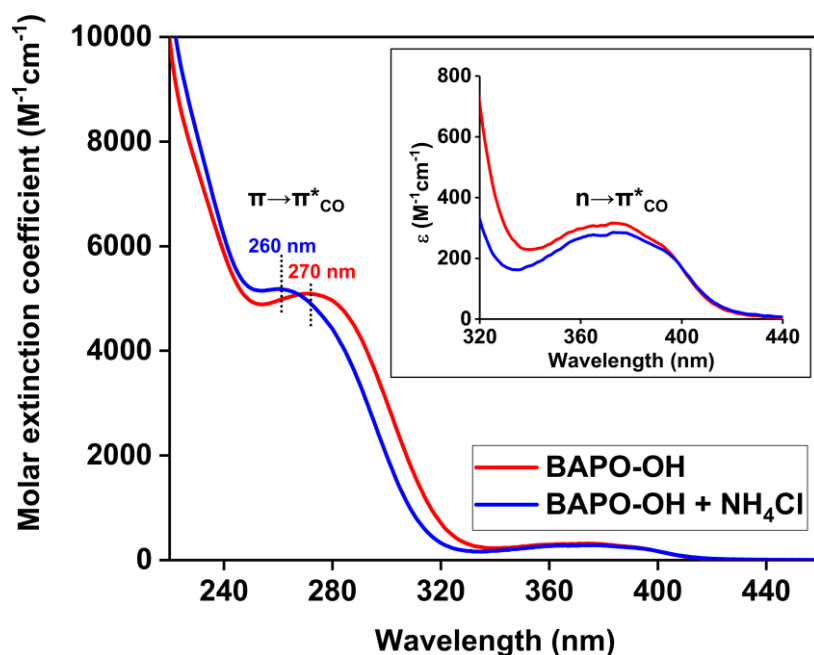


Figure 4.5 UV-Vis absorption spectra of BAPO-OH mixed with (blue line) and without NH_4Cl (red line) in ethanol recorded at a concentration of 0.1 mM. The $\pi \rightarrow \pi^*_{\text{CO}}$ transition is blue shifted while the $n \rightarrow \pi^*_{\text{CO}}$ band shows no visible shift.

The FTIR-ATR spectrum of CNC-BAPO (Figure 4.1) shows the typical stretching vibration of the carbonyl group ($\nu_{\text{C=O}}$) at 1709 cm^{-1} , corresponding to the urethane linkage which is absent in the spectrum of unmodified CNCs. Furthermore, the absence of the absorbance of the isocyanate groups at 2259 cm^{-1} suggests that the unreacted BAPO-NCO was completely removed during purification.

The single signal at 24.1 ppm in the ^{31}P CP-MAS NMR spectrum of CNC-BAPO (Figure 4.6, inset) is similar to the resonance of BAPO-NCO (24.9 ppm). In the ^{13}C CP-MAS NMR spectrum, the characteristic signals of the BAPO units at $\delta = 216.9$ (COMes), 172.5 (COCH₂), 156.7 (CONH), 140.2 (C⁴ Mes), 135.9 (C^{2,6} Mes), 129.1 (C^{3,5} Mes), 41.2 and 27.7 (CH₂ chains of HDI), and 20.1 ppm (*o*, *p*-CH₃ Mes) are clearly identifiable.

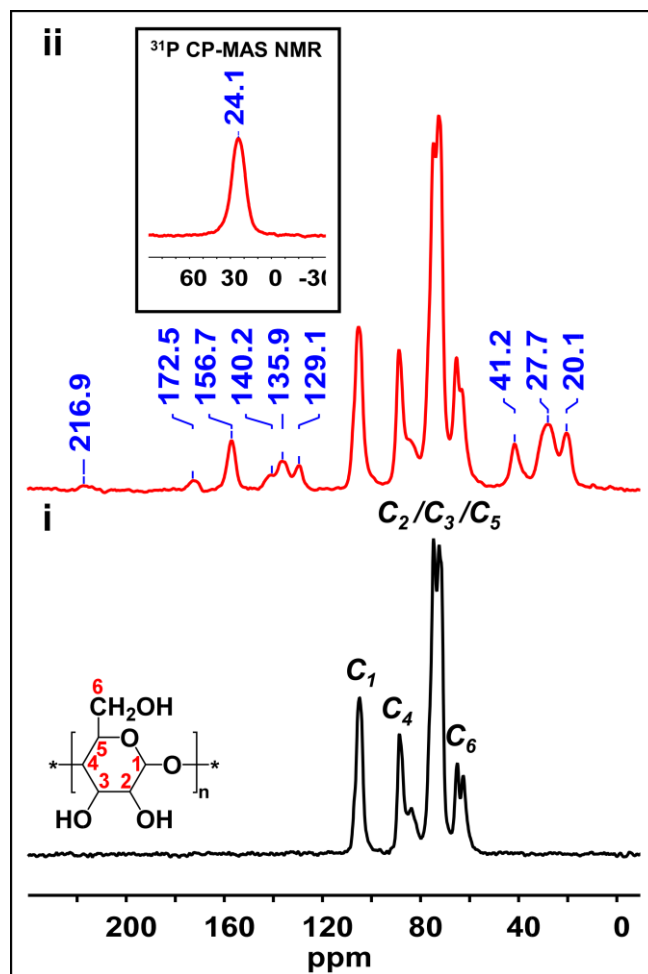


Figure 4.6 ^{13}C CP-MAS NMR spectrum of unmodified CNCs (i), ^{13}C and ^{31}P CP-MAS NMR spectra of CNC-BAPO (ii). Typical ^{13}C signals of cellulose nanocrystals at $\delta = 105.0$ (C₁), 88.6 (C₄ crystalline), 83.8 (C₄ amorphous), 74.7/72.4 (C_{2,3,5}), 65.0 (C₆ crystalline), and 62.9 ppm (C₆ amorphous) are observed in both spectra.

AFM confirms that the morphology of the CNCs is maintained and only a slight aggregation occurs during the treatment with BAPO units (Figure 4.7), since the introduced hydrophobic BAPO units can decrease the dispersity of cellulose nanocrystals in water.

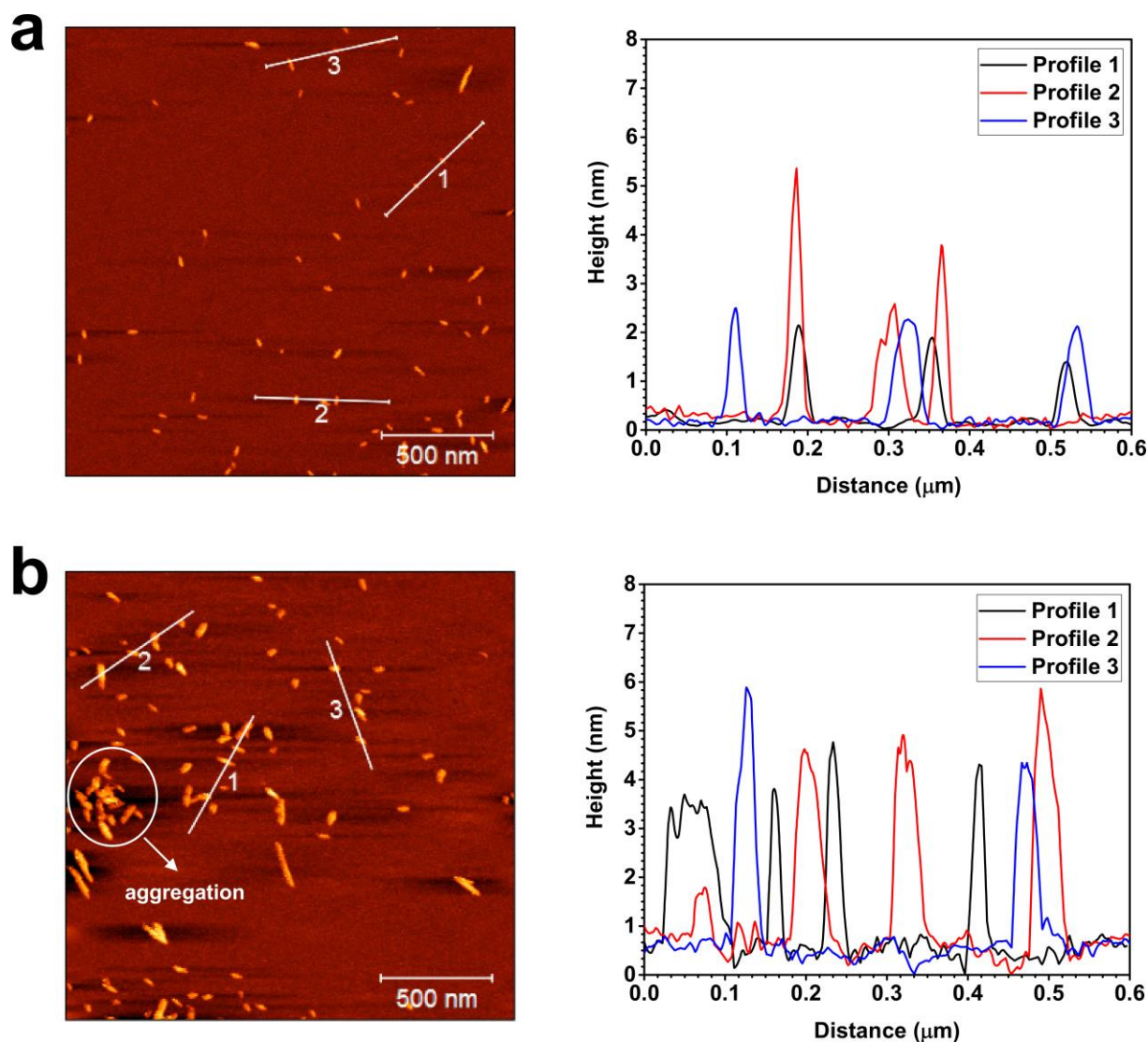


Figure 4.7 Tapping mode AFM $2 \times 2 \mu\text{m}$ height image of unmodified CNCs (a) and CNC-BAPO (b). The height of BAPO functionalized CNCs are similar to the unmodified CNCs. Please notice that AFM heights are almost half as large as TEM widths (an average diameter of 5–10 nm and lengths of 100–150 nm, data from the University of Maine), which might be due to counting of a larger fraction of laterally associated CNCs in the TEM images.⁸

The neat CNCs and CNC-BAPO show similar crystallinity and exhibit typical cellulose I β crystalline patterns,⁹ suggesting that the modification is limited to the surfaces of CNCs (Figure 4.8).

Upon combustion, CNC-BAPO shows a considerably higher char yield (19.1% at 800 °C, see Figure 4.9). This is because organo phosphorus compounds grafted on a cellulose substrate

favor char formation and suppress the concentration of combustible volatile species during thermal decomposition.¹⁰

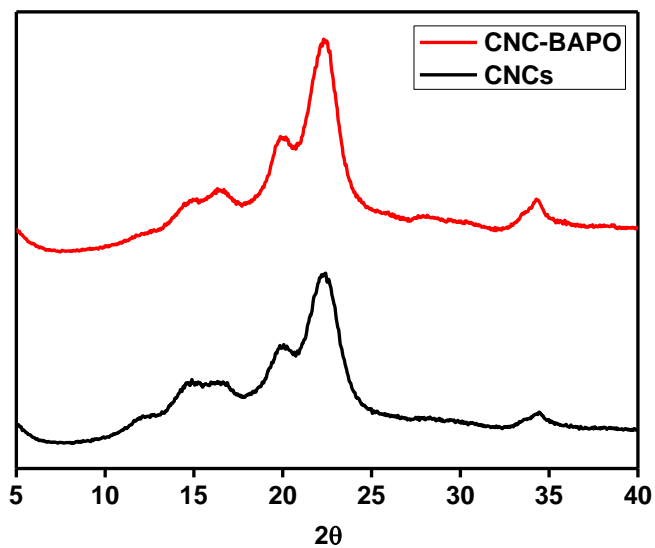


Figure 4.8 X-ray diffraction patterns of unmodified CNCs and CNC-BAPO.

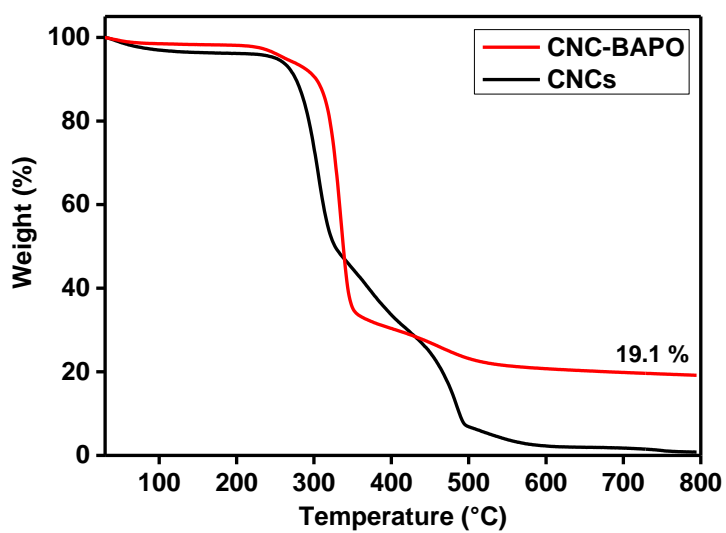


Figure 4.9 TGA thermograms of unmodified CNCs and CNC-BAPO.

4.3 Photopolymerization studies of different aqueous formulations

CNC-BAPO was tested for the polymerization of the mono-functional monomer: poly(ethylene glycol) methyl ether methacrylate (PEGMEM, $M_n = 950$ Da, chemical structure see Scheme 4.1b) in 50 wt% aqueous solutions. The influence of different amounts of CNC-BAPO was investigated. A recently reported water soluble photoinitiator BAPO-ONa¹¹ (chemical structure see Scheme 4.1c), which is more efficient than the widely used commercially available Irgacure 2959¹² (UV-Vis absorption spectra of these two PIs see Figure 4.2), was used with or without neat CNCs for comparison (Table 4.1).

Table 4.1 Composition of formulations and the properties of obtained thin films.

Formulation	PEGMEM ^[a]	BAPO-ONa ^[a]	Neat CNCs ^[a]	CNC-BAPO ^[a] ₁	tan(δ) ^[c]	Gel content (%)	DSC		Young's modulus (MPa)	Crosslinking density (mmol/cm ³) ^[d]	Swelling (%)
							T_m (°C)	ΔH (J/g)			
I	49.58	0.42	/		0.75	16	55	-96	130 ± 38	/	/
II	47.06	0.40	2.54		0.46	22	49	-94	272 ± 20	/	/
III	46.73	/	/	3.27 ^[b]	0.22	82	48	-85	270 ± 10	0.006	1100±65
IV	43.86	/	/	6.14	0.20	80	47	-79	340 ± 25	0.028	740±40

[a] wt%. [b] reactive species equal to **II**. [c] calculated based on the final plateau of the curves. [d] calculated according to the statistical theory of rubber elasticity.

Photorheology was applied to investigate the photopolymerization kinetics of the formulations. The measurements show the evolution of shear storage modulus (G') and loss modulus (G'') during irradiation with visible light (15 mW/cm²) and a cut-off filter at 400 nm under constant oscillation frequency (Figure 4.10). In all cases, the polymerization reaction shows a delay after switching on the light, probably because of oxygen inhibition. Formulations containing CNC-BAPO (Table 4.1, **III** and **IV**) show faster kinetics and reach higher G' values than the formulations using BAPO-ONa as PI (Table 4.1, **I** and **II**). With the doubled amount of CNC-BAPO (**IV**), the polymerization starts earlier than with half of that concentration (**III**).

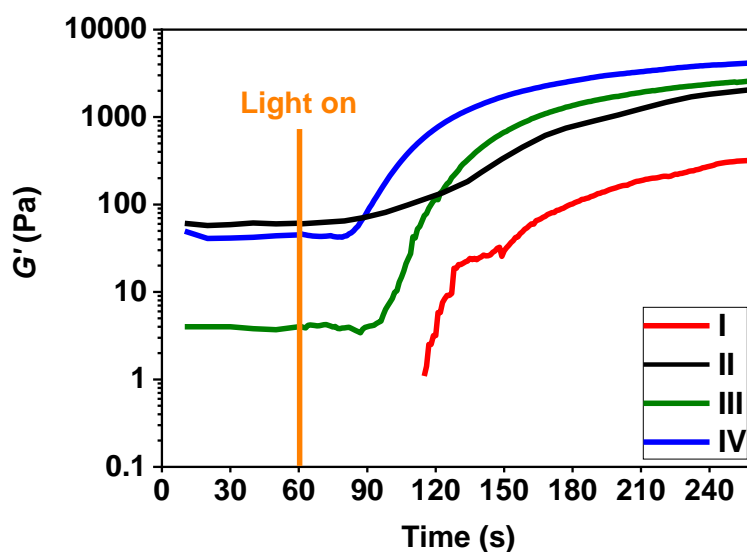


Figure 4.10 Photorheology characterization of the photopolymerization kinetics.

In addition, the gelation time of **III** (less than 1 min) is twice as short compared to **I** (Figure 4.11). **II** shows slower kinetics but a higher initial G' value was observed before the onset of the gelation process. This phenomenon indicates strong physical interactions between cellulose nanocrystals and polyethylene glycol chains. **I** shows a low elastic response at the beginning beyond the sensitivity limit of the instrument. It also reaches the lowest G' value of all samples. Furthermore, the introduction of CNC-BAPO leads to lower damping factors in $\tan(\delta)$ (Table 4.1).

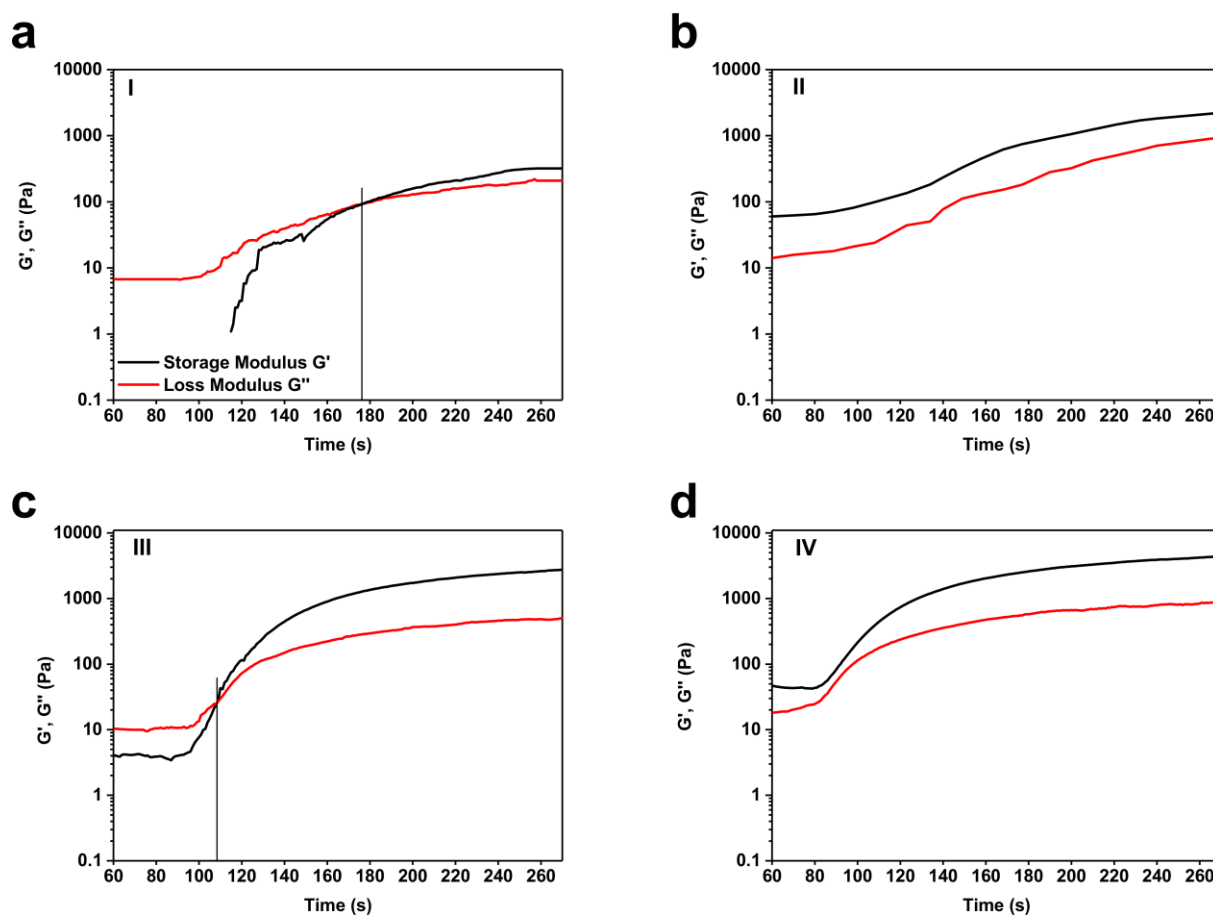


Figure 4.11 Time dependence of storage modulus G' and loss modulus G'' for formulations: (a) formulation **I**; (b) formulation **II**; (c) formulation **III**; (d) formulation **IV**. The light was switched on 60 seconds after the recording of data started. The data shown here are obtained after this delay. For samples **I** and **III**, G' is lower than G'' before irradiation, as it is common for liquid formulations. In these two graphs, the gel points were observed and it is evident that with the use of CNC-BAPO, the gel point,¹³ which is generally defined as the time required for G' to surpass G'' , is reached in a shorter time. For samples **II** and **IV**, the physical interactions among cellulose nanocrystals and the monomers in water are high and these formulations gave already “gelly” materials ($G' > G''$) before irradiation. Therefore, a gel point could not be observed.

Frequency sweep measurements (Figure 4.12) show that **III** and **IV** present higher G' elastic moduli (5.5 and 6 kPa, respectively) than **I** and **II** (2.5 and 3.6 kPa, respectively), indicating a higher mechanical stability of samples containing CNC-BAPO.

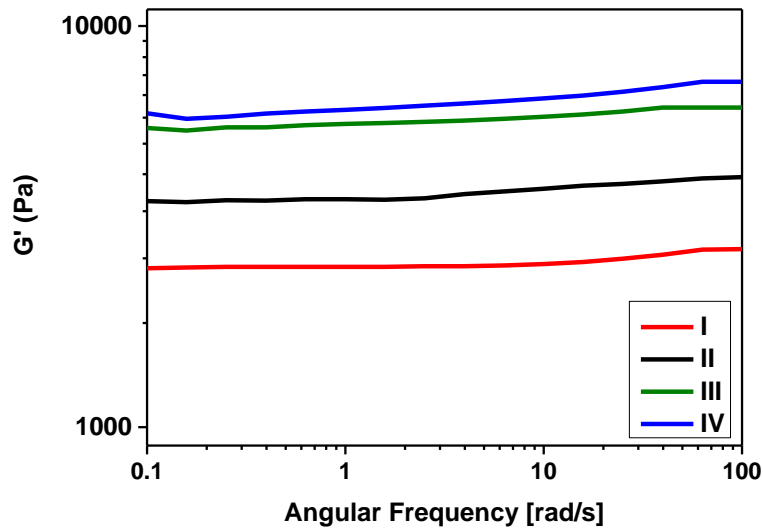


Figure 4.12 Frequency sweep measurements performed on specimens irradiated in the photorheometer.

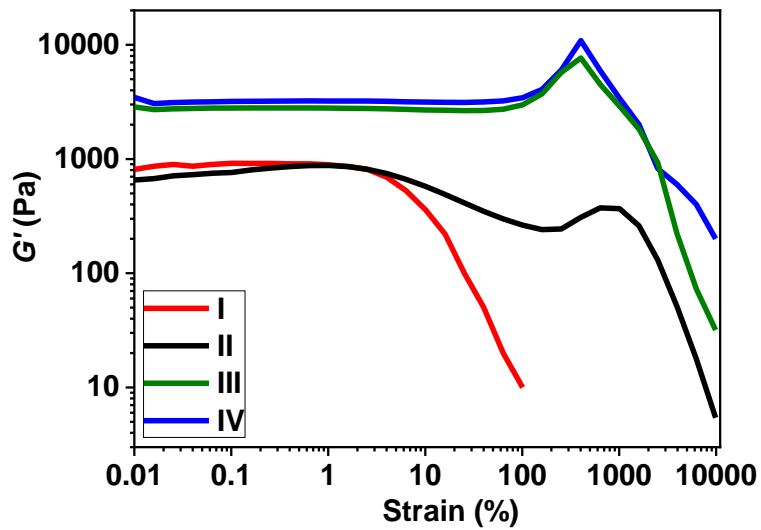


Figure 4.13 Amplitude sweep test performed on the cured samples.

Amplitude sweep measurements reveal a strong difference in the behavior under increasing oscillating amplitude (Figure 4.13). **III** and **IV** can stand a strain amplitude up to 100% and their structure breaks with a brittle fracture for larger deformations, due to a stronger network.

I and **II** have a reduced linear viscoelastic region with smoother drops, indicating a more easily flowing material.

With BAPO-ONa as PI and a mono-functional monomer, linear thermoplastic polymer chains are expected (Figure 4.14a). In contrast, CNC-BAPO contains thousands of photoactive BAPO groups on the surface which act as initiating centers for polymerization and as crosslinking points at the same time. Consequently, covalently cross-linked networks are obtained (Figure 4.14b).

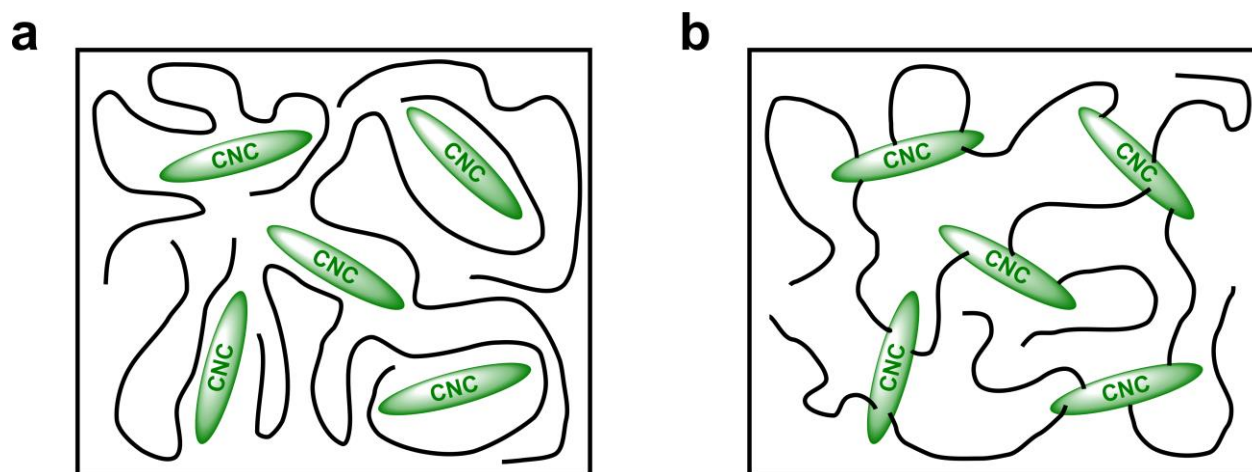


Figure 4.14 Schematic representation of polymerization in the presence of unmodified CNCs (**a**) and in the presence of CNC-BAPO (**b**). Polymer chains bound to cellulose nanocrystals with both chain ends are generated by recombination of radical chain ends, while dangling polymer chains bound to cellulose nanocrystals are obtained by disproportionation.

To confirm this, thin films (0.5 mm thick) were prepared and placed in deionized water for 1 day before ultrasonication (35 kHz) for half an hour. As expected, **I** and **II** disintegrated during sonication, while **III** and **IV** remained intact, suggesting robust and covalently cross-linked networks had been generated (Figure 4.15).

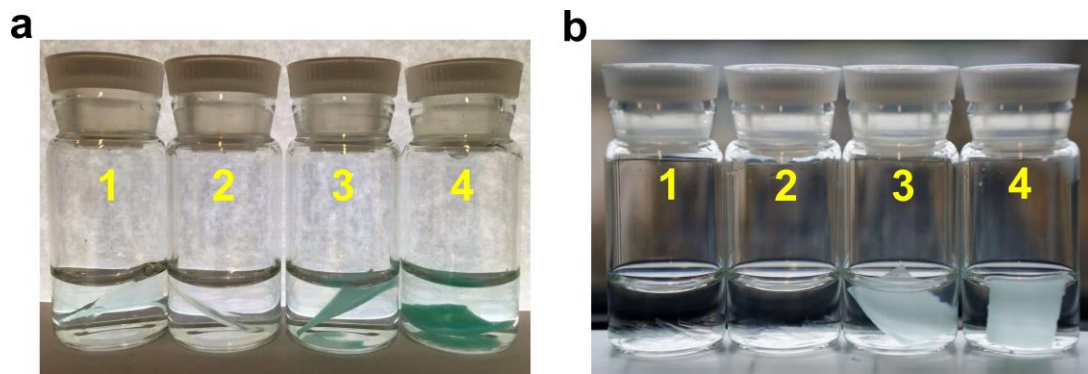


Figure 4.15 Photographs of casted films obtained from formulations according to Table 4.1 after placing them in deionized water for 5 min (a) and after immersion in water for 24 h followed by 30 min sonication (b).

This is also in agreement with another experiment in which the soluble and insoluble parts of the polymeric materials were separated by extraction with water. The evaluation of the insoluble fraction is listed in Table 4.1. High gel content values ($\geq 80\%$) were obtained with **III** and **IV** in contrast to **I** and **II** (gel content $\leq 22\%$). The soluble segments in **III** and **IV** are supposed to be the homopolymers generated by free mesityl radicals which form during the photolysis $\text{CNC-PO(R)(COMes)} + h\nu \rightarrow [\text{CNC-PO(R)}]^\bullet + \text{MesCO}^\bullet$ (R = COMes or polymer chain)¹⁴, schematic representation of the polymerization process see Figure 4.16.

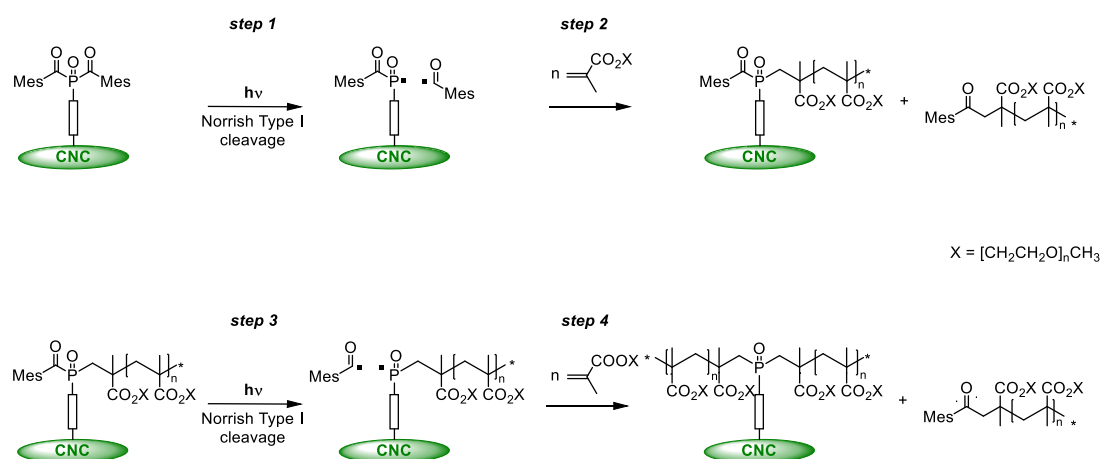


Figure 4.16 Detailed schematic representation of the polymerization process initiated by surface bound bis(acetyl)phosphane oxides.

In each of the reaction steps (1) and (3), a phosphorus centered radical is formed, which is chemically linked to the CNCs surfaces. Both radicals which are generated in two subsequent photoinitiated cleavage reactions, efficiently initiate the polymerization of acrylic double bonds, resulting in two polymer chains growing from the surface-fixed phosphorus atom (reaction steps (2) and (4)). In the same photoinduced cleavage reactions (1) and (3), two mesitoyl radicals are concomitantly formed, which are not linked to the substrate. Although mesitoyl radicals are known to be less efficient in the initiation of acrylate polymerization than the phosphinoyl radicals, this inevitably leads to the formation of nonbound homopolymers as shown in both reaction steps (2) and (4). These linear photopolymers can, however, easily be removed from the grafted CNCs surfaces by careful washing with water.

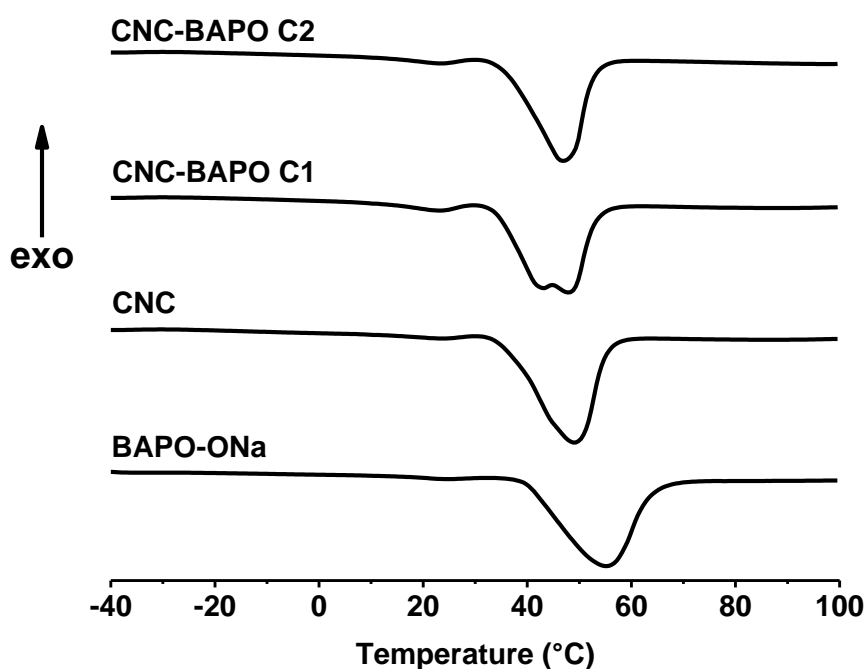


Figure 4.17 DSC thermograms of the thin films obtained. A second melting peak appears at lower temperature in BAPO-CNC C1 sample. This can be attributed to different thickness of crystals owing to the varying number of folds in the polymer chain.¹⁵

DSC measurements indicate that the presence of CNCs, both neat and functionalized, reduces the melting temperature (T_m) of the polymer. Due to cross-linking, **III** and **IV** show reduced crystallinity indicated by decreased endothermic peak areas (Figure 4.17).¹⁶

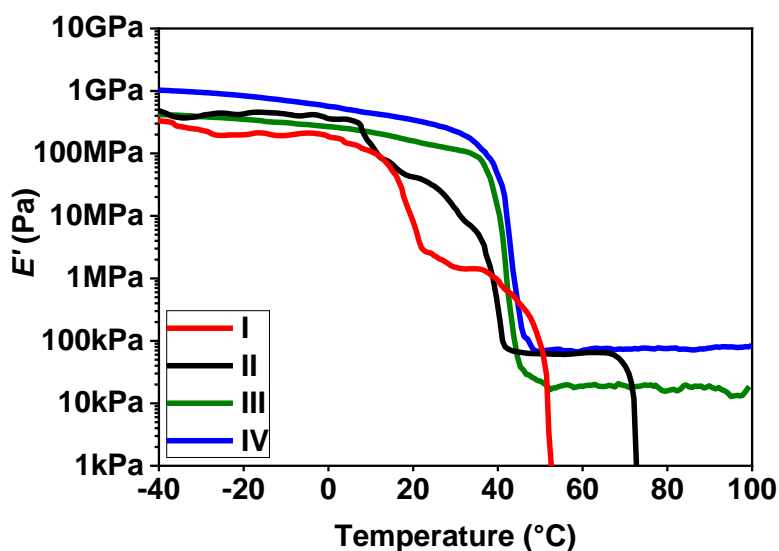


Figure 4.18 E' curves obtained from DMA measurements for thin films.

Dynamic mechanical analyses (DMA) (Figure 4.18) give additional support for the effective cross-linking of the polymer matrices. **III** and **IV** show rubbery plateaus at temperatures above T_m that remain stable until high temperatures (100 °C). The specimen with no CNCs chemically linked to the polymer matrices show a viscoelastic flux over T_m . These indicate that thermoset polymers were generated using CNC-BAPO as cross-linkers. The crosslinking density of the networks increases as expected with a higher amount of CNC-BAPO (Table 4.1). Tensile elongation tests of the dried specimen confirm that the presence of CNCs increases the Young's moduli of the polymer matrices (Table 4.1).

Extraordinary swelling ratios were achieved with **III** and **IV** when they are immersed in water (Table 4.1 and Figure 4.20a). The values are one order of magnitude greater than those

of other PEG-based hydrogels.¹⁷ Since a mono-functional monomer was used, the generated flexible polymer chains have sufficient mobility for large expansion due to the absence of extra crosslinking points. They can undergo extensive swelling similar to free and linear polymer chains.¹⁸ **IV** shows decreased swelling ratio and slower swelling kinetics (Figure 4.19), owing to the increased crosslinking density.

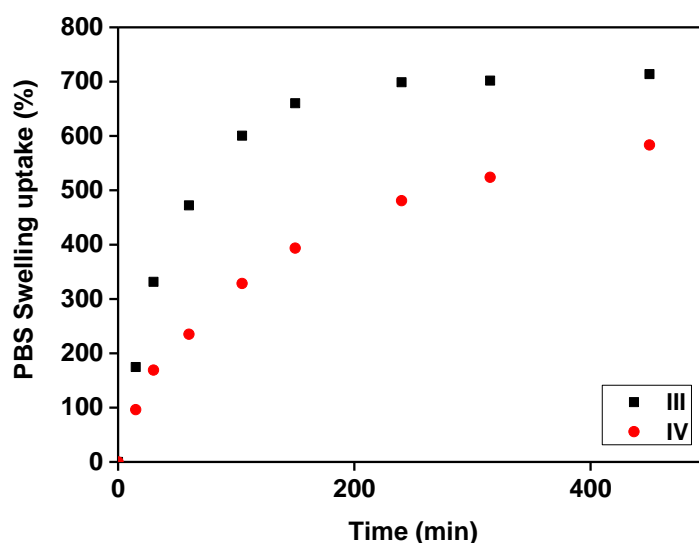


Figure 4.19 Swelling kinetics of the dried printed samples at room temperature in PBS.

4.4 3D printing of nanocomposite hydrogels

Formulations **III** and **IV** were used in a DLP 3D printer with LEDs (405 nm) for 3D printing. In spite of the high swellability, shape-persistent, free-standing 3D structured objects can be printed. No conventional cross-linkers are used in this process. Flat specimen were printed (4 mm thick) and probed by tensile tests in dried and swollen form (Figure 4.20a). The values obtained for the dried samples were close to those obtained for the specimen prepared previously by casting, indicating that 3D printing does not affect the mechanical properties. A

good conservation of the mechanical stability is maintained after swelling, which is comparable with other PEG-based hydrogels containing significantly less amount of water.¹⁹ In both dried and swollen form, **IV** shows a higher modulus, confirming a more cross-linked network (Figure 4.21).

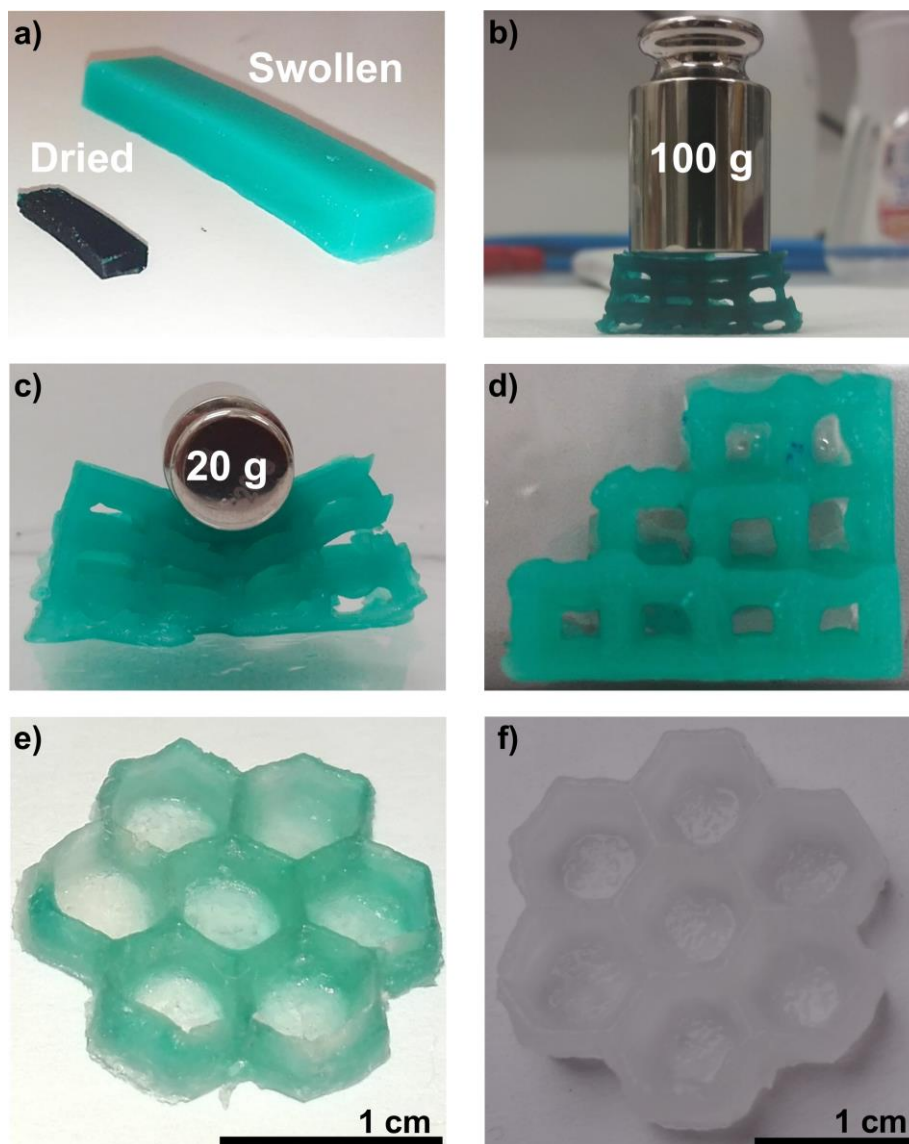
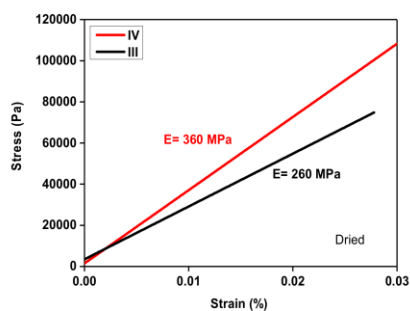


Figure 4.20 (a) Flat specimen from **III**. (b) A dried cubic-lattice structure from **III**. (c) The same structure after swelling for 1h. (d) The maintained structure after removing the 20 g weight. (e) A hexagonal structure from **IV**. (f) The swollen structure after repeating three times the drying and swelling procedure. The green dye, which was used to adjust the optical density during 3D printing, was washed out by re-dissolving in water.

(a)



(b)

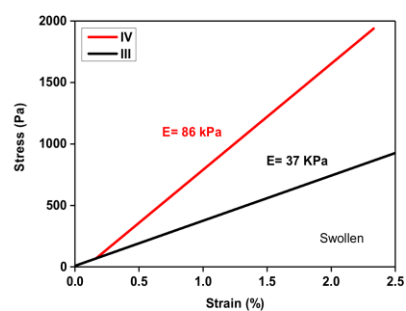


Figure 4.21 Tensile tests performed on the 3D printed samples: dried (a) and swollen (b).

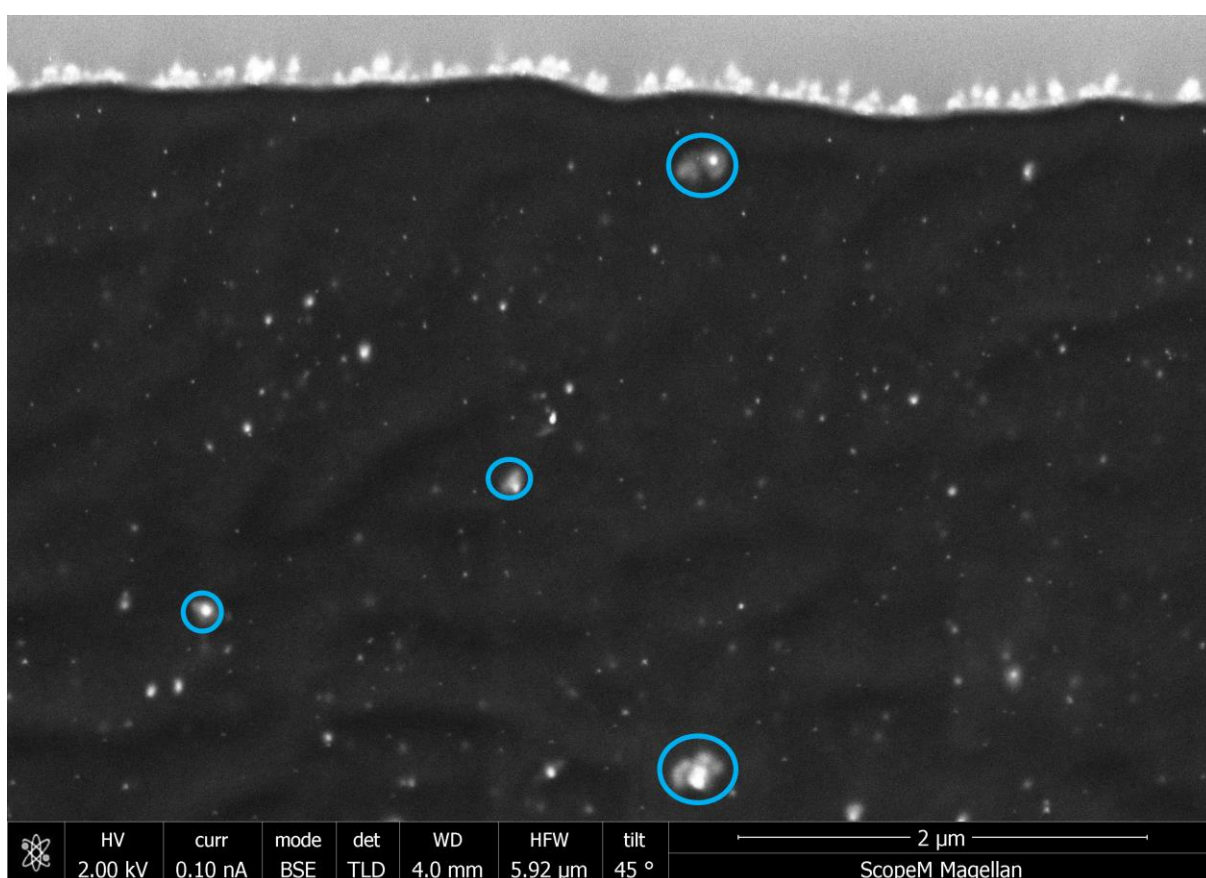


Figure 4.22 SEM images of a 3D printed thin film with the formulation **IV**. Small white dots, which have been previously reported,²⁰ indicate the cross-sections of individual cellulose nanocrystals distributed in the nanocomposite hydrogels. Blue circles suggest aggregates are formed.

A printed cubic-lattice structure can bear a load of 100 g (Figure 4.20b) or 20 g (Figure 4.20c) in dried and swollen form, respectively, without breaking. Furthermore, the drying and swelling

process is fully reversible and the samples of various shapes can be dried and swollen several times without any measurable influence on their integrity (Figure 4.20e-f). A scanning electron microscopy (SEM) investigation of a fractured surface of a 3D printed thin film shows that CNCs are well distributed in the nanocomposite, but aggregation is also observed (Figure 4.22).

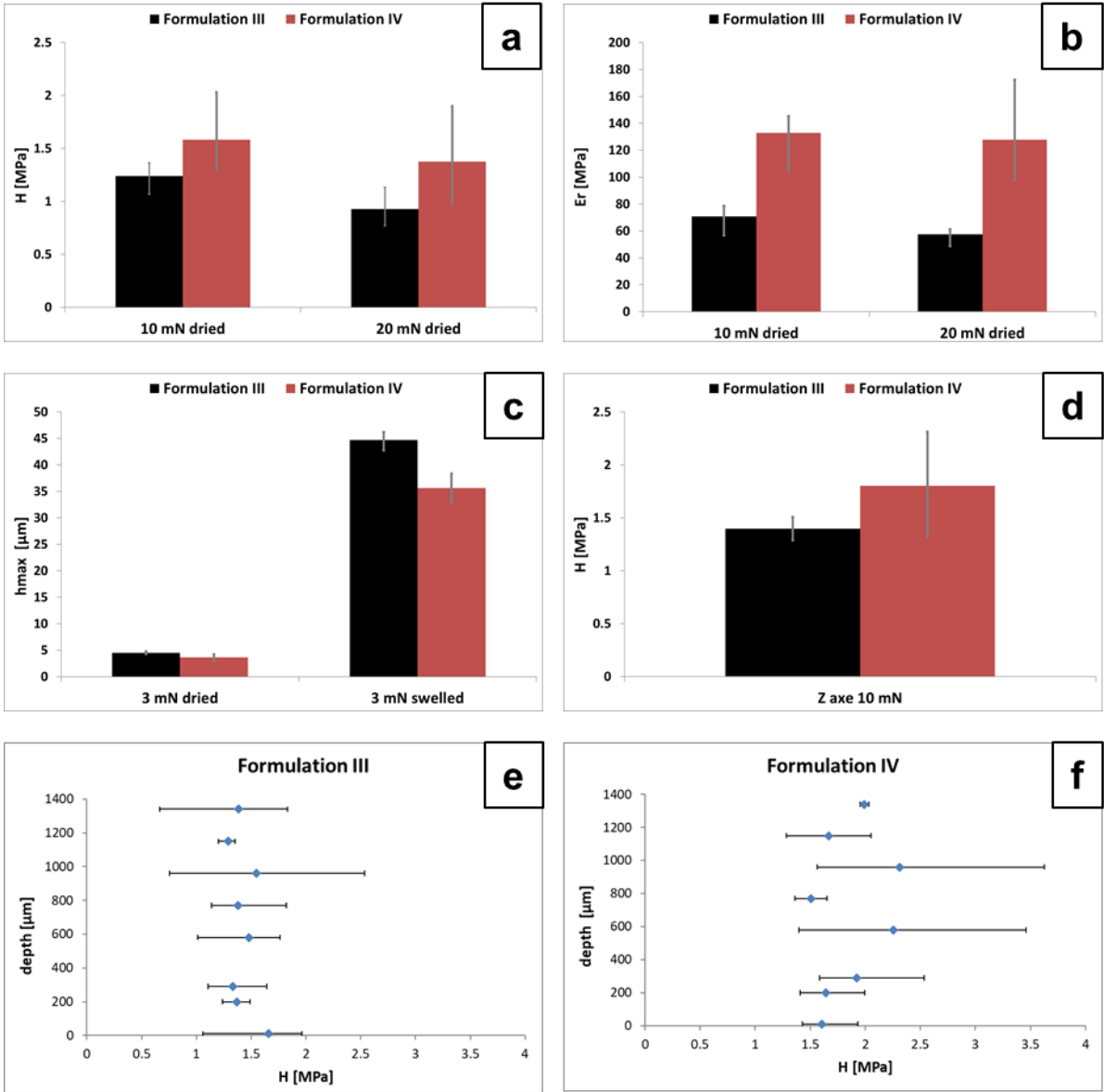


Figure 4.23 Hardness (a) and reduced elastic modulus (b) values of dried samples of formulation III and IV; maximum depth values of dried and swelled samples of III and IV (c); hardness values on Z axis planes of samples of III and IV (d); hardness values along Z axis at different depth on III (e) and IV (f).

Nanoindentation tests were performed on the printed hydrogels. Because of the higher crosslinking density, **IV** shows higher nanohardness, reduced elastic modulus and resistance to penetration than **III** in both dried and swollen form (Figure 4.23a-d). The nanohardness in the Z axis plane along the depth is homogeneous for both samples (Figure 4.23e-f), indicating the mechanical properties along the layer thickness were maintained during printing.

4.5 Conclusion

In this chapter, a highly photoactive BAPO derivative is described which is covalently bound to cellulose nanocrystals surfaces. When irradiated in the presence of a mono-functional monomer, the BAPO functionalized nanocrystals initiate the grafting of multiple polymer chains from the nanocrystal surfaces, which results in a stable three-dimensional polymer network with the cellulose nanocrystals acting as covalently embedded nanofillers and crosslinking points. The generated flexible polymer chains provide extraordinary swelling properties of the obtained nanocomposites. 3D structured nanocomposite hydrogels are successfully printed using these multifunctional nanocrystals with a commercially available DLP 3D printer equipped with UV-LED light sources. The printed structures are mechanically stable, easy to handle and show a superior swelling capacity. The approach of modifying the surfaces of nanofillers with photoinitiating groups, as presented here, has the potential to become a reliable strategy for the functionalization of a variety of nanomaterials possessing hydroxyl groups at the surfaces. This can further open an eco-friendly way to the rapid 3D printing of nanocomposite hydrogels including components from renewable resources in aqueous solutions with curing devices which have a low energy consumption.

4.6 Methods

4.6.1 Materials

Cellulose nanocrystals obtained from wood pulp by sulfuric acid treatment were provided by the University of Maine. They were purified by Soxhlet extraction with ethanol for 24 h before modification as described in chapter 3. PEGMEM ($M_n = 950$ g/mol) was purchased from Sigma-Aldrich (Switzerland) and used directly. Brilliant green dye was obtained from Merck (Germany).

4.6.2 Synthesis of CNC-BAPO

In a 250 mL Schlenk flask, 3.0 g (18.5 mmol) neat cellulose nanocrystals were dispersed in 150 mL dry DMF before ultra-sonication (35 kHz) at 0 °C for 30 min. Subsequently, 12.5 g (20 mmol, 1.1 eq.) BAPO-NCO and a catalytic amount of dibutyltin dilaurate (500 μ L) dissolved in 20 mL dry DMF were added. The suspension was heated to 100 °C and stirred for 24 h under argon in the dark. After the reaction was completed, the suspension was centrifuged and the modified cellulose nanocrystals were subsequently washed with acetone in a Soxhlet extractor for 24 h. The purified CNC-BAPO was suspended in H₂O (0.05 g/mL) and stored in the fridge. Elementary analysis [found %]: C, 46.79; H, 6.66; N, 2.53; S, 0.76; P, 0.94. The final weight of dry CNC-BAPO, measured gravimetrically by drying an aliquot of the water suspension, was 3.6 g. The value correlates well with the elementary analysis, which gives 3.7 g.

4.6.3 Estimation of the number of BAPO-NCO units bound on one CNC

The cellulose nanocrystals exhibit an average diameter of 5–10 nm and lengths of 100–150 nm as declared by the material supplier at the University of Maine.

Under the assumption that a nanocrystal has a rod-like form,²¹ the volume V_{CNC} of a single nanocrystal is given by:

$$V_{CNC} = \frac{\pi}{4} d^2 l$$

d = average width of the nanocrystals = 8 nm;

l = average length of the nanocrystals = 125 nm.

Mass, m_{CNC} , of a single nanocrystal:

$$m_{CNC} = V_{CNC} \times \rho$$

ρ = density of the nanocrystals = 1.5 g/cm³ (density of crystalline cellulose²¹).

Numbers, n_{CNC} , of nanocrystals in 1 g CNCs:

$$n_{CNC} = \frac{1}{m_{CNC}}$$

The weight content, m_{BAPO} , of BAPO-NCO grafted onto 1 g of CNC-BAPO is given by:

$$m_{BAPO} = \frac{1 \times E_p}{M_p} \times M_{BAPO}$$

E_p = phosphorus content of the sample = 0.94% as determined by elemental analysis;

M_p = molecular weight of phosphorus = 31 g·mol⁻¹;

M_{BAPO} = molecular weight of the BAPO-NCO = 626.7 g·mol⁻¹.

Number, n_{BAPO} , of BAPO-NCO molecules grafted onto 1 g of CNC-BAPO:

$$n_{BAPO} = \frac{m_{BAPO}}{M_{BAPO}} \times N_A$$

N_A = Avogadro constant = $6.022 \times 10^{23} \text{ mol}^{-1}$

Mass of CNCs in 1 g of CNC-BAPO:

$$m_{CNC-BAPO} = 1 - m_{BAPO}$$

Numbers of CNCs, $n_{CNC-BAPO}$, in 1g of CNC-BAPO:

$$n_{CNC-BAPO} = n_{CNC} \times \frac{m_{CNC-BAPO}}{1}$$

The ratio between BAPO-NCO and CNCs in 1 g of CNC-BAPO:

$$R = \frac{n_{BAPO}}{n_{CNC-BAPO}} = \frac{E_P \times N_A}{M_P} \times \frac{m_{CNC}}{m_{CNC-BAPO}} = \frac{E_P \times N_A}{M_A} \times \frac{V_{CNC} \times \rho}{1 - m_{BAPO}} \approx 2.1 \times 10^3$$

Surface density calculation, ρ_A , of BAPO-NCO units on one single nanocrystal:

$$\rho_A = \frac{m_{BAPO}}{A_{CNC-BAPO}} = \frac{m_{BAPO}}{\frac{4}{\rho \times d} \times m_{CNC-BAPO}} \approx 7.0 \times 10^{-8} \text{ g} / \text{cm}^2$$

4.6.4 Preparation of formulations

A weight of 20 g for each formulation was prepared according to Table 4.1. PEGMEM was dissolved in water first, followed by adding photoinitiators and cellulose nanocrystals. Suspensions containing cellulose nanocrystals were homogenized using an Ultra-turrax stirrer (IKA, T10) for 10 min in the dark. The homogenized suspension was degassed at a reduced pressure.

4.6.5 Photopolymerization kinetics and rheological characterizations

Rheological measurements in real time were performed using an Anton Paar rheometer (Physica MCR 302) in parallel plate mode. For photorheology tests the light source used was a Hamamatsu LC8 lamp with a bulb emitting visible light (15 mW/cm^2) and a cutoff filter below 400 nm equipped with a 7 mm light guide. The set-up has a lower plate in quartz, the gap between the two plates was set to 0.1 mm and the sample was kept at a constant temperature ($25 \text{ }^\circ\text{C}$). Under a constant shear frequency of 60 rad/sec, light was turned on after 1 min in order to stabilize the system. Concomitant changes in viscoelastic material moduli (G' and G'') during illumination were measured as a function of exposure time. The measurements were carried out in the linear viscoelastic region (strain amplitude 0.1%).

For the frequency and amplitude sweep tests the formulation were placed on the quartz plate, the gap was set at 0.1mm and the material was cured for 4 minutes. Frequency sweep tests were performed over a frequency range of 0.1-100 rad/sec and with a constant strain amplitude of 1%. Amplitude sweep tests were performed over a strain range of 0.1-10000% at a constant frequency of 10 rad/sec.

4.6.6 Preparation of thin films

Thin films (0.5 mm thick) were prepared by casting the formulations in a plastic mold and irradiating 2 min with visible light (Hamamatsu LC8, 25 mW/cm^2) under nitrogen atmosphere. All samples were dried for 2 days in vacuum at room temperature before removing from the mold.

4.6.7 Dynamic mechanical analysis and tensile test

Thin films were cut into rectangle-shaped specimens with a length of 30 mm, a width of 5 mm. The measurements were performed with a Triton Technology TTDMA in tensile configuration. All experiments were performed with a temperature ramp of 3 °C/min, applying a force with a frequency of 1 Hz and with 10 µm of displacement. The same equipment was used for performing tensile tests on printed samples (30 mm length, 5 mm width, 4 mm thick) in controlled-force mode (force increase 0.5 N/min). 4 specimens were tested for each composition to give the average Young's modulus (E) values. The mechanical experiments were carried out at 25 °C both on dried samples and on samples after 5h of swelling in water.

4.6.8 Calculation of Crosslinking density

The crosslinking density is calculated from the measured storage modulus (E') values above T_m , according to the statistical theory of rubber elasticity.²² The number of moles of crosslinking points per unit volume, i.e. the crosslinking density for a network can be obtained from the equation: $E' = \nu RT$, where ν is the crosslinking density, R is the universal gas constant, and T is the temperature.

4.6.9 3D printing of model structures

Three-dimensional hydrogels were printed by UV-curing the formulations containing CNC-BAPO (**III** and **IV**). Brilliant green dye (0.05 wt% of the monomer) was used to limit the light penetration. The predesigned digital models were 3D printed using a Freeform Pico Plus 39 DLP printer (Asiga) with XY pixel resolutions of 39 microns using a UV-LED light source (405nm, 22 mW/cm²). The layer thickness was settled at 20 µm and the layer exposition time varied from 3 to 6 seconds according to the design. After printing, the structures were rinsed

with water in a sonicator for 3 min to remove residual non-cured materials. A subsequent post curing process was performed with a medium pressure mercury lamp for 5 min (provided by Robot Factory).

4.6.10 Nanoindentation tests

Hardness (H) and reduced elastic modulus (E_r) were performed using the NanoIndenter Ti950 (Hysitron) with a higher load head (3D OmniProbe) designed to accommodate a wide range of applications. The tests were performed by applying and removing controlled loads to the specimens using a geometrically well-defined probe.²³ A cono-spherical probe was used. Conical-spherical probe is a conical shaped probe with a spherical end (with a radius of 5 μm). Three different loads (3 mN, 10mN and 20 mN) are used to test the dried samples on the XY axis plane. The swollen samples were tested only with a load of 3 mN. Because if higher loads are used, the depth is over of instrument limits. The dried samples are also tested in Z surface with a load of 10 mN. To test the homogeneity of hardness along the depth, the indentation on Z axis plane were realized at the distance of 190 μm . The loads were applied with a rate of 0.25 mN/s with a permanence time at the maximum load of 5 s. The swollen samples were valued in terms of maximum depth (h_{max}), because the depth is extremely high in relation to the load and the hardness value is not reliable. It is clear that the samples with a maximum depth have the highest resistance to penetration.

4.6.11 Swelling kinetics

The swelling kinetics of the gels in PBS was measured gravimetrically at room temperature. The vacuum dried samples were immersed in PBS. At different time intervals, the hydrogels were removed from the solution and the weight was determined after wiping off the liquid on the surfaces with wet filter papers. The swelling ratio (SR) is defined as follows $\text{SR} = 100 \times$

$(W_t - W_d)/W_d$, where the W_t is the weight of the hydrogel at a certain time and W_d is the weight of the dried hydrogel.

4.6.12 Atomic-force microscopy (AFM)

The AFM measurements were performed on a commercial AFM system (BioScope Catalyst, Bruker Nano, Santa Barbara, California) that is mounted onto an inverted confocal laser-scanning microscope (FluoView FV500, Olympus, Center Valley, Pennsylvania). 10 μ L of diluted aqueous suspension (0.001 wt%) of each sample was deposited onto freshly cleaved mica and left to dry at room temperature. The height images were obtained using tapping mode AFM with ATEC NC cantilever probes (Nanosensors, Neuchatel, Switzerland). The images are 2 x 2 μ m in size, with a resolution of 512 x 512 pixels, and a scan rate of 0.5 Hz was used.

4.6.13 Differential scanning calorimetry (DSC)

DSC analyses were performed using a Netzsch DSC 204 F1 Phoenix instrument, equipped with a low temperature probe. The experiments were carried out between -50 and 100 $^{\circ}$ C with a scan rate of 10 $^{\circ}$ C min⁻¹.

4.6.14 Gel content determination

The insoluble fraction (gel content) of the products was determined according to the following procedure: the samples were held in a metal net, weighted and subsequently submitted to extraction for 24 hours at room temperature in water to dissolve the non-cross-linked polymers. Then the samples were dried for 2 days in vacuum at room temperature. The insoluble fraction percentage was determined as weight difference before and after solvent extraction.

4.6.15 Determination of swelling ratio

The thin films were immersed in deionized water for 24 h at room temperature. Then, the samples were removed from the water and blotted dry to gently remove excess water. The swollen sample mass was recorded. Afterwards, the hydrogels were dried for 2 days in vacuum at room temperature and then the dry mass was recorded. 3 specimens were tested for each composition. The swelling percentage of the cross-linked samples was calculated as:

$$\text{Swelling}(\%) = \frac{W_s - W_d}{W_d} \times 100;$$

W_d = Weight of dry sample, W_s = Weight of swollen sample.

4.6.16 Focused Ion Beam Scanning Electron Microscopes (FIB-SEM)

The samples were mounted with conductive Silver paint on aluminium SEM-stubs and were sputter coated with 2 nm Iridium while rotating. Perpendicular cross section milling was performed in a FEI Helios 600i FIB-SEM with a Gallium ion beam at 30 kV and 2.5 nA. Polishing was done at 30 kV and 790 pA. The polished cross section was imaged with an electron beam at 2 kV and 0.17 nA by detecting backscatter and secondary electrons (through-the-lens detector in different detection modes: TLD BSE, TLD SE).

4.7 References

1. a) Y. Habibi, L. A. Lucia, O. J. Rojas, *Chem. Rev.* **2010**, *110*, 3479-3500; b) K. J. De France, T. Hoare, E. D. Cranston, *Chem. Mater.* **2017**, *29*, 4609-4631.
2. a) J. Yang, C.-R. Han, J.-F. Duan, M.-G. Ma, X.-M. Zhang, F. Xu, R.-C. Sun, X.-M. Xie, *J. Mater. Chem.* **2012**, *22*, 22467-22480; b) X. Yang, E. Bakaic, T. Hoare, E. D. Cranston, *Biomacromolecules* **2013**, *14*, 4447-4455; c) J. R. McKee, S. Hietala, J. Seitsonen, J. Laine, E. Kontturi, O. Ikkala, *ACS Macro Lett.* **2014**, *3*, 266-270.

3. a) K. Haraguchi, *Polym J* **2011**, *43*, 223-241; b) A. K. Gaharwar, N. A. Peppas, A. Khademhosseini, *Biotechnol. Bioeng.* **2014**, *111*, 441-453.
4. a) A. Sydney Gladman, E. A. Matsumoto, R. G. Nuzzo, L. Mahadevan, J. A. Lewis, *Nat. Mater.* **2016**, *15*, 413-418; b) J. G. Torres-Rendon, T. Femmer, L. De Laporte, T. Tigges, K. Rahimi, F. Gremse, S. Zafarnia, W. Lederle, S. Ifuku, M. Wessling, J. G. Hardy, A. Walther, *Adv. Mater.* **2015**, *27*, 2989-2995; c) K. Markstedt, A. Mantas, I. Tournier, H. Martínez Ávila, D. Hägg, P. Gatenholm, *Biomacromolecules* **2015**, *16*, 1489-1496; d) G. Siqueira, D. Kokkinis, R. Libanori, M. K. Hausmann, A. S. Gladman, A. Neels, P. Tingaut, T. Zimmermann, J. A. Lewis, A. R. Studart, *Adv. Funct. Mater.* **2017**, *27*, 1604619. e) N. B. Palaganas, J. D. Mangadlao, A. C. C. de Leon, J. O. Palaganas, K. D. Pangilinan, Y. J. Lee, R. C. Advincula, *ACS Appl. Mater. Interfaces* **2017**, *9*, 34314-34324.
5. a) K. Haraguchi, T. Takehisa, *Adv. Mater.* **2002**, *14*, 1120-1124; b) K. Haraguchi, H.-J. Li, *Angew. Chem. Int. Ed.* **2005**, *44*, 6500-6504; c) K. Haraguchi, H.-J. Li, K. Matsuda, T. Takehisa, E. Elliott, *Macromolecules* **2005**, *38*, 3482-3490.
6. a) A. A. Pawar, G. Saada, I. Cooperstein, L. Larush, J. A. Jackman, S. R. Tabaei, N.-J. Cho, S. Magdassi, *Sci. Adv.* **2016**, *2*; b) T. Billiet, M. Vandenhoute, J. Schelfhout, S. Van Vlierberghe, P. Dubruel, *Biomaterials* **2012**, *33*, 6020-6041.
7. B. D. Fairbanks, M. P. Schwartz, C. N. Bowman, K. S. Anseth, *Biomaterials* **2009**, *30*, 6702-6707.
8. A. Brinkmann, M. Chen, M. Couillard, Z. J. Jakubek, T. Leng, L. J. Johnston, *Langmuir* **2016**, *32*, 6105-6114.
9. Y. Nishiyama, P. Langan, H. Chanzy, *J. Am. Chem. Soc.* **2002**, *124*, 9074-9082.
10. J. Alongi, R. A. Carletto, F. Bosco, F. Carosio, A. Di Blasio, F. Cuttica, V. Antonucci, M. Giordano, G. Malucelli, *Polym. Degrad. Stab.* **2014**, *99*, 111-117.
11. G. Müller, M. Zalibera, G. Gescheidt, A. Rosenthal, G. Santiso-Quinones, K. Dietliker, H. Grützmacher, *Macromol. Rapid Commun.* **2015**, *36*, 553-557.
12. S. Benedikt, J. Wang, M. Markovic, N. Moszner, K. Dietliker, A. Ovsianikov, H. Grützmacher, R. Liska, *J. Polym. Sci. A Polym. Chem.* **2016**, *54*, 473-479.
13. R. Muller, E. Gerard, P. Dugand, P. Rempp, Y. Gnanou, *Macromolecules* **1991**, *24*, 1321-1326.
14. a) J. Wang, G. Siqueira, G. Muller, D. Rentsch, A. Huch, P. Tingaut, J. Levalois-Grutzmacher, H. Grutzmacher, *Chem. Commun.* **2016**, *52*, 2823-2826; b) M. Sangermano, M. Periolatto, M. Castellino, J. Wang, K. Dietliker, J. L. Grützmacher, H. Grützmacher, *ACS Appl. Mater. Interfaces* **2016**, *8*, 19764-19771.
15. Wunderlich, B. "Macromolecular physics", Vol. 2: *Crystal Nucleation, Growth Annealing*, Academic Press, New York, **1976**.

16. H. A. Khonakdar, J. Morshedian, U. Wagenknecht, S. H. Jafari, *Polymer* **2003**, *44*, 4301-4309.
17. a) A. Khoushabi, A. Schmocker, D. P. Pioletti, C. Moser, C. Schizas, J. A. Manson, P. E. Bourban, *Compos. Sci. Technol.* **2015**, *119*, 93-99; b) S. Mishra, F. J. Scarano, P. Calvert, *J. Biomed. Mater. Res. Part A* **2012**, *100A*, 2829-2838.
18. a) K. Haraguchi, T. Takehisa, *Adv. Mater.* **2002**, *14*, 1120-1124; b) K. Haraguchi, H.-J. Li, *Angew. Chem. Int. Ed.* **2005**, *44*, 6500-6504.
19. a) J. S. Temenoff, K. A. Athanasiou, R. G. Lebaron, A. G. Mikos, *J. Biomed. Mater. Res.* **2002**, *59*, 429-437; b) Q. T. Nguyen, Y. Hwang, A. C. Chen, S. Varghese, R. L. Sah, *Biomaterials* **2012**, *33*, 6682-6690.
20. L. Tang, C. Weder, *ACS Applied Materials & Interfaces* **2010**, *2*, 1073-1080.
21. G. Siqueira, J. Bras, A. Dufresne, *Langmuir* **2010**, *26*, 402-411.
22. A. Chiappone, S. Jeremias, R. Bongiovanni, M. Schönhoff, *Journal of Polymer Science Part B: Polymer Physics* **2013**, *51*, 1571-1580.
23. W. C. Oliver, G. M. Pharr, *Journal of Materials Research* **1992**, *7*, 1564-1583.

5 A highly efficient waterborne photoinitiator for visible-light-induced 3D printing of hydrogels

5.1 Introduction

Hydrogels are three-dimensional (3D) networks formed by hydrophilic polymer chains.^{1,2} They possess tunable physical and chemical properties and have been widely used in biomedicine, soft electronics, sensors and actuators.^{3,4} With the expansion from initial prototyping to the fabrication of commercial products, 3D printing finds widespread use for the construction of complex and functional volumetric objects, which helps promoting essential innovations in many areas.⁵⁻¹⁰ One especially promising application is fabricating hydrogel-based scaffolds through photopolymerization with predesigned structures and functionality for tissue engineering.¹¹⁻¹³

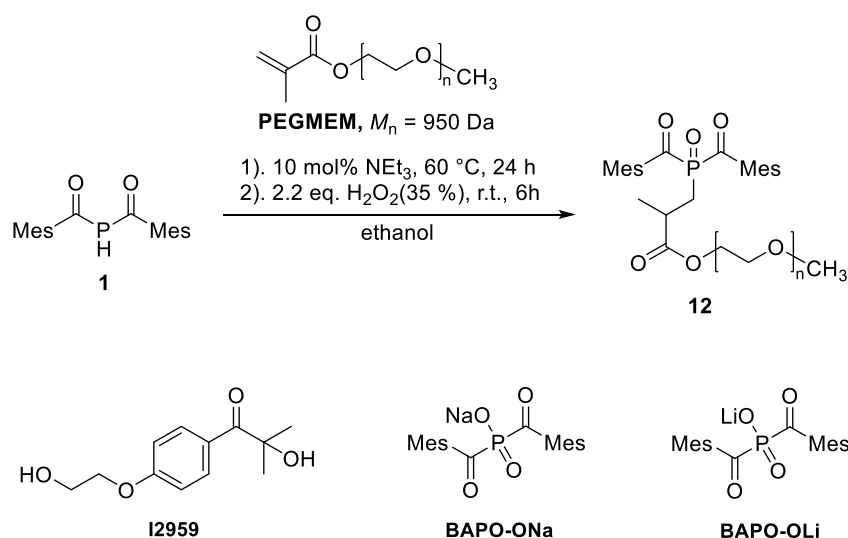
Photoinitiators (PIs) play a critical role in determining the photopolymerization efficiency and the properties of the printed objects.^{14,15} Currently, the commercially available Irgacure 2959 (Scheme 5.1) is the most frequently used PI in aqueous photocuring systems. However, limited water-solubility (0.5 wt%) and low efficiency under ultraviolet-visible light irradiation are serious drawbacks. Several approaches were developed to convert water-insoluble PIs into water compatible derivatives, but tedious synthetic procedures are often involved.¹⁶⁻¹⁹ Water-dispersible nanoparticles as PIs were recently reported for use in waterborne formulations.^{20,21} A variety of Norrish type II PIs show good solubility and biocompatibility, but exhibit lower reactivity than type I systems.²²

In this chapter, a new poly(ethylene glycol) substituted BAPO derivative (PEG-BAPO) was developed as a visible light photoinitiator for 3D printing of hydrogels. It can easily be dispersed

in water forming micelles, showing good storage stability and high photo-reactivity. A gyroid hydrogel structure was successfully printed on a commercially available digital light processing (DLP) 3D printer.

5.2 Synthesis and characterization of PEG-BAPO

PEG-BAPO (**12**) was synthesized following a straightforward one-pot procedure as shown in Scheme 5.1. The atom economic and efficient phospho-Michael addition of bis(mesityl)phosphane (**1**) onto a commercially available poly(ethylene glycol) methyl ether methacrylate (**PEGMEM**, $M_n = 950$ Da), followed by oxidation with aqueous H_2O_2 resulted in PEG-BAPO (**12**) as a yellow solid in good yield (72.1%).



Scheme 5.1 One-pot synthesis of PEG-BAPO and three other PIs studied in this chapter.

PEG-BAPO shows excellent dispersibility in water evidenced by the fact that 3 g can be easily dispersed in 7 mL of water at ambient temperature, resulting in a 30 wt% stable transparent solution. Since the BAPO group is hydrophobic while the polyether is hydrophilic, PEG-BAPO is supposed to form micelles in aqueous solution. This amphiphilic property was

verified by a comparison of ^1H NMR spectra of the compound in CDCl_3 and in D_2O with the same concentration (20 g/L). The weaker peak intensity of the methyl groups and up-field shifts in D_2O can be attributed to the formation of micelles (Figure 5.1).^{23,24}

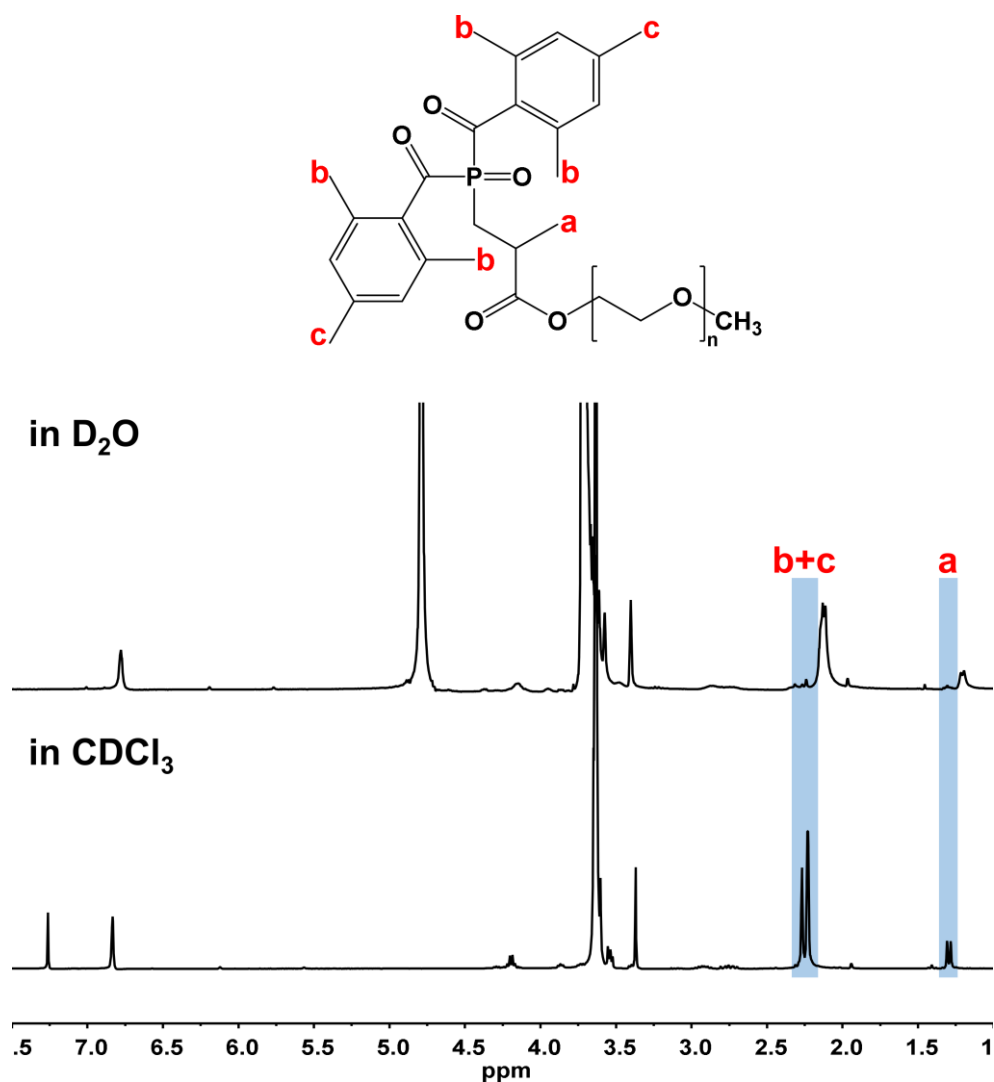


Figure 5.1 Comparison of ^1H NMR spectra of PEG-BAPO in D_2O and CDCl_3 with the same concentration (20 mg/mL). The ratio of BAPO group and polyether group is 1:28 in CDCl_3 and 1:33 in D_2O . The peak positions of methyl groups (a-c) of PEG-BAPO in D_2O are moved to up-field in comparison to the spectrum in CDCl_3 .

The critical micellar concentration (CMC) of PEG-BAPO was determined by surface tension measurements via Wilhelm plate method²⁵ in aqueous solutions at various concentrations. The CMC value is determined to be 1.07 mM at 25 °C (Figure 5.2), which is in good agreement

with the one determined from the analysis of ^1H NMR chemical shifts observed upon increasing the concentration of PEG-BAPO in D_2O (Figure 5.3). Dynamic light scattering (DLS) analysis suggests that micelle sizes of PEG-BAPO are around 10 nm when the concentrations are higher than CMC (Table 5.1). These micelles are hence much smaller than that of the water-dispersible nanoparticles of 2,4,6-trimethylbenzoyl-diphenylphosphine oxide (≥ 180 nm).²⁰

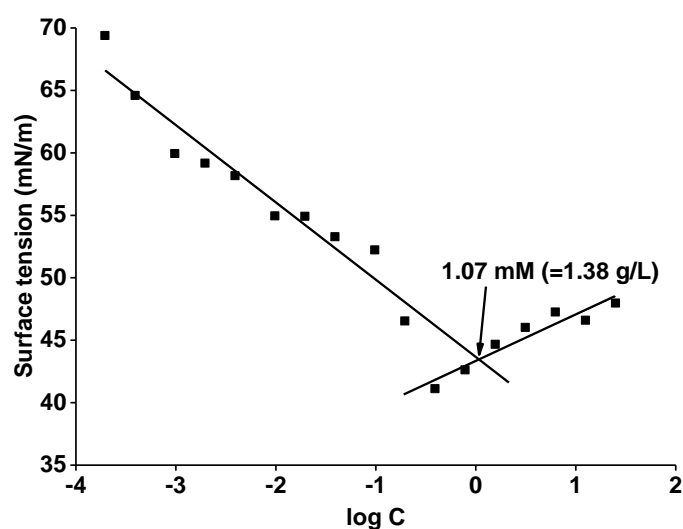


Figure 5.2 Determination of critical micelle concentration (CMC) of PEG-BAPO with a tensiometer in H_2O at 25 °C. The point of intersection of two lines indicates the CMC value (1.07 mM = 1.38 g/L).

Table 5.1 DLS measurement of PEG-BAPO in H_2O at different concentrations.

Conc. [g/L]	Z_{ave} [nm]	PDI
5	12.1	0.28
10	8.4	0.24
15	7.1	0.12
20	7.1	0.11

Z_{ave} = Z-average particle size; PDI = polydispersity index

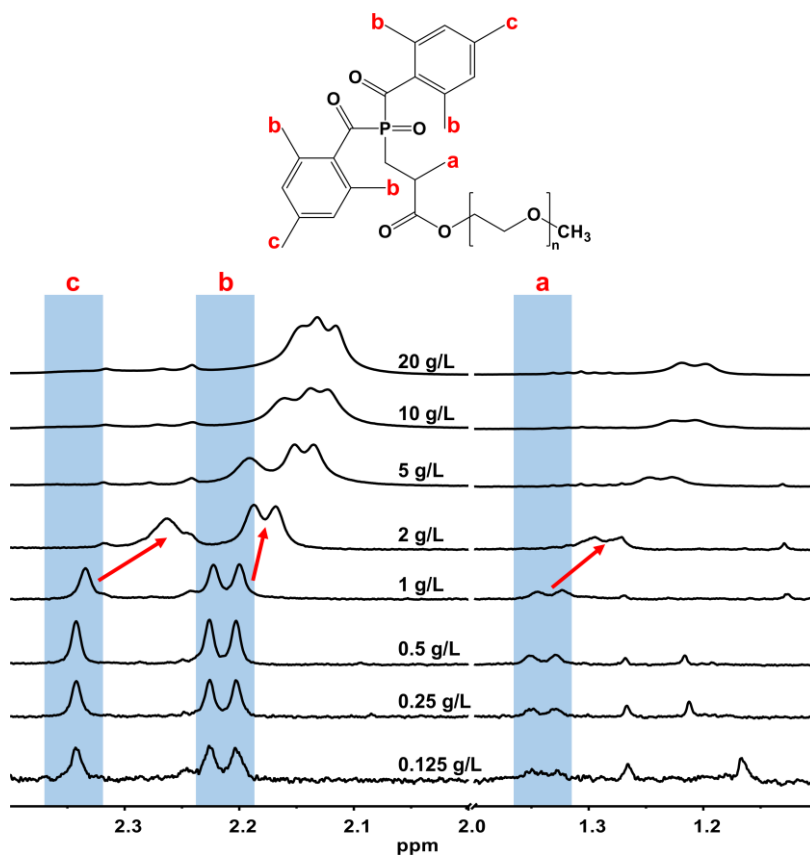


Figure 5.3 Selected regions of ^1H NMR spectra of PEG-BAPO at various concentrations in D_2O at 25°C . An obvious up-field shift of methyl groups (a-c) is observed when the concentration of PEG-BAPO in aqueous solutions increased from 1 g/L to 2 g/L, this suggests that the CMC is between these two concentrations.

The UV-Vis absorption spectrum of PEG-BAPO was measured and compared with those of other three PIs using a 1 mM aqueous solution (Figure 5.4). Irgacure 2959 only absorbs light in the UV-region. The two BAPO salts (BAPO- OLi^{22} and BAPO- ONa^{26} , Scheme 5.1) have strong absorption bands above 385 nm in water, which is the typical long-wave absorption for the $n \rightarrow \pi^*$ excitation of the $\text{C}=\text{O}$ group in a BAPO structure. PEG-BAPO exhibits higher molar extinction coefficients in the visible region from 390 to 430 nm as compared to the two BAPO salts. This makes it more efficient for photopolymerization of aqueous formulations under visible light irradiation.

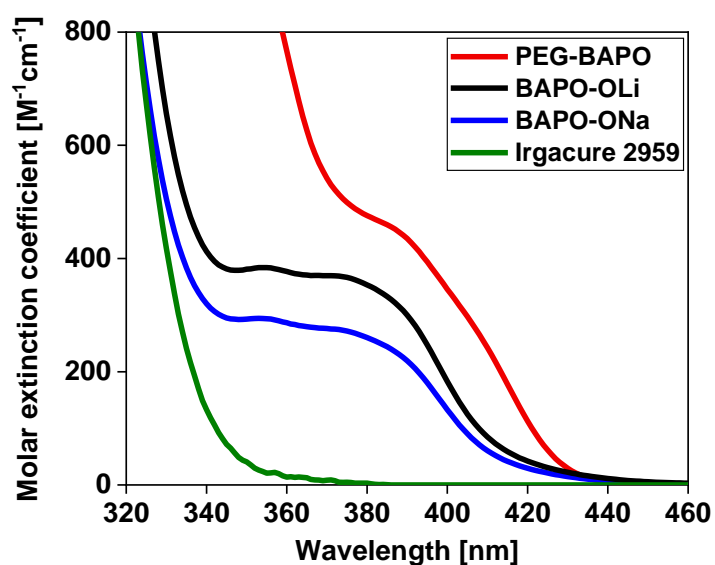


Figure 5.4 UV-Vis absorption spectra of the studied PIs in H₂O recorded at the same concentration (1 mM).

Photo-curable formulations, containing PIs, monomers, oligomers, and additives, often show acidic or basic properties because of impurities from the production process, or functional groups of the monomers and additives.²² Acylphosphane oxides are prone to nucleophilic attack and may undergo hydrolysis in an acidic and especially in a basic aqueous medium which severely limits the storage times of formulations containing these compounds.²⁷ The storage stability of PEG-BAPO was tested under neutral, acidic (pH = 2) and basic (pH = 11) conditions in the dark at room temperature during 20 days. PEG-BAPO shows good storage stability under all conditions (Figure 5.5). The remaining concentration is 92% in a basic environment, while higher values (> 96%) are achieved under neutral and acid conditions. The values are in the same range as state of the art acylphosphane oxide PIs,²² this makes PEG-BAPO possible for industrial applications.

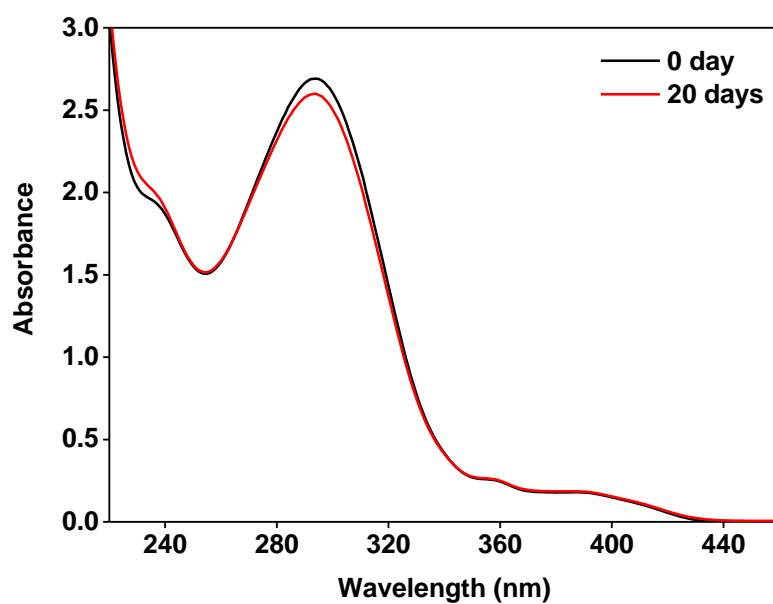


Figure 5.5a Storage stability test of PEG-BAPO in a neutral solution (MeCN/H₂O = 50/50 v/v). The remaining concentration is 97% after storing for 20 days in the dark at room temperature.

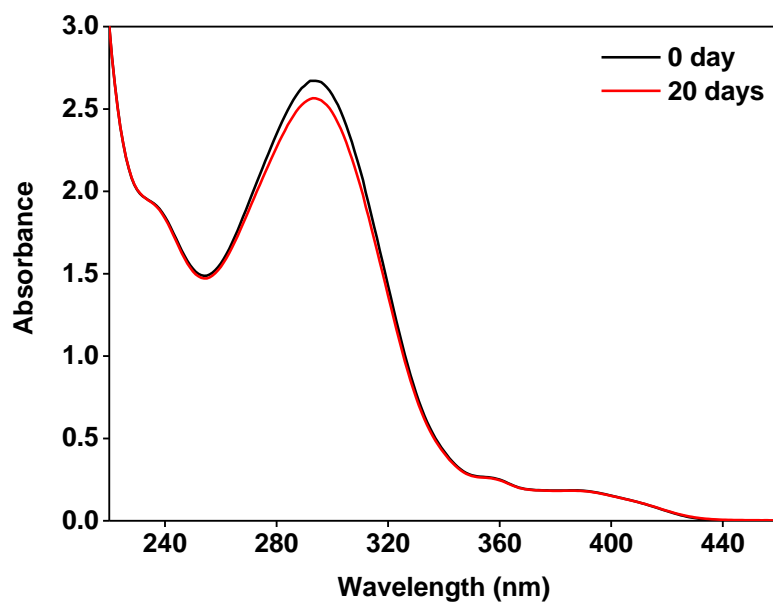


Figure 5.5b Storage stability test of PEG-BAPO in an acidic solution (MeCN/H₂O = 50/50 v/v with a few drops of HCl, pH = 2). The remaining concentration is 96% after storing for 20 days in the dark at room temperature.

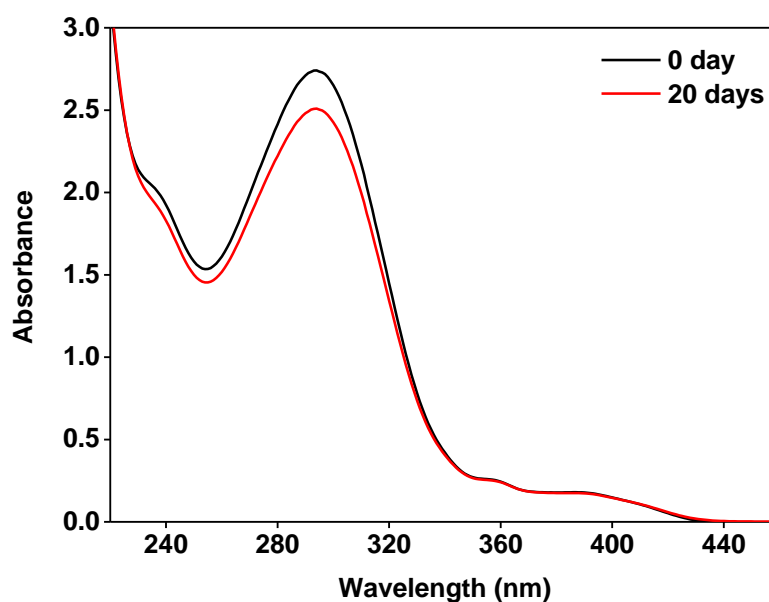


Figure 5.5c Storage stability test of PEG-BAPO in alkaline solutions (MeCN/H₂O = 50/50 v/v with a few drops of NaOH, pH = 11). The remaining concentration is 92% after storing for 20 days in the dark at room temperature.

5.3 Photoreactivity of PEG-BAPO

Photo-DSC measurements were performed to determine the efficiency of the four PIs (Figure 5.6). Aqueous formulations containing 50 wt% of poly(ethylene glycol) diacrylate (PEGDA, $M_n = 700$ Da) and 5 mM of PIs (BAPO-OLi, BAPO-ONa, PEG-BAPO, and Irgacure 2959) were irradiated with a LED-lamp (460 nm, 8 mW/cm²). This wavelength is well suited for biomedical or dental applications and avoids higher energy radiation which is harmful to biological materials. Irgacure 2959 is inactive at this wavelength due to the lack of absorption in the visible range. PEG-BAPO stands out and gives the shortest t_{max} (the time until the maximum heat of polymerization is reached) and $t_{95\%}$ (the time until 95% of the total polymerization enthalpy is reached) values of all the investigated photoinitiators (Table 5.2). Moderate values of double bond conversion (DBC) were achieved for all three BAPOs. This

might due to the low extinction coefficient of these BAPOs at 460 nm and the low intensity of the LED-lamp.

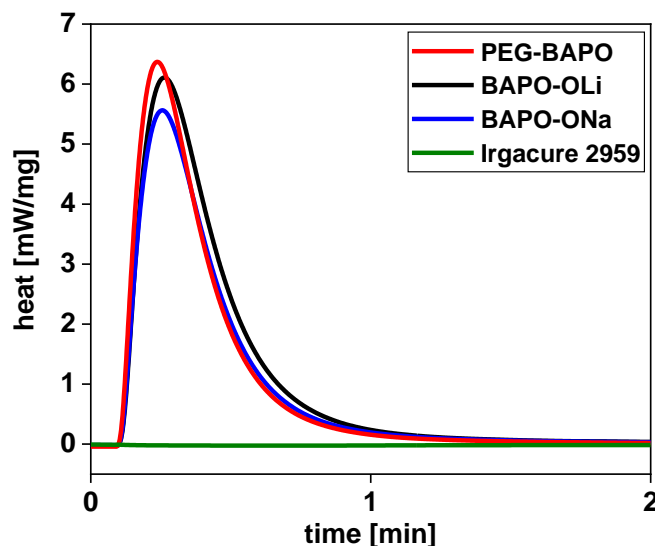


Figure 5.6 Photo-DSC curves of the four formulations.

Table 5.2 Photo-DSC data of PEGDA formulations.

PI	t_{\max} [s]	$t_{95\%}$ [s]	DBC [%]
Irgacure 2959	-	-	-
BAPO-ONa	23	76	52
BAPO-OLi	19	70	56
PEG-BAPO	14	53	55

Short t_{\max} [s] and $t_{95\%}$ [s] and high DBC values indicate high efficiency of the PI in a given formulation.

The three formulations with BAPO-OLi, BAPO-ONa, or PEG-BAPO were then studied by photo-rheology measurements²⁸ under the same irradiation conditions. Figure 5.7a compares the evolution of the shear moduli of the formulations during photopolymerization. PEG-BAPO shows higher reactivity than the other two PIs in agreement with the photo-DSC data. The delay

time (t_d) of PEG-BAPO is significantly shorter (Figure 5.7b), and the slope ($\Delta G'/\Delta t$), which is a measure for the polymerization rate, is about three times as high as for the two BAPO salts (Figure 5.7c). The final storage modulus reached with PEG-BAPO (561 kPa) is higher than that obtained with the other two PIs (they both reached 516 kPa).

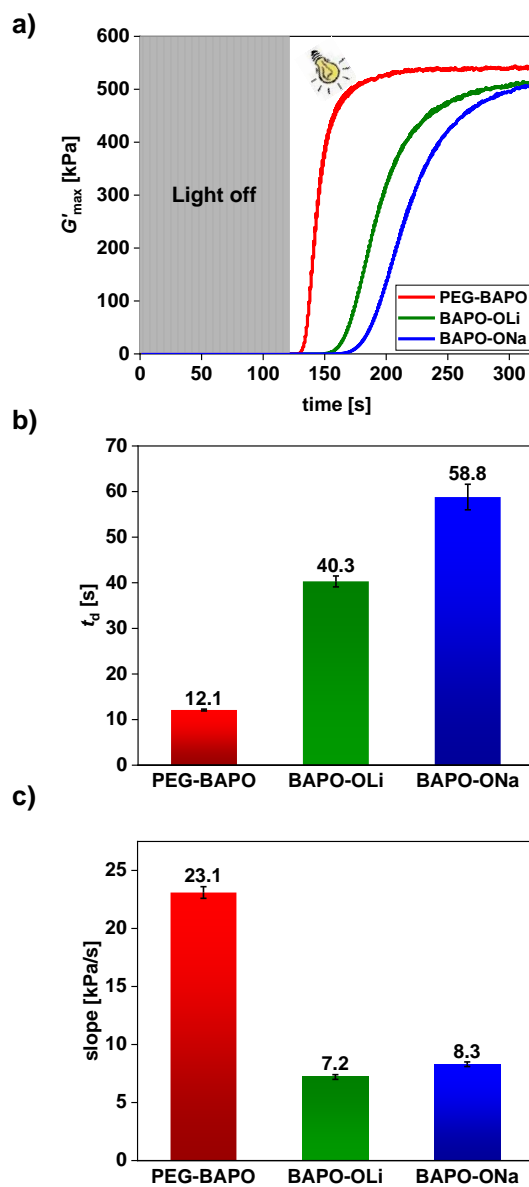


Figure 5.7 Photo-rheology measurements of the three formulations. (a) Photo-rheometer curves. The light was automatically turned on after 120 seconds. (b) Delay time (t_d) of the three different PIs. (c) Slope $\Delta G'/\Delta t$ of the three different PIs.

5.4 3D printing of hydrogel model using PEG-BAPO

Finally, the efficiency of PEG-BAPO as PI was evaluated for 3D printing of hydrogels. An aqueous formulation (Figure 5.8) containing the same amount of PEDGA and PEG-BAPO as before was tested on a DLP 3D printer (Lithoz CeraFab 7500, 460 nm, 64.2 mW/cm², Figure 5.9). 0.02 wt% of tartrazine was added as a visible light absorber to limit light penetration (see results of penetration tests, Table 5.3; printing parameters are listed in Table 5.4). Water soluble Na and Li salts of bis- and mono-acylphosphane oxides²² were also investigated but found to be inefficient initiators under these conditions.

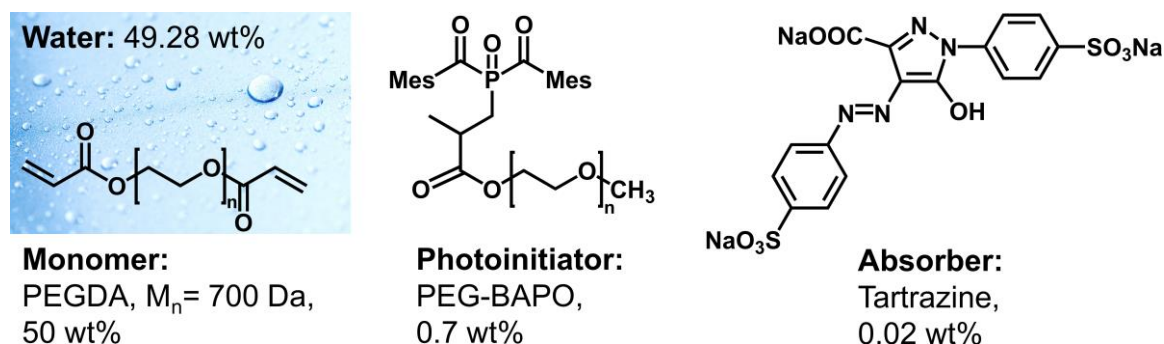


Figure 5.8 The aqueous formulation for 3D printing of hydrogels.

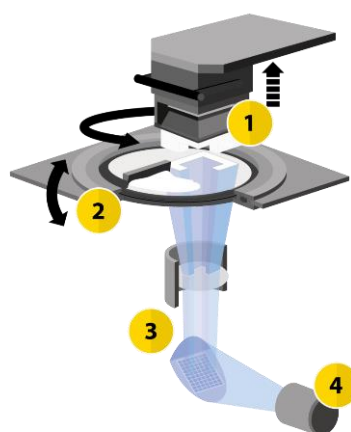


Figure 5.9 Schematic setup of CeraFab 7500 printer: 1 – building platform; 2 – rotating container; 3 – optical system; 4 – LEDs.

Table 5.3 Penetration tests of aqueous formulations.

Tartrazine conc. [wt%]	Exposure time [s]	Penetration depth [μm]
0	5	0
0	10	230
0	15	250
0.01	10	150
0.01	15	260
0.01	20	278
0.02	5	0
0.02	10	56

Table 5.4 Printing parameters for the gyroid hydrogel structure.

Parameter [units]	Value
Layer thickness [μm]	25
Light intensity [mW/cm ²]	64.2
Exposure time [s]	10
Waiting time [s]	4
Tilt up speed [steps/s]	20
Tilt down speed [steps/s]	20
Time per layer [s]	36

A well-defined gyroid structure could be successfully printed with PEG-BAPO and the stiffness of the structure was sufficient for further processing without breaking the structure (Figure 5.10a). Light microscopy images show good lateral precision (Figure 5.10b). A deviation in the z-direction (Figure 5.10c) can be attributed to the generally high penetration depth of the light in the aqueous formulation, which cannot be fully compensated by the limited amount of tartrazine (Table 5.3).

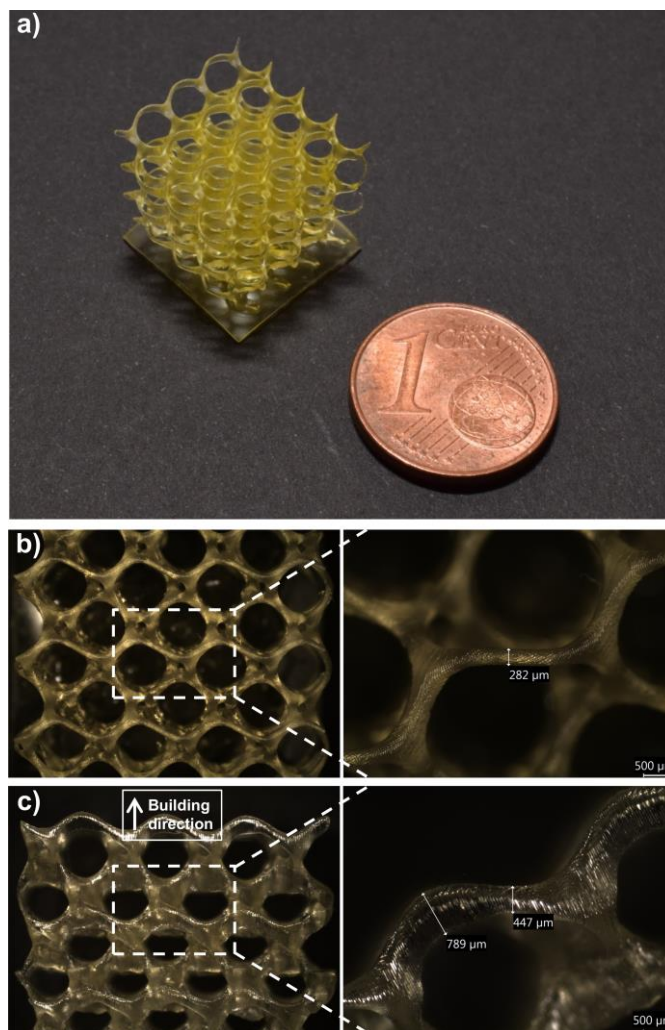


Figure 5.10 Photograph of a 3D printed hydrogel with gyroid structure (a). Light microscopy image of the hydrogel, the depicted view of the x,y-plane (b) and the z,y-plane (c).

5.5 Conclusion

An efficient one-pot procedure for the preparation of the highly efficient waterborne photoinitiator (PEG-BAPO) has been developed. PEG-BAPO shows good storage stability and higher reactivity than the state of the art visible light PIs. The unrivalled efficiency of PEG-BAPO is demonstrated by the 3D printing of an aqueous formulation to give a gyroid hydrogel

structure with LED light at 460 nm which now allows the simple and fast fabrication of other hydrogels in the future.

5.6 Methods

5.6.1 Critical micelle concentration (CMC) determination

The critical micellar concentration (CMC) of PEG-BAPO was determined by surface tension measurements via Wilhelm plate method⁴ in aqueous solutions at various concentrations, using a tensiometer DCAT 21 (Dataphysics, Germany) with a PT11 Wilhelmy plate (L: 10mm, W: 19.9mm, T: 0.2mm) at 25.0 ± 0.2 °C.

5.6.2 Dynamic light scattering (DLS) measurement

The sizes of micelles under different concentrations were characterized by DLS. The particle dispersions were measured at 25 °C in disposable plastic sizing cuvettes. All measurements were performed at an angle of 173° in backscattering mode and each sample was measured 3 times.

5.6.3 Storage Stability

The storage stability test was performed in three different solvents. MeCN/H₂O = 50/50 v/v for stability in neutral solutions, MeCN/H₂O = 50/50 v/v with a few drops of HCl (pH = 2) for stability in acidic solutions and MeCN/H₂O = 50/50 v/v with a few drops of NaOH (pH = 11) for stability in alkaline solutions. PEG-BAPO was dissolved in each solvent in a concentration of 1×10^{-3} mol/L and at $t = 0$ day UV-Vis spectra were measured. Afterward, the solutions were stored in the dark for 20 days at room temperature. At $t = 20$ days UV-Vis spectra were measured again. The concentration was diluted to 2×10^{-4} mol/L for all UV-Vis measurements

to ensure that the absorbance stays in the detection range of the UV-Vis spectrometer. The percentage of decline in absorbance at the maximum $\pi \rightarrow \pi^*$ transition of the C=O group ($\lambda_{\max} = 294 \text{ nm}$) is directly proportional to the percentage in concentration decline, therefore directly providing the remaining concentration of PEG-BAPO.

5.6.4 Photo-Differential Scanning Calorimetry (DSC)

Photo-DSC measurements were performed on a Netzsch DSC 204 F 1 at 25 °C under nitrogen atmosphere (20 mL/min) using a LED-lamp (Omnicure LX, 460 nm) at 8 mW/cm². Photoinitiators (PEG-BAPO, BAPO-ONa, BAPO-OLi and Irgacure 2959) were used in a concentration of 5 mM in an aqueous solution containing 50wt% of PEGDA. $10 \pm 0.5 \text{ mg}$ of the samples were weighed into the aluminum crucibles that were closed by a glass lid. At the beginning of the measurements, an isothermal period of 240 s was scheduled before the irradiation was activated for 300 s. Subsequently, another isothermal period of 60 s was observed before the second irradiation period of another 300 s was started. The DSC curve from the second irradiation period was subtracted from the first in order to provide a DSC curve, which excludes all thermal effects due to light dissipation. From the resulting DSC curves, t_{\max} , the time to reach the maximum of heat flux, $t_{95\%}$, the time to reach 95% of double bond conversion (DBC, Equation 1), and the DBC itself were extracted from the data obtained.

$$DBC = \frac{\Delta H_P \times M_w}{\Delta H_{0,P}} \quad (1)$$

ΔH_P Heat of polymerization [J/g] (area of the peak)

M_w Molecular weight of the monomer [g/mol]

$\Delta H_{0,P}$ Theoretical heat of polymerization of the monomer [J/mol] (for PEGDA 700, 155 kJ/mol was used)

5.6.5 Photorheological characterization

Rheometric measurements²⁹ were performed using an Anton Paar Modular Compact Rheometer MCR 302 WESP with a plate-to-plate measuring system consisting of a 25 mm steel stamp, a glass plate and a gap size of 50 μm in oscillation mode with 1 Hz and amplitude of 0.1 % strain at 25 °C. Samples were irradiated with a LED-lamp (Omniculture LX, 460 nm) bottom-up through the glass plate with light intensity (8 mW/cm^2) as measured at the top of the glass plate with an Oceanoptics USB200+ radiometer. Storage modulus G' was measured every second; the light was automatically turned on after 120 seconds and the measurement was continued for different, predefined periods. All measurements were done at least in triplicate.

The maximum storage modulus (G'_{max}) is a measure of the mechanical integrity and the crosslink density, respectively. The slope $\Delta G'/\Delta t$ of this linear fit was taken as a measure for the reactivity of the hydrogel formulation while the delay (or induction) time t_d (at the intersection of the linear fit with the abscissa) was defined as an indicator for the affinity of the formulation to gel. The gel point t_g , the intersection of the curves G' and G'' , was found to be equivalent to t_d , as no substantial increase of G' is observable before t_g is attained.

5.6.6 Penetration tests

A microscope slide was coated with a thin layer of formulation and subsequently exposed to a circular light spot with a diameter of 10 mm. This light exposure (460 nm) was performed for different durations at a light intensity of 64.2 mW/cm^2 . The light exposure initiated local photopolymerization in the exposed area and selectively cured the aqueous formulation. The non-solidified formulation was afterwards removed and the thickness of the cured hydrogel was measured using a micrometer screw. The thickness of the solidified hydrogel is equal to the light-penetration depth for the corresponding energy dose, which equals to the product of

irradiance value and light exposure time. Due to the low stiffness of the hydrogel, the obtained values are of course subject to a substantial measurement uncertainty; nonetheless, it is possible to deduce trends and determine basic parameters for the actual printing process.

5.6.7 3D-printing

3D structuring was done using a Lithoz CeraFab 7500 printer. The assembly of the CeraFab 7500-system comprises a rotating vat filled with the feed material. The light source illuminates the bottom side of the vat via a digital micro-mirror device. The building platform is above the vat and moves upwards the z-axis during the fabrication process.

The building envelope of the CeraFab-system is 76 x 43 x 150 mm. The resolution in the x/y-plane is 40 x 40 μm and for the structuring of the photocurable aqueous formulation, the layer thickness was set to 25 μm . The 3D-printing process relies on the concept of photopolymerization. A thin layer of resin is automatically coated onto the vat, the building platform approaches the vat, only leaving a small gap of a couple of 25 μm which remains filled with resin, this gap corresponds to the thickness of an individual layer in the printed object. Approximately 15 mL of the freshly prepared aqueous formulation comprising PEGDA (50 wt%), PEG-BAPO (5 mM, 0.7 wt%) and tartrazine (0.02 wt%) were poured into the vat before starting the printing process. The photosensitive compounds in the formulation are then cured by selective exposure with light of 460 nm wavelength - where the light hits the formulation the diacrylate compound photopolymerizes into a 3-dimensional network. After completing the layer, including a waiting time of 4 s, the building platform is elevated and the whole sequence is repeated all over again. The waiting time corresponds to the period before each curing sequence and the tilting parameters (tilt up and tilt down speed of 20 steps per second) correspond to the speed for approaching the part towards the vat before curing or separating the

part from the vat after curing, respectively. The total time per layer corresponds to a printing speed of approximately 2.4 mm/h in the z-direction. After the layer-by-layer structuring, the cured structures are removed from the building platform using a razorblade. Subsequently, they were carefully cleaned from the excess formulation by immersing the part in water.

5.7 References

- 1 K. Y. Lee and D. J. Mooney, *Chem. Rev.*, 2001, **101**, 1869-1880.
- 2 E. M. Ahmed, *Journal of Advanced Research*, 2015, **6**, 105-121.
- 3 Y. S. Zhang and A. Khademhosseini, *Science*, 2017, **356**, eaaf3627.
- 4 D. Seliktar, *Science*, 2012, **336**, 1124-1128.
- 5 T. S. Srivatsan and T. S. Sudarshan, *Additive Manufacturing: Innovations, Advances, and Applications*, Taylor & Francis, 2015.
- 6 J. R. Tumbleston, D. Shirvanyants, N. Ermoshkin, R. Januszewicz, A. R. Johnson, D. Kelly, K. Chen, R. Pinschmidt, J. P. Rolland, A. Ermoshkin, E. T. Samulski and J. M. DeSimone, *Science*, 2015, **347**, 1349-1352.
- 7 J. A. Lewis and B. Y. Ahn, *Nature*, 2015, **518**, 42-43.
- 8 F. Kotz, K. Arnold, W. Bauer, D. Schild, N. Keller, K. Sachsenheimer, T. M. Nargang, C. Richter, D. Helmer and B. E. Rapp, *Nature*, 2017, **544**, 337-339.
- 9 J. H. Martin, B. D. Yahata, J. M. Hundley, J. A. Mayer, T. A. Schaedler and T. M. Pollock, *Nature*, 2017, **549**, 365-369.
- 10 S. C. Ligon, R. Liska, J. Stampfl, M. Gurr and R. Mülhaupt, *Chem. Rev.*, 2017, **117**, 10212-10290.
- 11 B. Derby, *Science*, 2012, **338**, 921-926.
- 12 S. V. Murphy and A. Atala, *Nat. Biotechnol.*, 2014, **32**, 773-785.
- 13 J. Torgersen, X.-H. Qin, Z. Li, A. Ovsianikov, R. Liska and J. Stampfl, *Adv. Funct. Mater.*, 2013, **23**, 4542-4554.
- 14 Y. Yagci, S. Jockusch and N. J. Turro, *Macromolecules*, 2010, **43**, 6245-6260.
- 15 T. Billiet, M. Vandenhoute, J. Schelfhout, S. Van Vlierberghe and P. Dubruel, *Biomaterials*, 2012, **33**, 6020-6041.
- 16 B. D. Fairbanks, M. P. Schwartz, C. N. Bowman and K. S. Anseth, *Biomaterials*, 2009, **30**, 6702-6707.
- 17 S. Li, F. Wu, M. Li and E. Wang, *Polymer*, 2005, **46**, 11934-11939.

- 18 B. D. Fairbanks, S. P. Singh, C. N. Bowman and K. S. Anseth, *Macromolecules*, 2011, **44**, 2444-2450.
- 19 R. Liska, *J. Polym. Sci. A Polym. Chem.*, 2002, **40**, 1504-1518.
- 20 A. A. Pawar, G. Saada, I. Cooperstein, L. Larush, J. A. Jackman, S. R. Tabaei, N.-J. Cho and S. Magdassi, *Sci. Adv.*, 2016, **2**, e1501381.
- 21 A. A. Pawar, S. Halivni, N. Waiskopf, Y. Ben-Shahar, M. Soreni-Harari, S. Bergbreiter, U. Banin and S. Magdassi, *Nano Lett.*, 2017, **17**, 4497-4501.
- 22 S. Benedikt, J. Wang, M. Markovic, N. Moszner, K. Dietliker, A. Ovsianikov, H. Grützmacher and R. Liska, *J. Polym. Sci. A Polym. Chem.*, 2016, **54**, 473-479.
- 23 X. Cui, S. Mao, M. Liu, H. Yuan and Y. Du, *Langmuir*, 2008, **24**, 10771-10775.
- 24 Q. Q. Wu, Y. Xiong, J. J. Yang, H. D. Tang and S. Chen, *Macromol. Chem. Phys.*, 2016, **217**, 1569-1578.
- 25 A. Patist, S. S. Bhagwat, K. W. Penfield, P. Aikens and D. O. Shah, *Journal of Surfactants and Detergents*, 2000, **3**, 53-58.
- 26 G. Müller, M. Zalibera, G. Gescheidt, A. Rosenthal, G. Santiso-Quinones, K. Dietliker and H. Grützmacher, *Macromol. Rapid Commun.*, 2015, **36**, 553-557.
- 27 J. E. Baxter, R. S. Davidson, H. J. Hageman, G. T. M. Hakvoort and T. Overeem, *Polymer*, 1988, **29**, 1575-1580.
- 28 C. Gorsche, R. Harikrishna, S. Baudis, P. Knaack, B. Husar, J. Laeuger, H. Hoffmann and R. Liska, *Anal. Chem.*, 2017, **89**, 4958-4968.
- 29 C. Gorsche, R. Harikrishna, S. Baudis, P. Knaack, B. Husar, J. Laeuger, H. Hoffmann and R. Liska, *Anal. Chem.*, 2017, **89**, 4958-4968.

6 Bis(acyl)phosphane oxide-based polymeric photoinitiators

6.1 Introduction

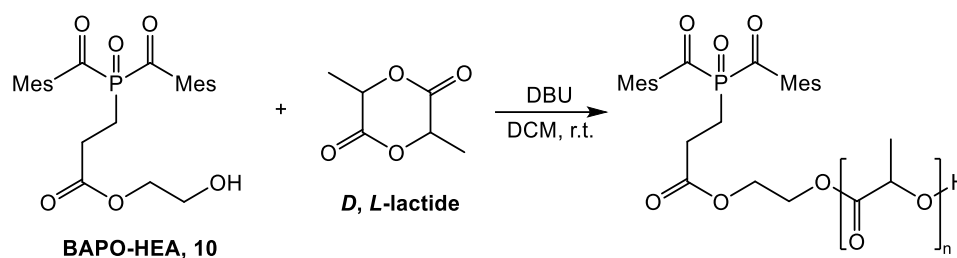
Polymeric photoinitiators are macromolecules containing covalently bonded photoactive groups, which can initiate polymerization of monomers or oligomers under light irradiation.¹ Compared to their corresponding low molecular weight analogues, polymeric photoinitiators possess various advantages, such as reduced migration, low volatility and improved compatibility in the formulations.²⁻⁷ Two strategies can be utilized in the preparation of polymeric photoinitiators. One is introducing a photoactive group as a pendant or in the terminal position into a polymer chain, the other is polymerization of monomers with photoactive groups.⁸⁻¹¹ In this chapter, polymeric photoinitiators with bis(acyl)phosphane oxide groups were synthesized according to these two strategies.

6.2 Polylactic acid with terminal BAPO group

Polylactic acid (PLA), currently the most synthetic biobased polymer on the market,¹² is a biodegradable and renewable thermoplastic polyester.¹³⁻¹⁴ It can be produced through the polycondensation of lactic acid or the ring-opening polymerization of lactide. The later route can produce PLA in a controlled manner, resulting in monodisperse PLA with a higher molecular weight.¹⁵ PLA is widely used in packaging, biomedical applications (such as bone fixations, tissue engineering, and drug delivery), inkjet printing and 3D printing.¹⁶⁻¹⁷

A photoactive PLA with a terminal BAPO unit (PLA-BAPO, **14**) was achieved by using BAPO-HEA (**10**) as an initiator for the ring-opening polymerization of *D, L*-lactide catalyzed

by 1,8-diazabicyclo[5.4.0]undec-7-ene (DBU) in DCM (Scheme 6.1). PLA-BAPO exhibits a narrow molecular weight distribution with PDI = 1.26 and $M_n = 17.1$ kg/mol (Figure 6.1).



Scheme 6.1 Synthesis of PLA-BAPO (**14**).

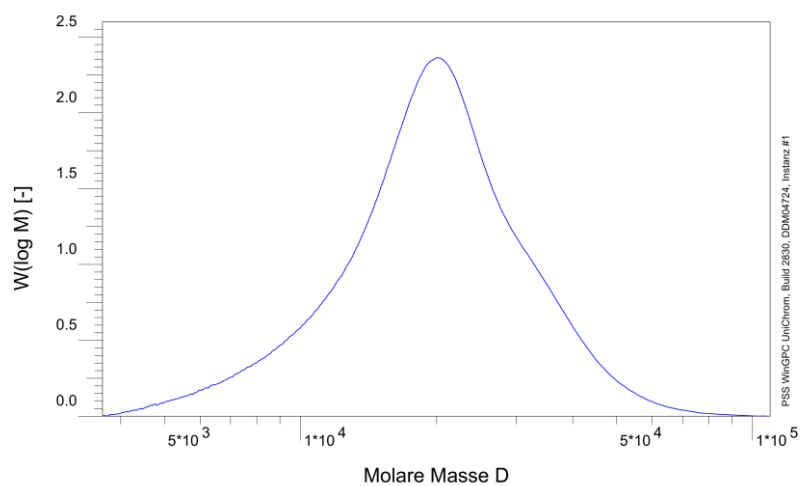


Figure 6.1 GPC analysis of PLA-BAPO.

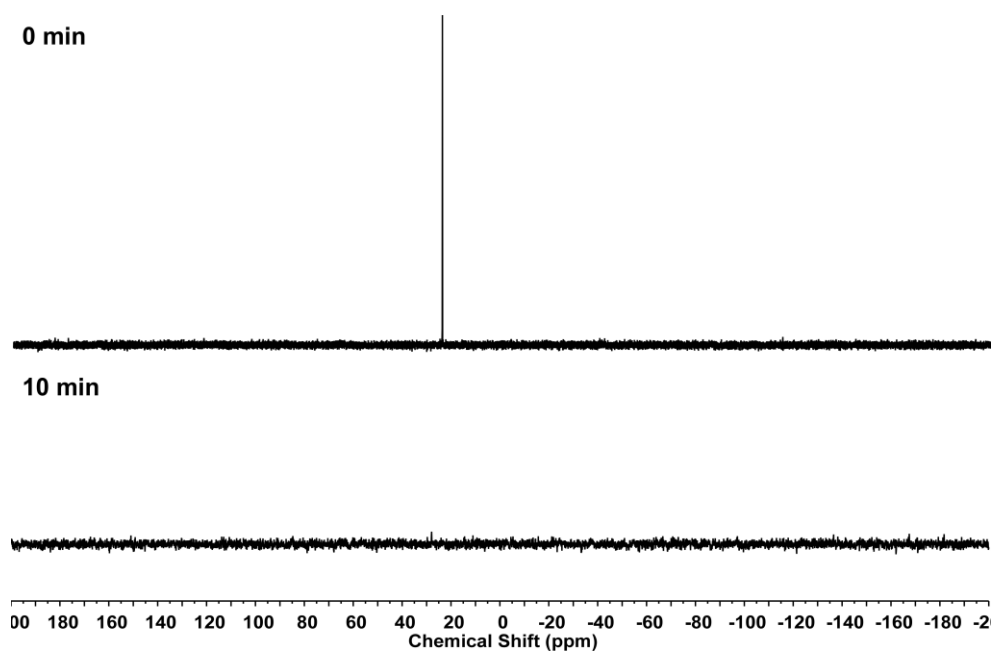


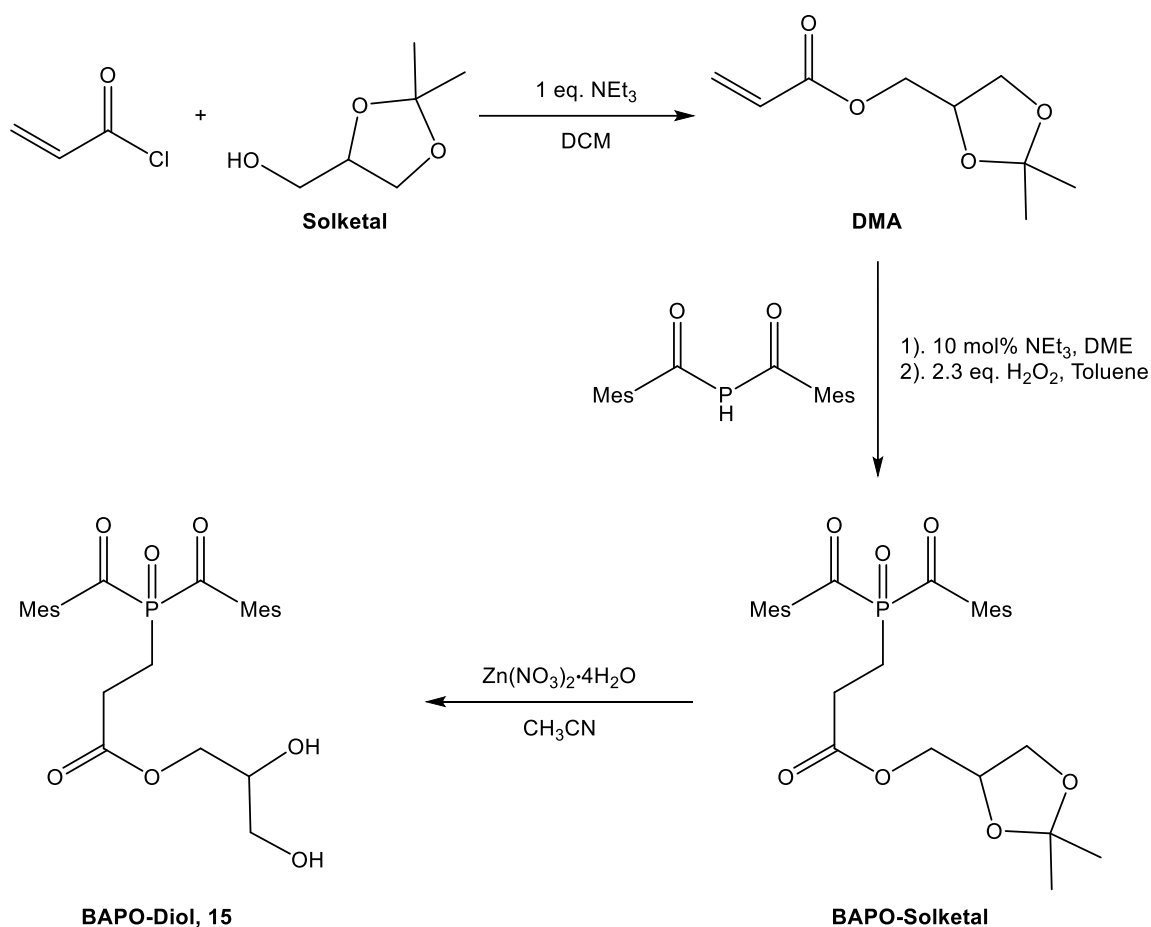
Figure 6.2 ^{31}P NMR spectra of a THF solution of PLA-BAPO. Before (upper) and after (lower) irradiation with a Hg vapor lamp for 10 min.

Upon irradiation (Hg vapor lamp, 10 min radiation time), PLA-BAPO shows rapid photobleaching to allow its application in block copolymer synthesis (Figure 6.2).

6.3 Polyurethane with side-chain BAPO (PU-BAPO)

Polyurethanes (PUs) are one of the key polymeric materials with various applications ranging from high-performance structural applications to foam padding.¹⁸⁻¹⁹ Linear PUs are commonly formed by reacting diols with diisocyanates in the presence of a catalyst. Here, a BAPO derivative with a diol functional group was synthesized for the preparation of photoactive PUs.

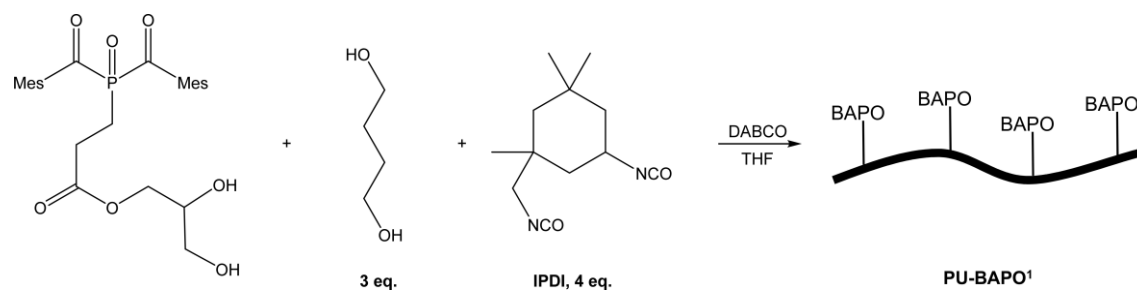
6.3.1 Synthesis of 2,3-dihydroxypropyl 3-(bis(2,4,6-trimethylbenzoyl)phosphoryl)propanoate (BAPO-Diol, 15)



Scheme 6.2 Synthesis of BAPO-Diol.

(2,2-Dimethyl-1,3-dioxolan-4-yl)methyl acrylate (DMA) was prepared from methacryloyl chloride and solketal, according to the literature.²⁰ The Michael addition of **1** onto DMA, followed by the oxidation of the phosphane, provided BAPO-Solketal as a yellow oil in high yield. A Lewis acid $\text{Zn}(\text{NO}_3)_2 \cdot 4\text{H}_2\text{O}$ ²¹ was applied for hydrolysis of BAPO-Solketal, resulting in BAPO-Diol (**15**) as a diol for PUs synthesis (Scheme 6.2).

6.3.2 Preparation of PUs-BAPO



Scheme 6.3 Synthesis of PU-BAPO¹.

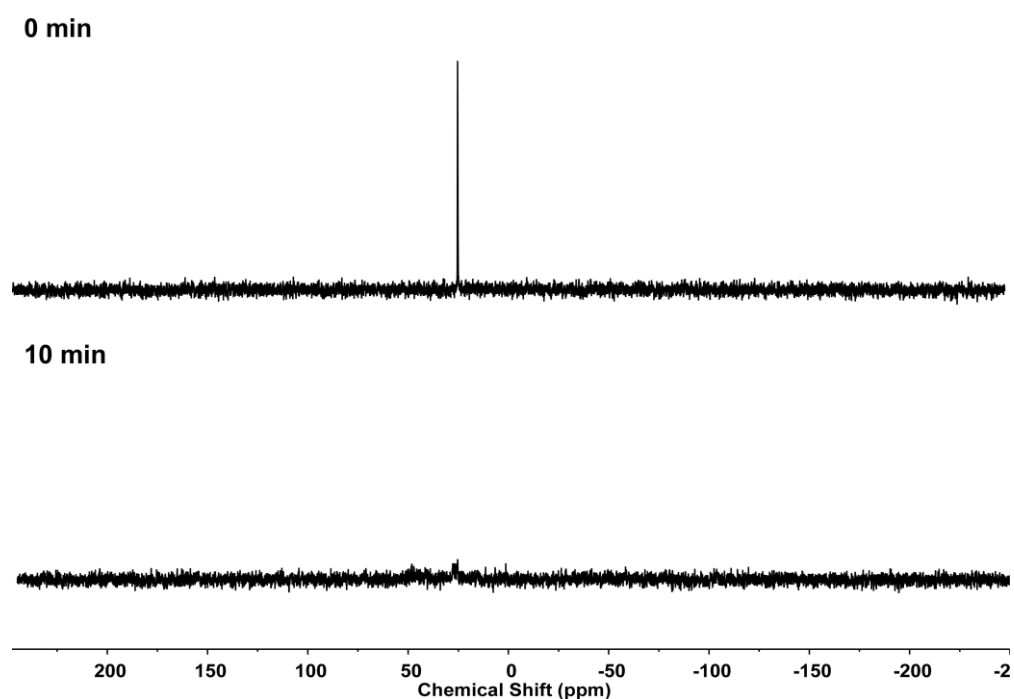


Figure 6.3 ³¹P NMR spectra of a THF solution of PU-BAPO¹. Before (upper) and after (lower) irradiation with a Hg vapor lamp for 10 min.

PU-BAPO¹ (**16**) was prepared by polycondensation of BAPO-Diol (**15**) with 1,4-butanediol (3 eq.) and isophorone diisocyanate (IPDI, 4 eq.) catalyzed by 1,4-diazabicyclo[2.2.2]octane (DABCO) in THF (Scheme 6.3). A GPC analysis gives the number average molecular weight (M_n) of PU-BAPO¹ for 3.0 kg/mol and PDI = 1.93. A THF solution of PU-BAPO¹ shows rapid photobleaching upon irradiation (Hg vapor lamp, 10 min radiation time, Figure 6.3).

PU-BAPO¹ was used to initiate the polymerization of methyl methacrylate under UV light irradiation, resulting in a graft polymer with higher molar mass ($M_n = 16.5$ kg/mol, PDI = 2.14, Figure 6.4).

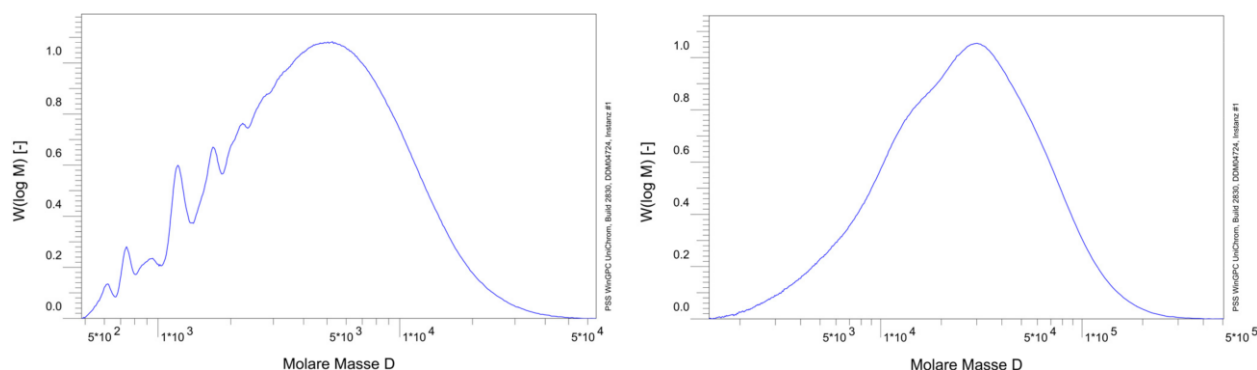
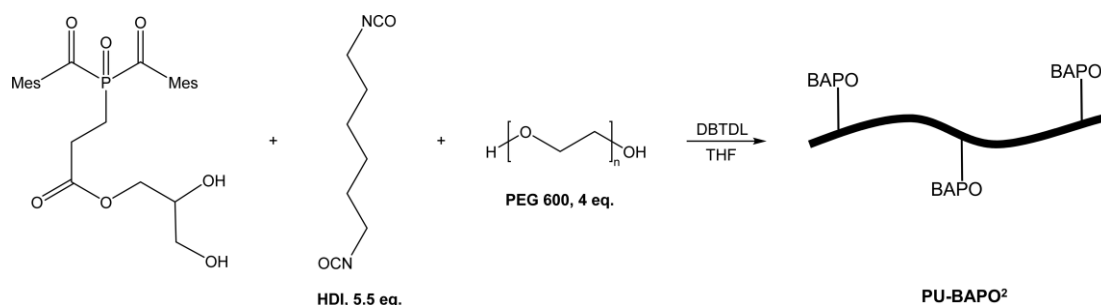


Figure 6.4 GPC analysis of PU-BAPO¹ (left) and PMMA graft polymer (right).

PU-BAPO² (**17**) was synthesized by polycondensation shown in scheme 6.4. Hexamethylene diisocyanate (HDI, 5 eq.) was used as a diisocyanate and polyethylene glycol 600 (PEG 600, 4 eq.) was used as a second diol to react with BAPO-Diol in the presence of dibutyltin dilaurate (DBTDL) as promotor. PU-BAPO² was precipitated in a large amount of n-hexane/diethyl ether mixed solvent (5 : 3) and isolated as a yellow powder (Figure 6.5 A). A GPC analysis gives the number average molecular weight (M_n) of PU-BAPO² for 12.6 kg/mol and PDI = 1.50. A thin film of PU-BAPO² can be obtained by solvent casting (Figure 6.5 B), due to sufficiently long polymer chains.



Scheme 6.4 Synthesis of PU-BAPO².

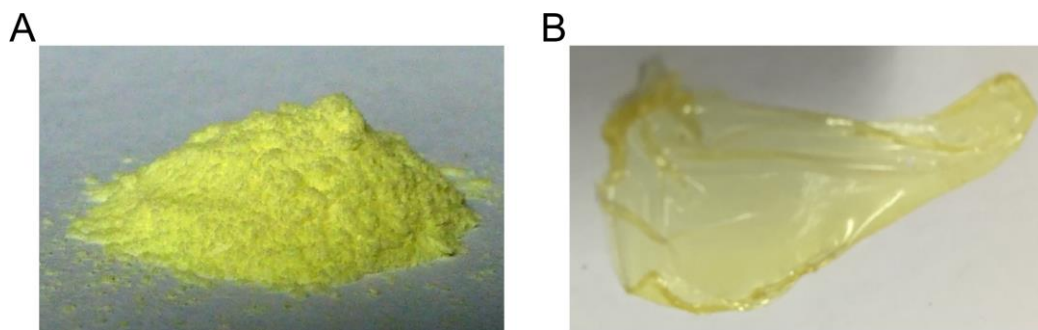


Figure 6.5 PU-BAPO powder (A). A thin film of PU-BAPO² by solvent casting of a 1 wt% THF solution (B).

6.4 Conclusion

Photoactive polymers with bis(acyl)phosphane oxide units were prepared via two strategies. One uses BAPO-HEA (**10**) as an initiator for the ring-opening polymerization of *D, L*-lactide, while the other utilizes the polycondensation of BAPO-Diol (**15**) with other diols and diisocyanates to make polyurethanes. Preliminary results show the possibility of using these polymeric photoinitiators for free-radical polymerization of unsaturated monomers.

6.5 References

1. Corrales, T.; Catalina, F.; Peinado, C.; Allen, N. S., Free radical macrophotoinitiators: an overview on recent advances. *Journal of Photochemistry and Photobiology A: Chemistry* **2003**, *159* (2), 103-114.
2. Sarker, A. M.; Sawabe, K.; Strehmel, B.; Kaneko, Y.; Neckers, D. C., Synthesis of Polymeric Photoinitiators Containing Pendent Chromophore–Borate Ion Pairs: Photochemistry and Photopolymerization Activities. *Macromolecules* **1999**, *32* (16), 5203-5209.
3. Jiang, X.; Yin, J., Dendritic Macrophotoinitiator Containing Thioxanthone and Coinitiator Amine. *Macromolecules* **2004**, *37* (21), 7850-7853.
4. Chen, Y.; Loccufier, J.; Vanmaele, L.; Frey, H., Novel multifunctional hyperbranched polymeric photoinitiators with built-in amine coinitiators for UV curing. *Journal of Materials Chemistry* **2007**, *17* (32), 3389-3392.

5. Temel, G.; Aydogan, B.; Arsu, N.; Yagci, Y., Synthesis and Characterization of One-Component Polymeric Photoinitiator by Simultaneous Double Click Reactions and Its Use in Photoinduced Free Radical Polymerization. *Macromolecules* **2009**, *42* (16), 6098-6106.
6. Karaca Balta, D.; Karahan, Ö.; Avci, D.; Arsu, N., Synthesis, photophysical and photochemical studies of benzophenone based novel monomeric and polymeric photoinitiators. *Progress in Organic Coatings* **2015**, *78*, 200-207.
7. Wang, K.; Yang, K.; Yu, Q., Novel polymeric photoinitiators with side-chain benzophenone: Facile synthesis and photopolymerization properties without coinitiator. *Progress in Organic Coatings* **2014**, *77* (11), 1929-1934.
8. Yilmaz, H.; Degirmenci, M.; Yilmaz, U.; Unal, H. I., End-chain and Mid-chain Functional Macrophotoinitiators of Poly([epsilon]-caprolactone) and Their Molar Mass Effects on Strong Electrorheological Response. *Polym. J* **2006**, *39* (1), 24-33.
9. Degirmenci, M.; Hizal, G.; Yagci, Y., Synthesis and Characterization of Macrophotoinitiators of Poly(ε-caprolactone) and Their Use in Block Copolymerization. *Macromolecules* **2002**, *35* (22), 8265-8270.
10. Chen, Y.; Loccufier, J.; Vanmaele, L.; Barriau, E.; Frey, H., Novel Multifunctional Polymeric Photoinitiators and Photo-Coinitiators Derived from Hyperbranched Polyglycerol. *Macromolecular Chemistry and Physics* **2007**, *208* (15), 1694-1706.
11. Degirmenci, M.; Alter, S.; Genli, N., Synthesis and Characterization of Well-Defined Mid-Chain Functional Macrophotoinitiators of Polystyrene by Combination of ATRP and “Click” Chemistry. *Macromolecular Chemistry and Physics* **2011**, *212* (15), 1575-1581.
12. Iwata, T., Biodegradable and Bio-Based Polymers: Future Prospects of Eco-Friendly Plastics. *Angewandte Chemie International Edition* **2015**, *54* (11), 3210-3215.
13. Jamshidian, M.; Tehrany, E. A.; Imran, M.; Jacquot, M.; Desobry, S., Poly-Lactic Acid: Production, Applications, Nanocomposites, and Release Studies. *Comprehensive Reviews in Food Science and Food Safety* **2010**, *9* (5), 552-571.
14. Lim, L. T.; Auras, R.; Rubino, M., Processing technologies for poly(lactic acid). *Progress in Polymer Science* **2008**, *33* (8), 820-852.
15. Södergård, A.; Stolt, M., Industrial Production of High Molecular Weight Poly(Lactic Acid). In *Poly(Lactic Acid)*, John Wiley & Sons, Inc.: 2010; pp 27-41.
16. Madhavan Nampoothiri, K.; Nair, N. R.; John, R. P., An overview of the recent developments in polylactide (PLA) research. *Bioresource Technology* **2010**, *101* (22), 8493-8501.
17. Van Wouwe, P.; Dusselier, M.; Vanleeuw, E.; Sels, B., Lactide Synthesis and Chirality Control for Polylactic acid Production. *ChemSusChem* **2016**, *9* (9), 907-921.

18. Sardon, H.; Pascual, A.; Mecerreyes, D.; Taton, D.; Cramail, H.; Hedrick, J. L., Synthesis of Polyurethanes Using Organocatalysis: A Perspective. *Macromolecules* **2015**, *48* (10), 3153-3165.
19. Engels, H.-W.; Pirkl, H.-G.; Albers, R.; Albach, R. W.; Krause, J.; Hoffmann, A.; Casselmann, H.; Dormish, J., Polyurethanes: Versatile Materials and Sustainable Problem Solvers for Today's Challenges. *Angewandte Chemie International Edition* **2013**, *52* (36), 9422-9441.
20. Oguchi, K.; Sanui, K.; Ogata, N.; Takahashi, Y.; Nakada, T., Relationship between electron sensitivity and chemical structures of polymers as electron beam resist. VII: Electron sensitivity of vinyl polymers containing pendant 1,3-dioxolan groups. *Polymer Engineering & Science* **1990**, *30* (8), 449-452.
21. Vijayasaradhi, S.; Singh, J.; Singh Aidhen, I., An Efficient, Selective Hydrolysis of Terminal Isopropylidene Acetal Protection by $Zn(NO_3)_2 \cdot 6H_2O$ in Acetonitrile. *Synlett* **2000**, *2000* (01), 110-112.

7 Summary and Outlook

This work describes the use of BAP-H (**1**) as a building block for the synthesis of functionalized BAPO photoinitiators. This is achieved by the atom-economic and convenient phospho-Michael addition of **1** to a variety of olefinic acceptors, resulting in phosphorous-functionalized BAPs, which can be easily oxidized to afford the corresponding BAPO derivatives. Various applications of the obtained BAPOs have been investigated in detail.

In Chapter 2, the synthetic route to the starting compound **1** has been improved on a kilogram scale. The salts generated during the synthesis were removed by washing with deionized water instead of filtration over Celite[®]. Excellent yield (90%) was obtained, which is higher than the previous protocol (81 %). In this route, shelf-stable red phosphorus was used instead of the toxic and flammable white phosphorus, but sodium was applied as the strongly reducing agent to activate red phosphorus. Facile methods for activating red phosphorus under mild conditions, and new atom-efficient synthetic strategy which avoids the generation of salts could be developed in future.

The phospho-Michael addition of methyl methacrylate with **1**, which was unsuccessful before, was achieved under two different reaction conditions. This extends the choice of active olefinics. Optimized procedures, including the choice of solvents and catalysts could be further studied.

A tri(methoxy)silyl-substituted BAPO derivative (**3**) was successfully fixed to non-porous glass surfaces for polymer grafting or covalently attached onto porous silica particles to obtain photoactive inorganic fillers. Other surfaces of diverse solids, such as silicon, ceramics,

titanium and aluminium could be further tested to form covalent bonds between solid surfaces and polymers. This favors interfacial interactions which eventually lead to superior properties.

A multifunctional BAPO photoinitiator comprising three photoactive groups (**6**) was obtained for the synthesis of star polymers via free radical photopolymerization. **6** can be selectively excited at different irradiation wavelengths, resulting in a star polymer consisting of three different polymer blocks, pMMA-pBMA-pBzMA. This provides access to materials with tailor-made properties under robust and environmentally favorable conditions. However, homopolymers generated by the cleaved acyl radicals require further purifications. New BAPOs with additional interactions between acyl groups and the phosphorous center could be developed for future applications.

BAPO functionalized ϵ -caprolactones (**8** and **9**) were synthesized by phospho-Michael addition of **1** onto cyclohex-2-en-1-one and subsequent Baeyer–Villiger oxidation. 4-BAPO-substituted lactone (**8**) and 6-BAPO-substituted lactone (**9**) were obtained with a ratio **8** : **9** = 1 : 0.29. Future work may concentrate on the ring-opening polymerization of these two compounds and applications of the generated photoactive polycaprolactones.

In Chapter 3, cellulose nanocrystals were functionalized with methacryloyl groups to which bis(acyl)phosphane was added by a phospho-Michael addition. Subsequent oxidation with H₂O₂ generated photoactive groups, which serve as initiators for free radical polymerization of acrylic monomers. Under mild and acid-free conditions, hybrid materials with excellent graft yields can be rapidly obtained, showing long-term dispersion stability in THF. Furthermore, the obtained PMMA grafted cellulose nanocrystals show an improved mechanical performance when dispersed in a PMMA matrix. In future work, other nanocellulose including cellulose nanofibers, bacterial nanocellulose and eventually wood surfaces could be functionalized using

the same modification strategy. This could render the wood surface more water repellent and insensitive to light.

In Chapter 4, a new BAPO with an isocyanate end group (**11**) was directly used to bind covalently to CNCs without any further modification of their surfaces. Subsequently, a mono-functional monomer was successfully grafted from the obtained photoactive nanomaterial without introducing any additional crosslinking between individual polymer chains, resulting in a stable network structure, which is otherwise impossible to achieve with conventional photoinitiators. Using this water dispersible nanomaterial, 3D structured objects were fabricated under mild conditions with a DLP 3D printer, which is equipped with energy-efficient UV-LEDs (405 nm). The obtained nanocomposite hydrogels show enhanced mechanical properties, outstanding swellability and good shape stability. A variety of nanomaterials possessing surface hydroxyl groups could be functionalized with this method, which may provide tougher hydrogels, elastomers or thermosets with superior functionalities in future.

In Chapter 5, a highly efficient water-soluble photoinitiator was synthesized for visible-light-induced 3D printing of hydrogels. The photoinitiator shows good storage stability in the same range as state of the art PIs but exceed them by far in solubility and reactivity. The biomedical applications need further studies.

In Chapter 6, BAPO-HEA (**10**) was applied as an initiator for the ring-opening polymerization of *D, L*-lactide, generating a photoactive polylactic acid with terminal BAPO group. Besides, the polycondensation of BAPO-Diol (**15**) with other diols and diisocyanates results in photoactive polyurethanes with side-chain BAPOs. Preliminary tests indicate that these photoactive polymers can be used as polymeric photoinitiators for free-radical

polymerization of unsaturated monomers. Same strategies might result in new polymeric photoinitiators with reduced migration, low volatility and improved compatibility in the formulations. However, the proper synthesis and applications of these polymeric photoinitiators require further investigations.

8 Experimental procedures

8.1 General techniques and chemicals

General techniques

All air- and moisture-sensitive manipulations were carried out using standard vacuum line Schlenk techniques or in a M Braun dry-box containing an atmosphere of purified argon.

DME, DMF, THF, n-hexane, diethyl ether and toluene were degassed and purified using an Innovative Technologies PureSolv system.

Chemicals

Standard chemicals were purchased from ABCR, Acros, Alfa Aesar, Fluka, Merck, Sigma-Aldrich and Strem or provided by BASF Switzerland.

8.2 Analytic methods

Solution NMR spectroscopy

NMR spectra were recorded on Bruker Avance 200, 250, 300, 400 and 500 spectrometers operating at room temperature if not specified otherwise. Chemical shifts δ were measured according to IUPAC and are given in parts per million (ppm) relative to TMS (^1H , ^{13}C , ^{29}Si) and H_3PO_4 (^{31}P). The multiplicity of the signals is indicated as s (singlet), d (doublet), t (triplet), q (quartet) or m (multiplet). The abbreviation br describes broad signals. Absolute values of coupling constants J are given in Hertz (Hz).

Solid-state ^{13}C and ^{31}P CP-MAS NMR spectroscopy

Solid-state ^{13}C and ^{31}P CP-MAS NMR spectra were recorded at RT on a Bruker Avance 400 NMR spectrometer (Bruker BioSpin AG, Fällanden, Switzerland) using a 4 mm CP-MAS probe. Approximately 30 - 40 mg of dried material was packed in a 4 mm zirconia rotor. The ^{13}C and ^{31}P CP-MAS NMR spectra were recorded at 100.6 and 162.0 MHz, respectively, using the following parameters: 3.5 μs 90° excitation pulse on ^1H channel, 3 ms contact time with a ramp from 100 to 50% of power level on the proton channel, 10,000 (^{13}C) and 13,000 Hz (^{31}P) MAS rates, 4 s relaxation delays, 71 kHz SPINAL 64 proton decoupling was applied during acquisition, and appropriate numbers of scans were recorded to yield reasonable signal-to-noise ratios.

Infrared spectroscopy (FTIR-ATR)

FT-IR spectra of the dried samples were recorded using a Tensor 27 FT-IR spectrometer (Bruker, Switzerland). For each sample, the diamond crystal of an Attenuated Total Reflectance (ATR) accessory was brought into contact with the area to be analyzed. The contact area was a circle of about 1.5 mm in diameter. All spectra were recorded between 4000 and 600 cm^{-1} with a resolution of 4 cm^{-1} and 32 scans per sample.

UV/vis spectroscopy

UV/vis spectra were recorded on an UV/vis/NIR lambda-19-spectrometer (range 200-600 nm) in 10 mm Quartz cells.

Mass spectrometry (MS)

Mass spectrometry measurements were carried out by the MS Service (Laboratory of Organic Chemistry) at ETH Zürich.

Elemental analysis (EA)

Analyses were carried out by the Micro-Laboratory (Laboratory of Organic Chemistry) at ETH Zürich.

Melting point determination

The melting points were determined with a Büchi M-560 device.

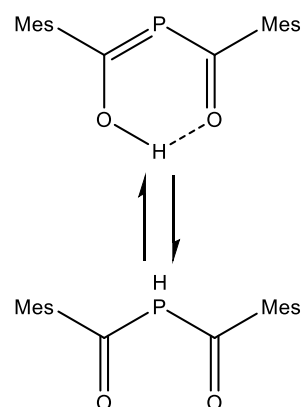
Gel permeation chromatography (GPC)

Measurements were performed on a Viscotek GPC unit. Detection: Triple Detector Array TDA 302 (refractive index, small and wide angle light diffraction and viscosity) and UV detector Viscotek 2500 ($\lambda = 254$ nm). The solution of a polymer sample is passed through two columns (Polymer Laboratories, PLgel 5 μ m Mixed-C and PLgel 5 μ m Mixed-D) to achieve a separation of polymers by size. The temperature was maintained at 35 °C during the measurement. The sample concentration was 1 mg/mL in DMF, the injection volume 100 μ L and the flow-rate 1 mL/min. Data analysis: universal calibration with 13 monodisperse PS standards.

8.3 Synthetic protocols

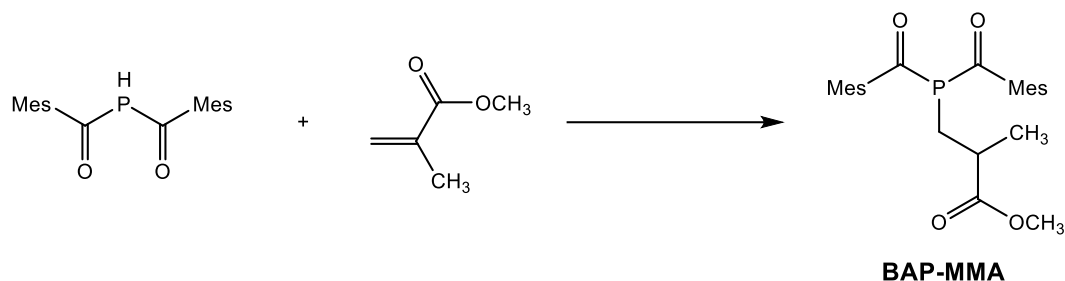
Bis(2,4,6-trimethylbenzoyl)hydrogenphosphane (1, BAP-H)

A suspension of red elemental phosphorus (127.71 g, 4.0 mol, 1 eq., 97%), naphthalene (51.78 g, 0.4 mol, 99.8%), and freshly cut sodium metal pieces (276.31 g, 12 mol, 3 eq., 99.8%) in DME (3 L) was prepared in a 6 L flask. The mixture was stirred at 0°C first by cooling in an ice bath, then stirred further for 2d at r.t. to yield a black suspension. After adding tert-butanol (377.2 mL, 4.0 mol, 1 eq., $\rho=0.79$, 99.5%) diluted in 200 mL DME dropwise at 0°C, the mixture was allowed to warm to r.t. and stirred for 7 h. Mesitoyl chloride (1491 g, 8.0 mol, 2 eq., 98%) was then added dropwise at 0°C. The mixture was allowed to warm to r.t. and stirred for 12h. Glacial acetic acid (240.93 g, 4.0 mol, 1 eq., 99.7%) was added to the yellow suspension dropwise at 0°C, then was allowed to warm to r.t. and stirred for 4 h, before moving the solvent under reduced pressure. The residual yellow solid was suspended in 12 L toluene, and washed with 5 L of deionized water. The residual yellow solution was dried over Na₂SO₄. After a filtration over celite, the solvent was removed under reduced pressure. The residual yellow solid was dried under high vacuum for 2 d to yield 1173.91 g (3.6 mol, 90%, $M = 326.38$ g/mol) of BAP-H.



Methyl 3-(bis(2,4,6-trimethylbenzoyl)phosphoryl)-2-methyl-propanoate (2, BAPO-MMA)

1. Synthesis of Methyl 3-(bis(2,4,6-trimethylbenzoyl)phosphaneyl)-2-methylpropanoate (BAP-MMA)



Route 1: A solution of BAP-H (3.264 g, 10 mmol) and tetramethylguanidine (0.12 mL, 1 mmol, 0.1 eq.) in DME (25 mL) was prepared in a 100 mL Schlenk flask. Methyl methacrylate (1.1 mL, 10.4 mmol, 1.04 eq.) was added. After stirring for 16 h at 50 °C, the solution was reduced *in vacuo* to 10 mL and layered with hexane (5 mL). The obtained pale yellow solid was collected by filtration and dried under high vacuum for 12 h to yield 3.92 g of BAP-MMA (9.2 mmol, 92%).

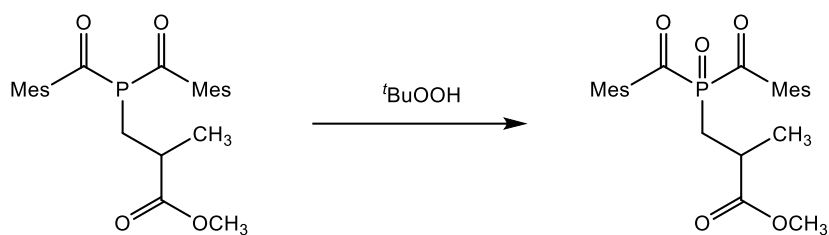
Route 2: A suspension of BAP-H (3.264 g, 10 mmol, 1 eq.) and triethylamine (0.14 mL, 1 mmol, 0.1 eq) in ethanol (25 mL) was prepared in a 100 mL Schlenk flask. Methyl methacrylate (1.1 mL, 10.4 mmol, 1.04 eq.) was added. After stirring for 20 h at 50 °C, the solvent was removed *in vacuo*. Subsequently, the yellow oil was dissolved in 20 mL Et₂O and layered with hexane (5 mL). The obtained pale yellow solid was collected by filtration and dried under high vacuum for 12 h to yield 3.79 g of BAP-MMA (8.9 mmol, 89%).

¹H-NMR (300.13 MHz, CDCl₃, 298 K): δ [ppm] = 1.23 (d, 3 H, CHCH₃, ³J_{HH} = 6.9 Hz), 2.19 (s, 12 H, *o*-CH₃ Mes), 2.26 (s, 6 H, *p*-CH₃ Mes), 2.38 (m, 2 H, CH₂P), 2.64 (m, 1 H, CHCO), 3.66 (s, 3 H, OCH₃), 6.74 (s, 4 H, H_{ar} Mes);

¹³C{¹H}-NMR (75.47 MHz, CDCl₃, 298 K): δ [ppm] = 18.5 (d, CHCH₃), 20.2 (d, ⁴J_{PC} = 5.3 Hz, *o*-CH₃ Mes), 21.3 (s, *p*-CH₃ Mes), 24.7 (d, ¹J_{PC} = 9.8 Hz, CH₂P), 37.7 (d, ²J_{PC} = 18.9 Hz, CHCO), 52.0 (s, OCH₃), 129.1 (s, C^{3,5} Mes), 133.7 (s, C^{2,6} Mes), 138.8 (d, ²J_{PC} = 27.9 Hz, C¹ Mes), 139.6 (s, C⁴ Mes), 176.0 (d, ³J_{PC} = 6.0 Hz), 217.3 (d, ¹J_{PC} = 47.6 Hz, COMes);

³¹P{¹H}-NMR (121.49 MHz, CDCl₃, 298 K): δ [ppm] = 48.9 ppm.

2. Oxidation of BAP-MMA



A solution of BAP-MMA (1.279 g, 3 mmol) in toluene (8 mL) was prepared in a 25 mL Schlenk flask. *tert*-Butyl hydroperoxide (0.6 mL, 3.3 mmol, 1.1 eq., 5.5 M in decane) was added dropwise at 0 °C. After stirring vigorously at r.t. for 7 h, the solvent was removed under reduced pressure. After recrystallization from diethyl ether/pentane (10 mL/5 mL, -20 °C), a yellow powder (**2**, BAPO-MMA) was obtained after removing the solvent under high vacuum for 14 h (1.075 g, 81.0%).

¹H-NMR (300.13 MHz, CDCl₃, 298 K): δ [ppm] = 1.29 (d, 3 H, CHCH₃, ³J_{HH} = 7.2 Hz), 2.24 (s, 6 H, *o*-CH₃ Mes), 2.25 (s, 6 H, *o*-CH₃ Mes), 2.27 (s, 6 H, *p*-CH₃ Mes), 2.27-2.33 (m, 1 H, PCH₂), 2.69-2.82 (m, 1 H, PCH₂), 2.83-3.00 (m, 1 H, CHCO), 3.63 (s, 3 H, OCH₃), 6.84 (s, 4 H, H_{ar} Mes).

¹³C{¹H}-NMR (75.47 MHz, CDCl₃, 298 K): δ [ppm] = 19.4 (d, ³J_{PC} = 7.9 Hz, CHCH₃), 19.9 (s, *o*-CH₃ Mes), 21.3 (s, *p*-CH₃ Mes), 29.2 (d, ¹J_{PC} = 54.3 Hz, CH₂P), 33.8 (d, ²J_{PC} = 3.6 Hz, CHCO), 52.2 (s, OCH₃), 129.4 (s, C^{3,5} Mes), 135.8 (d, ²J_{PC} = 41.4 Hz, C¹ Mes), 135.9 (d, ²J_{PC} = 40.9 Hz, C¹ Mes), 136.0 (d, ³J_{PC} = 16.4 Hz, C^{2,6} Mes), 141.5 (d, ⁵J_{PC} = 3.2 Hz, C⁴ Mes), 175.3 (d, ³J_{PC} = 7.9 Hz, COCH), 215.5 (d, ¹J_{PC} = 53.9 Hz, COMes), 215.9 (d, ¹J_{PC} = 53.2 Hz, C^oOMes).

³¹P{¹H}-NMR (121.49 MHz, CDCl₃, 298 K): δ [ppm] = 24.6 ppm.

IR (ATR [cm⁻¹]): 2982 (w), 2955 (w), 2920 (w), 2878 (w), 1731 (s), 1669 (s), 1643 (s), 1606 (s), 1454 (m), 1435 (m), 1383 (m), 1356 (m), 1300 (m), 1210 (s), 1188 (s), 1152 (s), 1121 (s), 1034 (s), 989 (w), 858 (s), 801 (s), 767 (s), 619 (m), 444 (m).

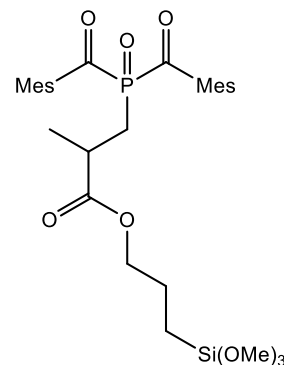
UV/Vis λ [nm] = 231(sh.), 282, 353, 384.

ESI MS [M + H]⁺ *m/z* = 443.1982, meas. 443.1981.

m.p. 65 °C.

4-(Trimethoxysilyl)butyl-3-[bis(2,4,6-trimethylbenzoyl)-phosphinoyl]-2-methylpropionate (3, TMESI²-BAPO)

A solution of BAP-H (11.984 g, 36.7 mmol) and 1,1,3,3-tetramethylguanidine (0.46 mL, 3.7 mmol, 0.1 eq.) in 50 mL toluene was prepared in a 100 mL Schlenk flask. 3-(Trimethoxysilyl)propyl methacrylate (9.305 g, 36.7 mmol, 1 eq.) was added. After stirring for 24 h at 60 °C, *tert*-butyl hydroperoxide (8 mL, 40.4 mmol, 1.1 eq., 5.5 M in decane) was added dropwise at 0 °C. After stirring vigorously at r.t. for 12 h, the solvent was removed under reduced pressure. The obtained yellow oil was washed with hexane (3 x 20 mL) and dried under high vacuum for 12 h to yield 19.51 g of the desired product TMESI²-BAPO (3) (33.0 mmol, 90%).



¹H-NMR (300.13 MHz, C₆D₆, 298 K): δ [ppm] = 0.51-0.58 (m, 2 H, SiCH₂), 1.17 (d, 3 H, CHCH₃, ³J_{HH} = 6.9 Hz), 1.62-1.74 (m, 2 H, SiCH₂CH₂), 1.95 (s, 6 H, *p*-CH₃ Mes), 2.35 (s, 6 H, *o*-CH₃ Mes), 2.41 (s, 6 H, *o*-CH₃ Mes), 2.40-2.46, 2.91-3.11 (m, 3 H, PCH₂CHCO), 3.39 (s, 9 H, Si(OCH₃)₃), 3.94 (t, 2 H, OCH₂, ³J_{HH} = 6.9 Hz), 6.54 (d, 4 H, *H*_{ar} Mes, ⁴J_{HH} = 2.4 Hz).

¹³C{¹H}-NMR (75.47 MHz, C₆D₆, 298 K): δ [ppm] = 5.7 (s, SiCH₂), 19.4 (d, ³J_{PC} = 8.5 Hz, CHCH₃), 20.2 (d, ⁴J_{PC} = 6.4 Hz, *o*-CH₃ Mes), 21.1 (s, *p*-CH₃ Mes), 22.5 (s, SiCH₂CH₂), 29.7 (d, ¹J_{PC} = 54.4 Hz, CH₂P), 34.4 (d, ²J_{PC} = 3.6 Hz, CHCO), 50.3 (s, OCH₃), 67.1 (s, OCH₂), 129.5 (d, ⁴J_{PC} = 5.0 Hz, C^{3,5} Mes), 136.4 (d, ³J_{PC} = 29.0 Hz, C^{2,6} Mes), 136.8 (d, ²J_{PC} = 41.4 Hz, C¹ Mes), 137.1 (d, ²J_{PC} = 40.9 Hz, C^{1'} Mes), 141.1 (d, ⁵J_{PC} = 9.6 Hz, C⁴ Mes), 174.8 (d, ³J_{PC} = 6.8 Hz, COCH), 216.7 (d, ¹J_{PC} = 54.6 Hz, COMes), 217.0 (d, ¹J_{PC} = 53.8 Hz, C^oOMes).

²⁹Si NMR (59.64 MHz, C₆D₆, 298 K) from ¹H - ²⁹Si HMQC: δ [ppm] = -42.3 ppm.

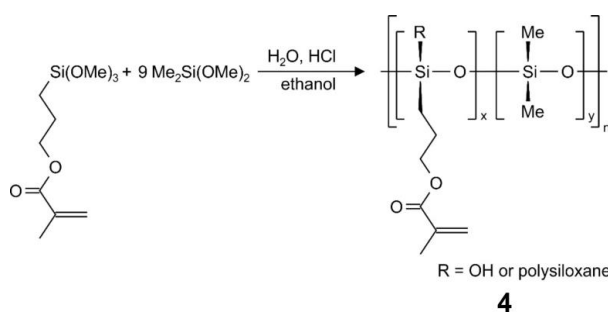
³¹P-NMR (121.49 MHz, C₆D₆, 298 K): δ [ppm] = 24.7 ppm (q, ³J_{PH} = 10.21 Hz).

IR (ATR [cm⁻¹]): 2942 (w), 2840 (w), 1732 (m), 1673 (m), 1607 (m), 1456 (m), 1192 (s), 1081 (s), 849 (m), 815 (s), 616 (m), 444 (m).

UV/Vis λ [nm] = 232 (sh.), 282, 353, 384.

ESI MS: [M + H]⁺ m/z = 591.2538, meas. 591.2537.

Acrylated polydimethylsiloxane (4)



3-(Trimethoxysilyl) propyl methacrylate (2.5 mL, 2.60 g, 10.5 mmol, 1 eq.), dimethyldimethoxysilane (13.1 mL, 11.33 g, 94 mmol, 9 eq.), ethanol (60 ml), and aqueous hydrochloric acid (1 M, 15 ml) were added in a 250 ml round bottom flask. The solution was stirred for four days in a closed vessel and eight additional days in an open vessel. The residual solution was dried at 60 °C under high vacuum. The acrylate functionalized silicone **4** was obtained as co(polymer) in form of a colorless oil.

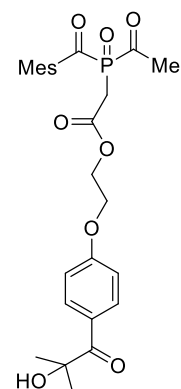
¹H-NMR (300.13 MHz, CDCl₃): δ [ppm] = 6.11 (br., 1H, acrylate), 5.54 (br., 1H, acrylate), 4.12 (t, *J* = 6.30 Hz, 2H, OCH₂), 1.95 (br., 3H, CqMe), 1.79–1.72 (br., 2H, CH₂CH₂Si), 0.64–0.59 (br., 2H, CH₂Si), 0.13–0.09 (br., 6H, SiMe₂).

¹³C{¹H}-NMR (75.47 MHz, CDCl₃): δ [ppm] = 167.4 (CO), 136.5 (Cq), 125.0 (CH₂, acrylate), 66.8–66.5 (br., OCH₂), 22.6 (br., CH₂CH₂Si), 18.3 (CqMe), 10.3–9.7 (br., CH₂Si), 1.5–0.9 (br., SiMe).

GPC (PMMA calibration): *M_n* = 1.85 kDa, *M_w* = 3.59 kDa, PDI = 1.94.

2-(4-(2-Hydroxy-2-methylpropanoyl)phenoxy)ethyl 2-(bis(2,4,6-trimethylbenzoyl)phosphoryl)acetate (5, prepared by Dr. Alex Huber)

In an 100 mL Schlenk flask, 2.023 g (5.05 mmol) of 2-(bis(2,4,6-trimethylbenzoyl)phosphoryl)acetic acid (BAPO-AA) was suspended in 60 mL toluene at 0 °C. Subsequently a slight excess of 0.813 g of oxalyl chloride (0.55 mL, 6.41 mmol, 1.27 eq.) and three droplets of anhydrous DMF were added. The yellow suspension was warmed to room temperature and degassed under slight vacuum to remove gas until a clear solution is obtained. All volatiles were removed under vacuum and the residue was re-dissolved in 15 mL of DCM. In a separate flask, 1.122 g of Irgacure® 2959 (5 mmol) were suspended in 15 mL DCM and to this suspension the solution of BAPO-AA-Cl was added within 10 minutes. The reaction mixture was kept under stirring at room temperature for one hour and then the solvent was removed under vacuum. The residue was dissolved in a small amount of chloroform and purified by column chromatography with hexane/ ethylacetate (2:1) as eluent to give 1.823g (3.01 mmol) of **5** as bright yellow powder (60 % isolated yield).



¹H-NMR (300.13 MHz, C₆D₆): δ [ppm] = 8.01 (d, J = 7.6 Hz, 2H, arom.), 6.91 (d, J = 7.6 Hz, 2H, arom.), 6.51 (s, 4H, *Mes*), 3.84 (t, J = 6.2 Hz, 2H, OCH₂), 3.63 (br., 1H, OH), 3.38 (d, J = 12.0 Hz, 2H, PCH₂), 2.34 (s, 12H, *o*-Me), 2.34 – 2.24 (m, 2H, OCH₂CH₂CH₂), 1.93 (s, 6H, *p*-Me), 1.55-1.48 (m, 2H, 2H, OCH₂CH₂), 1.44 (s, 6H, CH₃).

¹³C{¹H}-NMR (75.5 MHz, C₆D₆): δ [ppm] = 213.9 (d, J = 54.4 Hz, PCO), 203.5 (CO), 165.2 (d, J = 2.3 Hz, COO), 146.8 (arom.-C¹), 141.5 (*Mes*-C⁴), 136.6 (*Mes*-C²), 136.0 (*Mes*-C¹), 132.2 (arom.-C⁴), 130.4 (arom.-C²), 129.5 (*Mes*-C³), 128.5 (arom.-C³), 76.4 (C^{quart}), 64.9 (OCH₂), 34.9 (d, J = 48.6 Hz, PCH₂), 31.7 (OCH₂CH₂CH₂), 29.7 (OCH₂CH₂), 28.4 (CH₃), 20.9 (*p*-Me), 20.0 (*o*-Me).

³¹P{¹H}-NMR (121.5 MHz, C₆D₆): δ [ppm] = 18.3.

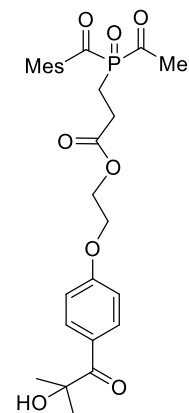
IR (ATR [cm⁻¹]): 3418 (br.), 2975 (w), 2927 (w), 1736 (s), 1669 (s), 1599 (s), 1507 (m), 1454 (m), 1420 (m), 1378 (m), 1246 (s), 1161 (s), 1106 (s), 1071 (m), 1036 (m), 957 (m), 848 (m), 765 (m), 738 (m), 618 (m), 590 (m), 559 (m).

ESI MS [M + Na]⁺ m/z = 629.2275, meas. 629.2274.

m.p. 190 °C (decomp.)

2-(4-(2-hydroxy-2-methylpropanoyl)phenoxy)ethyl 3-(bis(2,4,6-trimethylbenzoyl)phosphoryl)propanoate (6)

A solution of BAP-H (3.264 g, 10 mmol) and triethylamine (0.14 mL, 1 mmol, 0.1 eq.) in DME (40 mL) was prepared in a 100 mL Schlenk flask. 4-(2-Acryloyloxyethoxy)phenyl-2-hydroxy-2-propyl ketone (2.783 g, 10 mmol, 1 eq.) was added. After stirring for 18 h at room temperature, the solvent was removed under reduced pressure. The oily residue was dissolved in toluene (30 mL), tert-butyl hydroperoxide (2 mL, 11 mmol, 1.1 eq., 5.5 M in decane) was added dropwise at 0 °C. After stirring vigorously at r.t. for 6 h, the solvent was removed under reduced pressure. After recrystallization from a diethyl ether/pentane mixture (50 mL/20 mL, -20 °C), a yellow solid was obtained (5.142 g, 82.8%).



¹H-NMR (300.13 MHz, CDCl₃, 298 K): δ [ppm] = 1.62 (s, 6 H, CH₃), 2.22 (s, 12 H, *o*-CH₃ Mes), 2.27 (s, 6 H, *p*-CH₃ Mes), 2.47-2.59 (m, 2 H, PCH₂), 2.63-2.75 (m, 2 H, COCH₂), 4.23 (m, 2 H, COOCH₂), 4.46 (m, 2 H, CH₂O), 6.84 (s, 4 H, *H*_{ar} Mes), 6.93 (d, 2 H, ³*J*_{HH} = 9.0 Hz, *H*_{ar} Ph), 8.06 (d, 2 H, ³*J*_{HH} = 9.0 Hz, *H*_{ar} Ph).

¹³C{¹H}-NMR (75.47 MHz, CDCl₃, 298 K): δ [ppm] = 19.9 (s, *o*-CH₃ Mes), 21.4 (s, *p*-CH₃ Mes), 21.4 (d, ¹*J*_{PC} = 55.6 Hz, CH₂P), 26.2 (d, ²*J*_{PC} = 2.9 Hz, CH₂CO), 28.8 (s, CH₃), 63.2 (s, OCOCH₂), 66.0 (s, CH₂O), 76.0 (s, C quat.), 114.4 (s, C_{ar} Ph), 126.6 (s, C_{ar} Ph), 129.5 (s, C^{3,5} Mes), 132.5 (s, C_{ar} Ph), 135.8 (d, ²*J*_{PC} = 41.2 Hz, C¹ Mes), 135.9 (s, C^{2,6} Mes), 141.7 (s, C⁴ Mes), 162.3 (s, C_{ar} Ph), 171.8 (d, ³*J*_{PC} = 13.4 Hz, COCH₂), 202.8 (s, COPh), 215.4 (d, ¹*J*_{PC} = 53.1 Hz, COMes).

³¹P{¹H}-NMR (121.49 MHz, CDCl₃, 298 K): δ [ppm] = 24.6 ppm.

IR (ATR [cm⁻¹]): 3395 (br.), 2983 (w), 2968 (w), 2924 (w), 1737 (m), 1674 (s), 1599 (m), 1456 (m), 1187 (m), 1130 (m), 1058 (m), 952 (m), 846 (m), 815 (m), 700 (m);

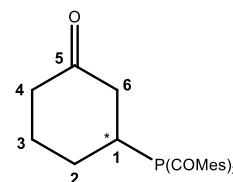
UV/Vis λ [nm] = 258, 297(sh.), 352, 386;

ESI MS [M + H]⁺ *m/z* = 621.2612, meas. 621.2605.

m.p. 117 °C, 213 °C (decomp.)

((3-Oxocyclohexyl)phosphanediyl)bis(mesitylmethanone) (7)

A solution of BAP-H (6.528 g, 20 mmol) and triethylamine (0.28 mL, 2 mmol, 0.1 eq.) in DME (50 mL) was prepared in a 100 mL Schlenk flask. Cyclohex-2-en-1-one (2.0 mL, 20 mmol, 1 eq.) was added. After stirring for 12 h at r.t., the solution was reduced *in vacuo* to 15 mL and layered with hexane (10 mL). The obtained pale yellow solid was collected by filtration and dried under high vacuum for 12 h to yield 7.613 g of **7** (18.0 mmol, 90 %).



¹H-NMR (400.13 MHz, C₆D₆, 298 K): δ [ppm] = 1.22-1.36, 1.57-1.68 (m, 2 H, **2**), 1.86-1.91, 2.16-2.24 (m, 2 H, **4**), 1.91-1.97, 2.02-2.10 (m, 2 H, **3**), 1.95 (s, 6 H, *p*-CH₃ Mes), 2.12 (s, 12 H, *o*-CH₃ Mes), 2.73-2.80, 2.93-3.02 (m, 2 H, **6**), 2.80-2.89 (m, 1 H, **1**).

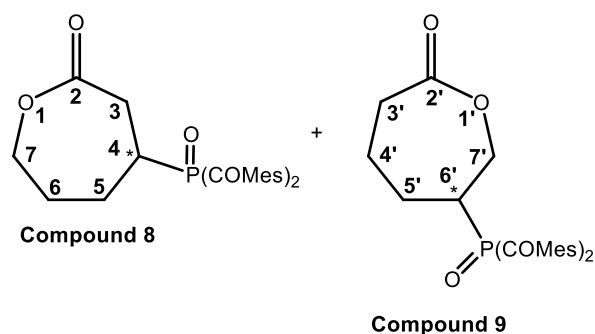
¹³C{¹H}-NMR (100.61 MHz, C₆D₆, 298 K): δ [ppm] = 20.4 (d, ⁴*J*_{PC} = 5.9 Hz, *o*-CH₃ Mes), 21.0 (s, *p*-CH₃ Mes), 26.9, 27.0 (s, **2**), 28.4, 28.5 (s, **3**), 34.4, 34.5 (s, **1**), 41.1 (s, **4**), 44.2, 44.2 (s, **6**), 129.1 (s, C^{3,5} Mes), 133.8 (s, C^{2,6} Mes), 139.3 (s, C⁴ Mes), 139.4 (d, ²*J*_{PC} = 28.3 Hz C¹ Mes), 206.9 (d, ¹*J*_{PC} = 9.6 Hz, COMes), 216.4 (d, ¹*J*_{PC} = 51.7 Hz, C'OMes).

³¹P{¹H}-NMR (161.98 MHz, C₆D₆, 298 K): δ [ppm] = 71.0 ppm.

IR (ATR [cm⁻¹]): 2942 (m), 2919 (m), 2859 (m), 1714 (s), 1626 (s), 1609 (s), 1446 (s), 1421 (s), 1376 (m), 1205 (m), 1142 (m), 1027 (m), 955 (w), 889 (m), 840 (m), 723 (m), 614 (m).

((2-oxooxepan-4-yl)phosphoryl)bis(mesitylmethanone) (8) & ((7-oxooxepan-3-yl)phosphoryl)bis(mesitylmethanone) (9)

The cyclohexanone substrate **7** (4.23 g, 10 mmol) was dissolved in 35 mL DCM and cooled with an ice bath. Subsequently, *m*CPBA (6.725 g, 30 mmol, 3 eq.) suspended in 55 mL DCM was added dropwise at 0 °C then the reaction mixture was stirred for 2 days at room temperature. The reaction mixture was filtered and washed with 20



mL cold DCM. The solution was collected and washed with saturated NaHCO₃ (40 mL × 2) and the organic layer was concentrated under vacuum. After recrystallization from a diethyl ether/pentane mixture (50 mL/20 mL, -20 °C), a yellow solid was obtained (3.103 g, 68.3%). 4-BAPO-substituted lactone (**8**) and 6-BAPO-substituted lactone (**9**) were obtained with the ratio **8** : **9** = 1 : 0.28.

¹H-NMR (500.2 MHz, CDCl₃, 298 K): δ [ppm] = 1.64-1.73 (m, 1 H, **5'**), 1.80-2.16 (m, 2 H of **5**, 1H of **6**, 1H of **5'**), 2.15-2.31 (*o*-CH₃ and *p*-CH₃ Mes of compound **8** and **9**), 2.32-2.39 (m, 2 H, **6**), 2.41-2.49 (m, 2 H, **4'**), 2.62-2.79 (m, 4 H, **4**, **3'** and **6'**), 2.82-2.98 (m, 2 H, **3**), 4.15-4.24 (m, 1 H, **7**), 4.29-4.38 (m, 1 H, **7**), 4.48-4.56 (m, 1 H, **7'**), 4.58-4.66 (m, 1 H, **7'**), 6.84, 6.85 (s, 4 H, *H*_{ar} Mes of compound **8**), 6.79-6.96 (4 H, *H*_{ar} Mes of compound **9**).

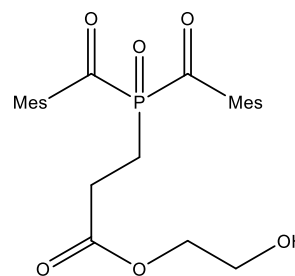
¹³C{¹H}-NMR (125.7 MHz, CDCl₃, 298 K): δ [ppm] = 19.8, 20.0 (s, *o*-CH₃ Mes of compound **9**), 19.9, 20.0 (s, *o*-CH₃ Mes of compound **8**), 21.4, 21.4 (s, *p*-CH₃ Mes), 23.1, 23.2 (s, **5'**), 27.8, 27.9 (s, **6**), 28.2, 28.2 (s, **4'**), 29.3, 29.5 (s, **5**), 33.6 (s, **3**), 33.9 (s, **3'**), 33.9 (d, ¹J_{PC} = 50.3 Hz, **4**), 40.7 (d, ¹J_{PC} = 45.3 Hz, **6'**), 67.1, 67.1 (s, **7'**), 68.7 (s, **7**), 129.5, 129.7 (s, C^{3,5} Mes of compound **8**), 129.5, 129.6 (s, C^{3,5} Mes of compound **9**), 135.7 (d, ²J_{PC} = 41.5 Hz, C¹ Mes of compound **9**), 135.8 (d, ²J_{PC} = 40.2 Hz, C¹ Mes of compound **8**), 135.8 (d, ²J_{PC} = 40.2 Hz, C^{1'} Mes of compound **8**), 136.0, 136.2 (s, C^{2,6} Mes of compound **9**), 136.1, 136.5 (s, C^{2,6} Mes of compound **8**), 141.9, 142.2 (s, C⁴ Mes of compound **8**), 142.0, 142.1 (s, C⁴ Mes of compound **9**), 172.7, 172.9 (s, **2**), 174.9 (s, **2'**), 214.0 (d, ¹J_{PC} = 46.5 Hz, COMes of compound **8**), 214.1 (d, ¹J_{PC} = 46.5 Hz, C'OMes of compound **8**), 214.6 (d, ¹J_{PC} = 45.3 Hz, COMes of compound **9**).

³¹P{¹H}-NMR (202.4 MHz, CDCl₃, 298 K): δ [ppm] = 27.3 ppm (**8**), 24.8 ppm (**9**).

ESI MS [M + NH₄]⁺ m/z = 472.2247, meas. 472.2243.

2-Hydroxyethyl 3-(bis(2,4,6-trimethylbenzoyl)phosphoryl)propanoate (10, BAPO-HEA)

A solution of bis(mesityl)phosphane (13.06 g, 40 mmol, 1 eq.) and triethylamine (0.56 mL, 4 mmol, 0.1 eq.) in DME (100 mL) was prepared in a 250 mL Schlenk flask. 2-Hydroxyethyl acrylate (4.3 mL, 40 mmol, 1 eq.) was added. After stirring for 12 h at room temperature, the solvent was removed under reduced pressure. The yellow oily residue was dissolved in toluene (80 mL) and aqueous hydrogen peroxide (7.9 mL, 80 mmol, 2 eq., 35%) was added dropwise at 0 °C. After stirring vigorously at r.t. for 6 h, the solvent was removed under reduced pressure. After recrystallization from diethyl ether/pentane (80 mL/30 mL, -20 °C), a yellow powder was obtained after removing the solvent under high vacuum for 14 h (16.42 g, 89.5%).



¹H NMR (300.13 MHz, CDCl₃, 298 K): δ [ppm] = 2.24 (s, 12 H, *o*-CH₃ Mes), 2.28 (s, 6 H, *p*-CH₃ Mes), 2.53-2.75 (m, 4 H, PCH₂CH₂), 2.98 (b, 1 H, OH), 3.67 (t, 2 H, ³J_{HH} = 4.5 Hz, CH₂OH), 4.20 (m, 2 H, ³J_{HH} = 5.1 Hz OCH₂), 6.86 (s, 4 H, H_{ar} Mes).

¹³C{¹H} NMR (75.47 MHz, CDCl₃, 298 K): δ [ppm] = 19.9 (s, *o*-CH₃ Mes), 21.4 (s, *p*-CH₃ Mes), 21.7 (d, ¹J_{PC} = 54.8 Hz, CH₂P), 26.9 (d, ²J_{PC} = 4.2 Hz, CH₂CO), 60.7 (s, OCOCH₂), 67.1 (s, CH₂OH), 129.5 (s, C^{3,5} Mes), 135.7 (d, ²J_{PC} = 41.4 Hz, C¹ Mes), 136.0 (s, C^{2,6} Mes), 141.8 (s, C⁴ Mes), 171.6 (d, ³J_{PC} = 8.2 Hz, COCH₂), 215.2 (d, ¹J_{PC} = 53.7 Hz, COMes).

³¹P{¹H} NMR (121.49 MHz, CDCl₃, 298 K): δ [ppm] = 24.8 ppm.

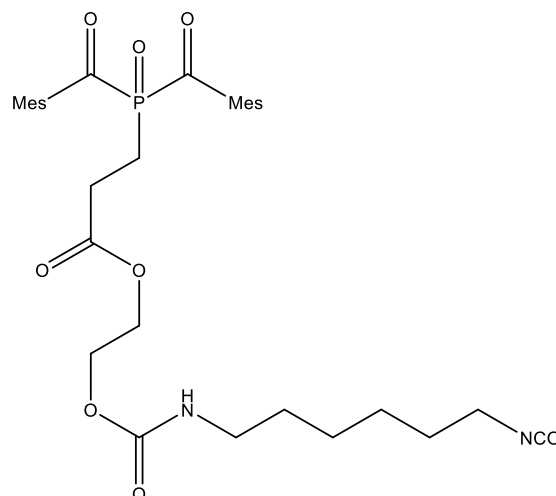
IR (ATR [cm⁻¹]): 2951 (w), 1743 (m), 1672 (m), 1643 (m), 1604 (m), 1182 (s), 1070 (m), 1042 (m).

ESI MS [M + H]⁺ m/z = 459.1931, meas. 459.1928.

m.p. 78°C.

2-([6-isocyanatohexyl]carbamoyloxy)ethyl 3-(bis(2,4,6-trimethylbenzoyl) phosphoryl) propanoate (11, BAPO-NCO)

A solution of hexamethylene diisocyanate (11.7 mL, 72 mmol, 3 eq.) and catalytic amounts of DBTDL (200 μ L) in 30 mL THF was prepared in a 250 mL Schlenk flask. BAPO-HEA (11.00 g, 24 mmol, 1 eq.) dissolved in 60 mL THF was added dropwise at room temperature. After stirring for 16 h at 50°C in the dark, the reaction mixture was concentrated to 30 mL and precipitated in 150 mL hexane. The yellow precipitate was filtered off and recrystallized from diethyl ether/hexane (30 mL/ 10 mL, r.t. to -20°C, 20 h). A yellow solid was obtained after removing the solvent under high vacuum for 14 h (14.03 g, 93.2 %).



^1H NMR (300.13 MHz, CD_2Cl_2 , 298 K): δ [ppm] = 1.26-1.41 (m, 4 H, $\text{CH}_2\text{CH}_2\text{CH}_2\text{CH}_2\text{NCO}$), 1.41-1.53 (m, 2 H, $\text{CH}_2\text{CH}_2\text{NH}$), 1.53-1.66 (m, 2 H, $\text{CH}_2\text{CH}_2\text{NCO}$), 2.22 (s, 12 H, *o*- CH_3 Mes), 2.30 (s, 6 H, *p*- CH_3 Mes), 2.47-2.57 (m, 2 H, PCH_2CH_2), 2.60-2.71 (m, 2 H, PCH_2CH_2), 3.11 (q, 2 H, CH_2NH), 3.28 (t, 2 H, $^3J_{\text{HH}} = 6.6$ Hz, CH_2NCO), 4.15-4.22 (m, 2 H, CH_2OCONH), 4.22-4.30 (m, 2 H, $\text{CH}_2\text{OCOCH}_2$), 5.01 (b, 1 H, NH), 6.89 (s, 4 H, H_{ar} Mes).

$^{31}\text{P}\{^1\text{H}\}$ NMR (121.49 MHz, CD_2Cl_2 , 298 K): δ [ppm] = 24.9 ppm.

$^{13}\text{C}\{^1\text{H}\}$ NMR (75.47 MHz, CD_2Cl_2 , 298 K): δ [ppm] = 20.1 (s, *o*- CH_3 Mes), 21.5 (s, *p*- CH_3 Mes), 21.7 (d, $^1J_{\text{PC}} = 55.5$ Hz, CH_2P), 26.5 (d, $^2J_{\text{PC}} = 2.9$ Hz, CH_2CO), 26.7 (s, $\text{CH}_2\text{CH}_2\text{CH}_2\text{NH}$), 26.8 (s, $\text{CH}_2\text{CH}_2\text{CH}_2\text{NCO}$), 30.4 (s, $\text{CH}_2\text{CH}_2\text{NH}$), 31.7 (s, $\text{CH}_2\text{CH}_2\text{NCO}$), 41.4 (s, CH_2NH), 43.5 (s, CH_2NCO), 62.8 (s, CH_2OCONH), 63.8 (s, $\text{CH}_2\text{OCOCH}_2$), 122.5 (s, NCO), 129.8 (s, $\text{C}^{3,5}$ Mes), 136.3 (s, $\text{C}^{2,6}$ Mes), 136.4 (d, $^2J_{\text{PC}} = 41.1$ Hz, C^1 Mes), 142.2 (s, C^4 Mes), 172.0 (d, $^3J_{\text{PC}} = 12.6$ Hz, COCH_2), 216.3 (d, $^1J_{\text{PC}} = 53.5$ Hz, COMes).

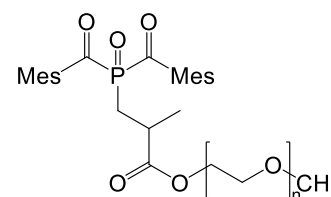
IR (ATR [cm^{-1}]): 2929 (w), 2895 (w), 2259 (s), 1738 (m), 1712 (s), 1680 (s), 1606 (m), 1542 (m), 1254 (m), 1197 (s), 1142 (s).

ESI MS [$\text{M} + \text{NH}_4$] $^+$ $m/z = 644.3095$, meas. 644.3089.

m.p. 61°C.

Polyethylene glycol with terminal BAPO group (12, PEG-BAPO)

A suspension of bis(mesityl)phosphane (3.59 g, 11 mmol, 1.1 eq.) and triethylamine (0.15 mL, 1.1 mmol, 10 mol%) in ethanol (100 mL) was prepared in a 250 mL Schlenk flask. Poly(ethylene glycol) methyl ether methacrylate ($M_n = 950$ g/mol, 9.50 g, 10 mmol, 1 eq.) was added. After stirring for 24 h at 60°C, aqueous hydrogen peroxide (1.9 mL, 22 mmol, 2.2 eq., 35%) was added dropwise at 0 °C. After stirring vigorously at r.t. for 6 h, the solvent was removed under reduced pressure. After recrystallization three times from diethyl ether/pentane (40 mL/10 mL, -20 °C), a yellow solid was obtained after removing the solvent under high vacuum for 14h (9.31 g, 72.1%).



$^1\text{H-NMR}$ (300.13 MHz, CDCl_3 , 298 K): δ [ppm] = 1.27 (d, 3 H, CHCH_3 , $^3J_{\text{HH}} = 7.2$ Hz), 2.21 (s, 6 H, *o*- CH_3 Mes), 2.21 (s, 6 H, *o*- CH'_3 Mes), 2.25 (s, 6 H, *p*- CH_3 Mes), 2.36-2.50, 2.65-2.99 (m, 3 H, PCH_2CHCO), 3.33-3.40 (OCH_3), 3.48-3.87, 4.10-4.22 (CH_2O), 6.81 (s, 4 H, H_{ar} Mes);

$^{13}\text{C}\{^1\text{H}\}$ -NMR (75.47 MHz, CDCl_3 , 298 K): δ [ppm] = 19.4 (d, $^3J_{\text{PC}} = 7.6$ Hz, CHCH_3), 19.9 (s, *o*- CH_3 Mes), 21.3 (s, *p*- CH_3 Mes), 29.0 (d, $^1J_{\text{PC}} = 54.3$ Hz, CH_2P), 33.8 (d, $^2J_{\text{PC}} = 3.5$ Hz, CHCO), 59.1 (s, OCH_3), 64.1, 69.0, 70.6, 72.0 (CH_2O), 129.3 (s, $\text{C}^{3,5}$ Mes), 135.8 (d, $^2J_{\text{PC}} = 41.1$ Hz, C^1 Mes), 135.9 (d, $^2J_{\text{PC}} = 41.0$ Hz, $\text{C}^{1'}$ Mes), 136.0 (d, $^3J_{\text{PC}} = 15.6$ Hz, $\text{C}^{2,6}$ Mes), 141.4 (d, $^5J_{\text{PC}} = 1.9$ Hz, C^4 Mes), 174.8 (d, $^3J_{\text{PC}} = 8.2$ Hz, COCH), 215.5 (d, $^1J_{\text{PC}} = 53.9$ Hz, COMes), 215.8 (d, $^1J_{\text{PC}} = 53.1$ Hz, $\text{C}'\text{OMes}$);

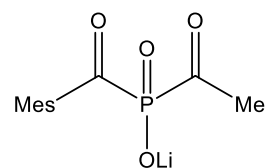
$^{31}\text{P}\{^1\text{H}\}$ -NMR (121.49 MHz, CDCl_3 , 298 K): δ [ppm] = 24.7 ppm;

IR (ATR [cm^{-1}]): 2879 (s), 1730 (w), 1552(w), 1466 (w), 1444 (w), 1344 (s), 1278 (m), 1242 (m), 1146 (s), 1105 (s), 1032 (s), 957 (s), 842 (s), 728 (m).

m.p. 35°C.

Lithium bis(2,4,6-trimethylbenzoyl)phosphinate (**13**, BAPO-OLi)

Bis(2,4,6-trimethylbenzoyl)phosphinic acid (**BAPO-OH**, 716.7 mg, 2 mmol, 1 eq.) was dissolved in the mixture of methanol (5 mL) and water (3 mL) in a 50 mL round-bottom flask. Lithium carbonate (74.6 mg, 1 mmol, 99 %, 1 eq.) was added and the mixture was stirred for 12 h at room temperature. The solvent was removed under vacuum to afford a yellowish solid (721.3 mg, 1.98 mmol, 99 %).



¹H-NMR (300.13 MHz, D₆-DMSO, 298 K): δ [ppm] = 2.23 (s, 18 H, *o*- and *p*-CH₃ Mes), 6.77 (s, 4 H, *H*_{ar} Mes);

¹³C{¹H}-NMR (75.47 MHz, D₆-DMSO, 298 K): δ [ppm] = 19.2 (s, *o*- CH₃ Mes), 20.6 (s, *p*-CH₃ Mes), 127.6 (s, C^{3,5} Mes), 133.8 (s, C^{2,6} Mes), 137.0 (s, C⁴ Mes), 140.5 (d, ²*J*_{PC} = 39.2 Hz, C¹ Mes), 227.1 (d, ¹*J*_{PC} = 105.7 Hz, COMes);

³¹P{¹H}-NMR (121.49 MHz, D₆-DMSO, 298 K): δ [ppm] = 0.8.

¹H-NMR (300.13 MHz, D₂O, 298 K): δ [ppm] = 2.29 (s, 12 H, *o*-CH₃ Mes), 2.29 (s, 6 H, *p*-CH₃ Mes), 7.02 (s, 4 H, *H*_{ar} Mes);

¹³C{¹H}-NMR (75.47 MHz, D₂O, 298 K): δ [ppm] = 18.6 (s, *o*- CH₃ Mes), 20.2 (s, *p*- CH₃ Mes), 128.5 (s, C^{3,5} Mes), 134.6 (s, C^{2,6} Mes), 137.2 (d, ²*J*_{PC} = 39.2 Hz, C¹ Mes), 140.7 (s, C⁴ Mes), 226.7 (d, ¹*J*_{PC} = 104.9 Hz, COMes);

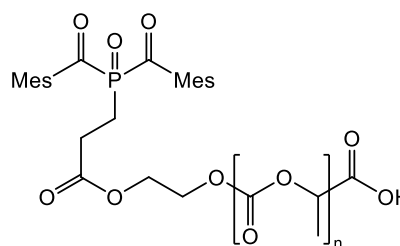
³¹P{¹H}-NMR (121.49 MHz, D₂O, 298 K): δ [ppm] = 0.0.

IR (ATR [cm⁻¹]): 2918 (m), 1648 (m), 1448 (w), 1244 (vs.), 1088 (vs.), 961 (w), 896 (m), 844 (s), 694(w).

ESI MS [M + H]⁺ m/z = 365.1489, meas. 365.1487.

Poly(lactic acid) with terminal BAPO group (14, PLA-BAPO)

BAPO-HEA (91.6 mg, 0.2 mmol) and *D, L*-lactide (2.88 g, 10 mmol) were dissolved in 15 mL of dry DCM in a 50 mL Schlenk flask. DBU (30 μ L, 0.2 mol) was injected and the mixture was stirred for 2 h at room temperature. The polymer was precipitated in cold methanol twice and isolated by centrifugation and dried overnight in a vacuum oven to yield 1.35 g of yellowish solid.



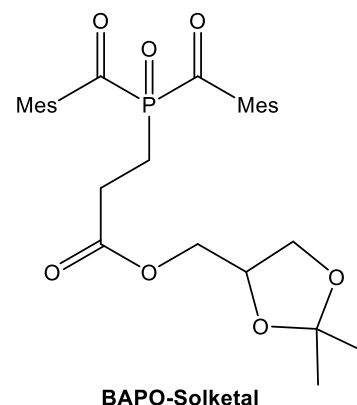
$^1\text{H NMR}$ (300.13 MHz, CDCl_3 , 298 K): δ [ppm] = 1.23-1.80 (b, 3H, CHCH_3), 2.20 (s, 12 H, *o*- CH_3 Mes), 2.25 (s, 6 H, *p*- CH_3 Mes), 2.43-2.71 (m, 4 H, PCH_2CH_2), 3.70 (b, 1 H, OH), 4.18-4.40 (m, 4 H, $\text{OCH}_2\text{CH}_2\text{O}$), 5.03-5.32 (b, 1 H, CHCH_3), 6.82 (s, 4 H, H_{ar} Mes).

GPC (PMMA calibration): $M_n = 17.1$ kg/mol, $M_w = 21.6$ kg/mol, PDI = 1.26.

2,3-Dihydroxypropyl 3-(bis(2,4,6-trimethylbenzoyl)phosphoryl)propanoate (15, BAPO-Diol)

1. Synthesis of (2,2-dimethyl-1,3-dioxolan-4-yl)methyl 3-(bis(2,4,6-trimethylbenzoyl)phosphoryl)propanoate (BAPO-Solketal)

A solution of BAP-H (6.528 g, 20 mmol) and triethylamine (0.28 mL, 2 mmol, 0.1 eq.) in 40 mL DME was prepared in a 100 mL Schlenk flask. (2,2-Dimethyl-1,3-dioxolan-4-yl)methyl acrylate (3.724 g, 20 mmol, 1 eq.) was added. After stirring for 12 h at room temperature, the solvent was removed under reduced pressure. The oily residue was dissolved in toluene (20 mL), H₂O₂ (30%, 4.8 mL, 2.3 eq.) was added dropwise at 0 °C. After stirring vigorously at r.t. for 5 h, the solvent was removed under reduced pressure. A yellow oil was obtained and re-dissolved in DCM (60 mL) and dried over Na₂SO₄. After filtration the solvent was removed under vacuum to obtain a yellow oil (9.981 g, 94.4%).



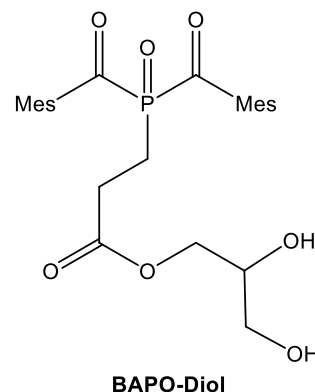
¹H-NMR (300.13 MHz, CDCl₃, 298 K): δ [ppm] = 1.35 (s, 3 H, CH₃), 1.40 (s, 3 H, CH₃), 2.23 (s, 12 H, *o*-CH₃ Mes), 2.26 (s, 6 H, *p*-CH₃ Mes), 2.47-2.59 (m, 2 H, PCH₂), 2.63-2.75 (m, 2 H, COCH₂), 3.66-3.73, 4.00-4.19, 4.22-4.32 (m, 5 H, OCH₂CHCH₂O), 6.84 (s, 4 H, H_{ar} Mes).

¹³C{¹H}-NMR (75.47 MHz, CDCl₃, 298 K): δ [ppm] = 19.8 (s, *o*-CH₃ Mes), 21.3 (s, *p*-CH₃ Mes), 21.4 (d, ¹J_{PC} = 55.5 Hz, CH₂P), 25.4 (s, CH₃), 26.0 (d, ²J_{PC} = 3.2 Hz, CH₂CO), 26.8 (s, CH₃), 65.4 (s, OCH₂CH), 66.3 (s, CH₂OCCH₃), 73.5 (s, CH₂CHCH₂), 109.9 (s, C(CH₃)₂), 129.4 (s, C^{3,5} Mes), 135.8 (d, ²J_{PC} = 41.3 Hz, C¹ Mes), 135.8 (s, C^{2,6} Mes), 141.6 (s, C⁴ Mes), 171.6 (d, ³J_{PC} = 13.7 Hz, COCH₂), 215.4 (d, ¹J_{PC} = 53.9 Hz, COMes).

³¹P{¹H}-NMR (121.49 MHz, CDCl₃, 298 K): δ [ppm] = 24.7 ppm.

2. Hydrolysis of BAPO-Solketal

To a solution of BAPO-Solketal (1.586 g, 3 mmol) in CH₃CN (15 ml), Zn(NO₃)₂·4H₂O (15 mmol, 5 eq.) was added and stirred at 50°C for 4 hours. The solvent was evaporated, and the oily residue was diluted with CH₂Cl₂ (45 ml) and washed with water (30 ml) and dried over Na₂SO₄. After filtration the solvent was removed under vacuum. The residual was recrystallized from a diethyl ether/pentane mixture (30 mL/10 mL, -20 °C), a yellowish solid was obtained (1.242 g, 84.7%).



¹H-NMR (300.13 MHz, CDCl₃, 298 K): δ [ppm] = 2.23 (s, 12 H, *o*-CH₃ Mes), 2.28 (s, 6 H, *p*-CH₃ Mes), 2.52-2.75 (m, 4 H, P CH₂CH₂), 3.40-3.59, 3.71-3.81, 4.10-4.15 (m, 5 H, OCH₂CHCH₂O), 6.86 (s, 4 H, *H*_{ar} Mes).

¹³C{¹H}-NMR (75.47 MHz, CDCl₃, 298 K): δ [ppm] = 19.9 (s, *o*-CH₃ Mes), 21.4 (s, *p*-CH₃ Mes), 21.5 (d, ¹*J*_{PC} = 54.7 Hz, CH₂P), 26.9 (d, ²*J*_{PC} = 4.2 Hz, CH₂CO), 63.1 (s, OCH₂CH), 66.4 (s, CHOH), 69.6 (s, CH₂OH), 129.5 (s, C^{3,5} Mes), 135.6 (dd, ²*J*_{PC} = 41.6 Hz, C¹ Mes), 136.0 (d, ³*J*_{PC} = 7.6 Hz, C^{2,6} Mes), 141.8 (d, *J* = 3.8 Hz, C⁴ Mes), 171.7 (d, ³*J*_{PC} = 7.7 Hz, COCH₂), 214.8 (d, ¹*J*_{PC} = 53.4 Hz, COMes), 214.9 (d, ¹*J*_{PC} = 53.3 Hz, C'OMes).

³¹P{¹H}-NMR (121.49 MHz, CDCl₃, 298 K): δ [ppm] = 24.7 ppm.

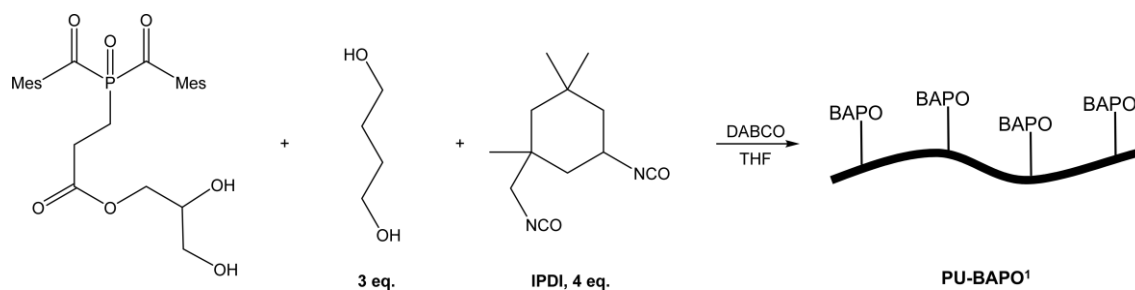
IR (ATR [cm⁻¹]): 3394 (br.), 2952 (s), 2925 (s), 2878 (s), 1736 (s), 1674 (s), 1641 (s), 1607 (s), 1420 (s), 1380 (s), 1184 (m), 1033 (m), 849 (m), 802 (m), 743 (m).

UV/Vis λ [nm] = 290, 359, 390;

ESI MS [M + Na]⁺ *m/z* = 511.1856, meas. 511.1859.

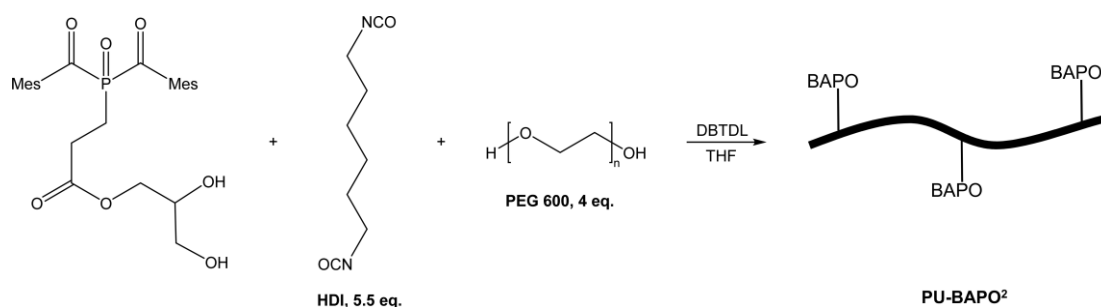
m.p. 57°C.

Polyurethane with side-chain BAPO (**16**, PU-BAPO¹)



In a 20 mL Schlenk flask, a solution of **15** (0.488 g, 1 mmol), 1,4-butanediol (0.270 g, 3 mmol, 3 eq.) and isophorone diisocyanate (0.936 g, 4 mmol, 4 eq.) in 5 mL THF was prepared and degassed by three freeze-pump-thaw cycles. Subsequently, 1,4-diazabicyclo[2.2.2]octane (9 mg, 2 mol%) dissolved in 1 mL THF was injected and the solution was heated to 60 °C for 8 h. The mixture was cooled to room temperature and was poured into a large amount of n-hexane-diethyl ether mixed solvent (300 mL, 1 : 1) to precipitate the polymer. The precipitate was collected by filtration and dried under high vacuum at room temperature. The polymer was obtained as a yellow powder.

Polyurethane with side-chain BAPO (**17**, PU-BAPO²)



In a 50 mL Schlenk flask, a solution of **15** (0.977 g, 2 mmol), polyethylene glycol 600 (4.800 g, 8 mmol, 4 eq.) in 10 mL THF was prepared and degassed by three freeze-pump-thaw cycles. Freshly distilled hexamethylene diisocyanate (1.79 mL, 5.5 eq.) and dibutyltin dilaurate (10 μ L) dissolved in 5 mL THF was prepared in another 50 mL Schlenk flask and was degassed by three freeze-pump-thaw cycles. The mixture of diols was added dropwise to the diisocyanate solution at 0 °C, the mixture was allowed to warm to room temperature and kept stirring for 1 h. Then heated to 60 °C for 14 h. The mixture was cooled to room temperature and was poured into a large amount of n-hexane-diethyl ether mixed solvent (400 mL, 5 : 3) to precipitate the polymer. The precipitate was collected by filtration and dried under high vacuum at room temperature. The polymer was obtained as a yellow powder.

Curriculum Vitae: Jieping Wang

Personal Details

Last Name	Wang
First Name	Jieping
Born	25.06.1987, China
Address	LAC, HCI H122, Vladimir-Prelog-Weg 1-5/10, 8093 Zürich, Switzerland.
Email	jieping.wang@inorg.chem.ethz.ch

Education

10/2012 – 04/2017	Doctorate in Chemistry ETH Zürich
09/2009 – 04/2012	Master of Science Nanjing University of Science and Technology
09/2005 – 06/2009	Bachelor of Engineering Nanjing University of Science and Technology

Teaching Experiences

09/2013 – 01/2016	Undergraduate Student Instructor
03/2015 – 05/2015	Master Student Mentor

Presentations

1. 3rd Scientific Progress Report meetings of NRP 66 (*oral*). **2015**, Thun, Switzerland.
 2. 4th EPONE International Polysaccharide Conference (*oral*). **2015**, Warsaw, Poland.
 3. 13th European Workshop on Phosphorus Chemistry (*poster*). **2016**, Berlin, Germany.
 4. 33rd SAOG Meeting (*poster*). **2017**, Fribourg, Switzerland.
-

Publications

1. **J. Wang**, A. Chiappone, I. Roppolo, F. Shao, E. Fantino, M. Lorusso, D. Rentsch, K. Dietliker, C. F. Pirri, H. Grützmacher. *Angew. Chem. Int. Ed.* **2018**, *57*, 2353-2356.
2. **J. Wang**, S. Stanic, A. A. Altun, M. Schwentenwein, K. Dietliker, L. Jin, J. Stampfl, S. Baudis, R. Liska, H. Grützmacher. *Chem. Commun.* **2018**, *54*, 920-923.
3. M. Sahin, K. K. Krawczyk, P. Roszkowski, **J. Wang**, B. Kaynak, W. Kern, S. Schlögl, H. Grützmacher. *Eur. Polym. J.* **2018**, *98*, 430-438.
4. A. Eibel, D. E. Fast, J. Sattelkow, M. Zalibera, **J. Wang**, A. Huber, G. Müller, D. Neshchadin, K. Dietliker, H. Plank, H. Grützmacher, G. Gescheidt. *Angew. Chem. Int. Ed.* **2017**, *56*, 14306-14309. (Hot Paper)
 - Highlighted in *SYNFACTS* (**2017**, *13*, 1141)
5. M. Sahin, S. Schlögl, S. Kaiser, W. Kern, **J. Wang**, H. Grützmacher. *J. Polym. Sci. A Polym. Chem.* **2017**, *55*, 894-902.
6. M. Sangermano, M. Periolatto, M. Castellino, **J. Wang**, K. Dietliker, J. L. Grützmacher, H. Grützmacher. *ACS Appl. Mater. Interfaces* **2016**, *8*, 19764-19771.
7. **J. Wang**, G. Siqueira, G. Müller, D. Rentsch, A. Huch, P. Tingaut, J. L. Grützmacher, H. Grützmacher. *Chem. Commun.* **2016**, *52*, 2823-2826.
8. S. Benedikt, **J. Wang**, M. Markovic, N. Moszner, K. Dietliker, A. Ovsianikov, H. Grützmacher, R. Liska. *J. Polym. Sci. A Polym. Chem.* **2016**, *54*, 473-479.
9. **J. Wang**, W. Yi, C. Cai. *Z. Anorg. Allg. Chem.* **2012**, *638*, 53-55.

Awards & Honors

09/2012	PhD Scholarship, China Scholarship Council (CSC)
10/2011	Outstanding Graduates Awards, NUST
12/2009	Fuda Group Technology Innovation Award (Second Prize)
09/2009	First Class Scholarship of Master Students, NUST
04/2009	First Class Scholarship, NUST
